Spring 2021

Integrated solar and ESS ac/dc systems for various grid applications

Phani Ratna Vanamali Marthi

Department: Electrical and Computer Engineering

Recommended Citation

Marthi, Phani Ratna Vanamali, "Integrated solar and ESS ac/dc systems for various grid applications" (2021). *Doctoral Dissertations*. 2976.
https://scholarsmine.mst.edu/doctoral_dissertations/2976

INTEGRATED SOLAR AND ESS AC/DC SYSTEMS FOR VARIOUS GRID APPLICATIONS

by

PHANI RATNA VANAMALI MARTHI

A DISSERTATION

Presented to the Graduate Faculty of the

MISSOURI UNIVERSITY OF SCIENCE AND TECHNOLOGY

In Partial Fulfillment of the Requirements for the Degree

DOCTOR OF PHILOSOPHY

in

ELECTRICAL ENGINEERING

2021

Approved by

Dr. Mariesa L. Crow, Advisor
Dr. Suman Debnath
Dr. Jonathan Kimball
Dr. Mehdi Ferdowsi
Dr. Pourya Shamsi
Dr. Bruce McMillin

PUBLICATION DISSERTATION OPTION

This dissertation consists of the following four articles, formatted in the style used by the Missouri University of Science and Technology:

Paper I: Pages 16-38, Synchronverter-based Control of Multi-Port Autonomous Reconfigurable Solar Plants (MARS), was published in *Proceedings of the 2020 IEEE Energy Conversion Congress and Exposition Conference*, Detroit, Michigan, October 2020.

Paper II: Pages 39-53, Model Based Predictive Control for Frequency Support in Multi-port Autonomous Reconfigurable Solar Plants, has been accepted for the *2021 IEEE Innovative Smart Grid Technologies 2021 Conference*, February 2021.

Paper III: Pages 54-78, A Predictive Grid Forming Control for Multi-port Autonomous Reconfigurable Solar Plants, has been submitted to *IEEE Transactions on Sustainable Energy*.

Paper IV: Pages 79-106, Suite of Solutions for Reducing Momentary Cessation in PV/Hybrid PV Plants in Low SCR and Low Inertia Grids, will be submitted to *IEEE Transactions on Power Delivery*.

ABSTRACT

Modular multilevel converters (MMC) have gained prominence for high power applications in recent years due to their technical merits such as voltage scalability, harmonic performance, and high efficiency. Integration of renewable energy sources such as solar photovoltaic (PV) systems and energy storage systems (ESS) to the grid using power electronic (PE) resources is increasing due to the techno-economic successes achieved by such systems. Following these developments, the integration of MMCs with PV plants and ESS systems is one of the dynamic research avenues being pursued. Along these lines, an integrated development of PV plants, ESS, and alternating- and direct-current (ac/dc) power plants through Multi-port Autonomous Reconfigurable Solar (MARS) systems is proposed.

The main research focus is on the modeling, control, and benefits of MARS systems compared to the discrete development of state-of-the-art PV, ESS, and HVdc links. Ultra-fast high fidelity MARS HVdc models are developed to test advanced control algorithms. The advanced control algorithms include synchronverter-based (SG-based) control and *grid forming* predictive control methods. The *grid forming* control methods are defined as the control methods that regulate converter output voltage without any phase-locked loop (PLL) mechanisms. The proposed *grid forming* predictive control is based on the model based predictive control (MBPC-based) for frequency support and also includes traditional voltage support control. The proposed control algorithms in the MARS control architecture are evaluated for various short circuit ratio (SCR) and inertia conditions. To illustrate the technical benefits of MARS systems, the MARS system architecture is compared with the discrete development of state-of-the-art PV plants and hybrid PV plants. In addition, the MARS system is proposed as a promising solution to the momentary cessation problem often seen in PE-based resources connected to low SCR and low inertia grids.

ACKNOWLEDGMENTS

I dedicate this dissertation to my advisor, Dr. Mariesa L. Crow, my parents, Prasad Marthi and Varalakshmi Sita, my cousin, Dr. Sri Rajasekhar Kothapalli, and Dr. Suman Debnath for their immense support, tremendous belief, inspiration, and guidance. This epic journey would not have been possible without them.

I would like to thank Dr. Jonathan W. Kimball, Dr. Mehdi Ferdowsi, Dr. Pourya Shamsi, and Dr. Bruce McMillin for being my committee members and for their valuable inputs and suggestions. I am grateful to my friends, Bhanu, Paulomi, Maigha, Subhajyothi, Krishnan, Bhargav, Nallan, Jashwant, Darshit, Gautham, Jatin, Samarth, Rasoul, and Fahd, at Missouri University of Science and Technology for their friendship and great association. I am also thankful to Jingfan Sun, Shilpa Marti, Qianxue Xia, Yashwant Kumar, Rachit Agarwal, and Dr. Burak Ozpineci at Oak Ridge National Laboratory (ORNL) for their fellowship. A particular thanks to Dr. Madhu Sudhan Chinthavali for his mentoring and providing me an opportunity to work at ORNL.

My family members were of great support to me always, providing me motivation and strength to go the extra mile. A special thanks to my uncles, Shyam Sundar Velamuri and C.S. Sastry, for their encouragement. Also special thanks to my cousins, Sri Ravi Shankar, Vijaya Durga, and Aarsha, for supporting me through all the times.

I cannot imagine how my last years of graduation might have been without my wife, Madhuri. Her care, affection, and love were the key driving force in achieving this long cherished dream. My heartfelt thanks to my elder brother, Ram Marthi, for being my guardian angel at all times. Finally, there was one important person who stood by me through all the twists, ups, downs, and all other vicissitudes of my graduate life whom I can never thank enough. He is my younger brother, Dr. Poorna Marthi.

TABLE OF CONTENTS

Page

SECTION

PAPER

SECTION

LIST OF ILLUSTRATIONS

Figure Page

SECTION

PAPER I

PAPER II

PAPER III

PAPER IV

LIST OF TABLES

Table Page

SECTION

PAPER I

PAPER II

PAPER III

PAPER IV

SECTION

1. INTRODUCTION

1.1. MOTIVATION & PROBLEM STATEMENT

As the penetration of power electronic (PE) based power plants increases, the inertia of the electric grid system is reduced resulting new stability challenges [1]. *Grid-forming* inverters connecting photovoltaic systems (PV) to the grid and energy storage systems (ESSs) are likely to play an important role in addressing these stability concerns. Moreover, high-voltage direct current (HVdc) links employing such systems will also be a enabler to transfer power from remotely located PV power plants and to improve grid stability. With the increased penetration of PV, the discrete development of PV and ESS connecting to transmission ac grid and HVdc links is one of the solutions for stable operation of the grid. Therefore, an integrated concept for the integration of PV and ESS to the transmission ac grid and HVdc links called Multi-Port Autonomous Reconfigurable Solar (MARS) system is proposed. This dissertation focuses on the modeling, control, and application of the MARS system. Advanced *grid forming* control methods for MARS using traditional and predictive control methods are proposed and are compared with *grid following* control methods. The *grid forming* controllers are the controllers that regulate the PE-based converter's instantaneous terminal voltages without any phase-locked loop (PLL) and can co-exist with other *grid-forming*, *grid-following*, and synchronous resources in the same alternate current (ac) grid [2]. The *grid following* controllers are the controllers that estimate the instantaneous angle of the PE-based converter's terminal voltage with the help of PLL and use a current control loop to regulate the ac current injected into the ac grid [2]. Additionally, the MARS system is proposed as a potential solution to reduce the momentary cessation problem seen in PE based systems. The proposed solution is compared with traditional and modified approaches.

1.2. DISSERTATION OUTLINE

The dissertation is organized as follows: in the introduction section, methods employed to develop the ultra-fast high fidelity MARS HVdc models are described. The ultra-fast CPU simulation algorithm used to simulate the MARS system is comprised of a hybrid discretization algorithm with a relaxation technique that reduces the imposed computational burden and employs a multi-rate method. These high fidelity and high efficiency simulation approaches are of paramount importance because the simulation of the MARS systems using traditional existing software may be computationally burdensome. The ultra-fast high fidelity models will potentially result in faster development and testing of control methods and their implementation. The developed models are used in all of the papers contained in this dissertation. In Paper I, a synchronverter based (SG-based) frequency control and a voltage control for the MARS system are proposed. The proposed control methods are tested for high penetration of renewable energy scenarios and compared with *grid following* control methods. In Paper II, a model based predictive control (MBPC) for frequency response in the MARS system is proposed. The proposed control method is tested for various short circuit ratio (SCR) conditions. In Paper III, a *grid forming* predictive control for frequency support in the MARS system is proposed along with a voltage support control for high penetration of renewable energy scenarios and remote integration scenarios. The proposed method is validated on real-time OPAL-RT simulators. In addition to the offline and online evaluation of the control methods, theoretical proofs for the improved performance of the proposed control methods are provided. Finally in Paper IV, the MARS system is presented as a solution for the momentary cessation problem. Momentary cessation is when the PE-based resources cease to operate and inject zero current to the ac grid [1]. This phenomenon has been a challenging problem in the high penetration of PE-based systems. In addition, the MARS solution is compared with other typical solutions for momentary cessation using discrete development of PV and ESS systems along with upgrades. The upgrades include synchronous condensers, capacitor banks, and dampers.

1.3. CONTRIBUTIONS

The main contributions of this dissertation are:

- To develop ultra-fast high fidelity MARS system HVdc models based on state space models and simulation algorithms that accurately represent the MARS system.
- To develop and implement comprehensive SG-based control method that includes, governor control, inertial control, frequency control, reactive power control, voltage control, and overcurrent protection for the MARS system.
- To develop and evaluate a *grid forming* predictive control method for the MARS system.
- To propose solutions for the momentary cessation problem that include the MARS system, the discrete development of PV plants with upgrades, and discrete hybrid PV plants with upgrades.

1.4. MARS MATHEMATICAL MODELS

Due to their attractive features, modular multilevel converters (MMCs) and their variants such as alternate arm converters (AACs) [3] and cascaded two-level converters (CTLs) [4] have achieved commercial success in the recent years [5, 6]. The technical and economic merits of solar integrated systems (PV) and energy storage systems (ESS) have increased the installation pace of renewable sources across the United States. These two achievements have led to growing interest in research on the integration of PV and ESS

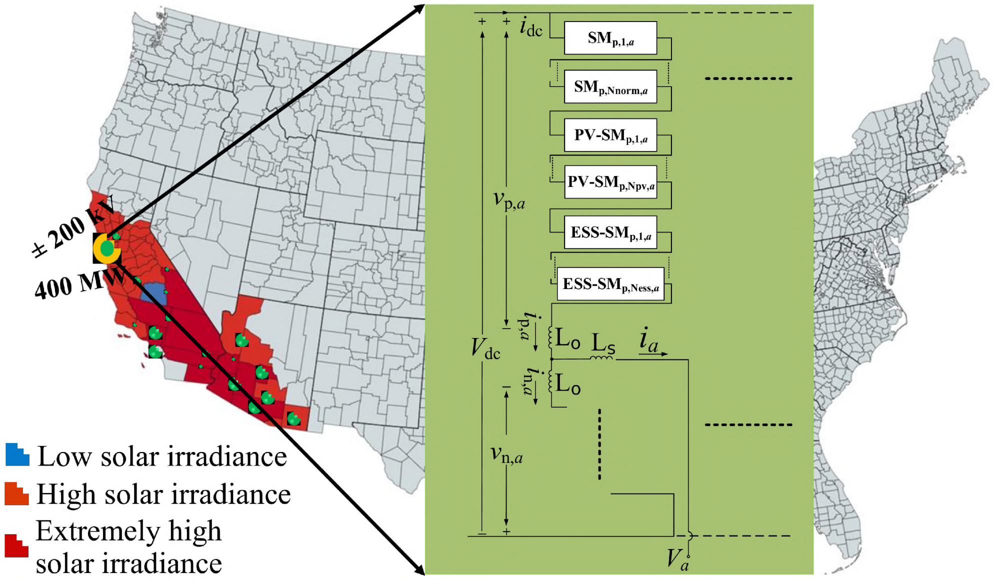

Figure 1.1. Circuit configuration of MARS

systems to MMCs. To address these challenges, the integration of PV and ESS systems through a new topology called the Multi-Port Autonomous Reconfigurable Solar (MARS) plant is proposed. The MARS system circuit configuration is novel and unique when compared to the circuit configurations of PV and ESS integrated MMC systems proposed in previous research endeavors [7, 8, 9, 10]. The research works in [7, 8, 9, 10] explore either PV systems or battery-based energy storage systems (BESS)or both, and neglect to consider more than 15 submodules (SMs) per arm. In the MARS system, normal SMs, PV SMs and ESS SMs are co-located in an arm of a phase leg with more than 200 SMs. The total number of SMs in a three phase MARS system can exceed 1200 and the number of states can be greater than 7000. Due to the presence of thousands of states and hundreds of SMs, the simulation of the MARS system is computationally complex and time consuming. Also, MARS systems are numerically stiff, which adds to the computational complexity and long simulation times. These issues necessitate a novel simulation algorithm to simulate the MARS system. Therefore it is important to model and simulate the MARS system with an algorithm capable of reducing the imposed computational burden.

$$\left(L_o + L_s\right) \frac{\mathrm{d}i_{\mathrm{p},j}}{\mathrm{d}t} - L_s \frac{\mathrm{d}i_{\mathrm{n},j}}{\mathrm{d}t} = -\left(R_o + R_s\right) i_{\mathrm{p},j} + R_s i_{\mathrm{n},j} + \frac{V_{\mathrm{dc}}}{2} - v_j - v_{\mathrm{cm}} - v_{\mathrm{p},j}, \forall j \in (a, b, c), \tag{1.1a}$$

$$\left(L_o + L_s\right) \frac{\mathrm{d}i_{\mathrm{n},j}}{\mathrm{d}t} - L_s \frac{\mathrm{d}i_{\mathrm{p},j}}{\mathrm{d}t} = -\left(R_o + R_s\right) i_{\mathrm{n},j} + R_s i_{\mathrm{p},j} + \frac{V_{\mathrm{dc}}}{2} + v_j + v_{\mathrm{cm}} - v_{\mathrm{n},j}, \forall j \in (a, b, c), \tag{1.1b}$$

$$v_{\mathrm{y},j} = \sum_{\mathrm{l}=1}^{\mathrm{N_{norm}}} v_{\mathrm{smnorm,y,l},j} + \sum_{\mathrm{l}=\mathrm{N_{norm}}+1}^{\mathrm{N_{pv}}} v_{\mathrm{smpv,y,l},j} + \sum_{\mathrm{l}=\mathrm{N_{pv}}+1}^{\mathrm{N_{ess}}} v_{\mathrm{smess,y,l},j} \tag{1.1c}$$

$$\sum_{\mathrm{l}=\mathrm{l_x}}^{\mathrm{N_x}} v_{\mathrm{smx,y,l},j} = \sum_{\mathrm{l}=\mathrm{l_x}}^{\mathrm{N_x}} \left[S_{\mathrm{yl1},j} v_{\mathrm{cy,l},j} + \left\{\left(1 - S_{\mathrm{yl1},j}\right)\left(1 - S_{\mathrm{yl2},j}\right) v_{\mathrm{cy,l},j}\right\} \operatorname{sgn}\left(i_{\mathrm{y},j}\right)\right],$$

$$\forall \mathrm{y} \in (\mathrm{p}, \mathrm{n}), \forall j \in (a, b, c) \tag{1.1d}$$

(1.1e)

where

$v_{\mathrm{smx,y,l},j} = v_{\mathrm{smnorm,y,l},j}$ or $v_{\mathrm{smpv,y,l},j}$or $v_{\mathrm{smess,y,l},j}$; $\mathrm{l_x} = 1$ or $(\mathrm{N_{norm}} + 1)$ or $(\mathrm{N_{pv}} + 1)$;

$\mathrm{N_x} = \mathrm{N_{norm}}$ or $(\mathrm{N_{pv}})$ or $(\mathrm{N_{ess}})$

1.5. HIGH FIDELITY MARS-HVDC MODEL

Based on solar resources and load centers, an example of a MARS system integration is shown in Figure 1.1. In Figure 1.1, the upper arm of phase a is highlighted and shown. The MARS circuit topology has three phases. Each phase $j \in (a, b, c)$ has two phase-legs, each phase-leg has two arms, and each arm $\mathrm{y} \in (\mathrm{p}, \mathrm{n})$ has a total of N SMs. The SMs can be a normal half-bridge system, a half-bridge with a dc-dc converter connecting to PV system, or a half-bridge with a dc-dc converter connecting to energy storage. The SMs in each arm are divided into N_{norm} normal SMs, N_{pv} PV-SMs, and N_{ess} ESS-SMs. The arm inductor is sized based on the fault current limits and the SM capacitor is determined based on capacitor voltage ripple requirements. The PV and ESS SM inductors are sized based on the dc-dc converter inductor current ripple requirements.

The total number of states within a MARS system are $(18N_{norm}+36N_{pv}+42N_{ess})+6$. These states include the arm currents, normal SM capacitor voltages, PV-SM capacitor voltages, PV-SM inductor currents, ESS-SM capacitor voltages, ESS-SM inductor currents, and semiconductor switching states ($S_{\mathrm{ylx},j}$). The arm current dynamics are given in (1.1a) - (1.1d). A comprehensive description of other terms in (1.1) and normal SMs' operation is detailed in [11] and [12].

1.6. PV SM

The PV system is integrated into an SM using a boost converter. The inductor current (i_{Lpv}) dynamics in the boost converter are given by

$$L_{\mathrm{pv}}\frac{\mathrm{d}i_{\mathrm{Lpv,y,l},j}}{\mathrm{d}t} = v_{\mathrm{cpv,y,l},j} - \left(1 - S_{\mathrm{yl3},j}\right) v_{\mathrm{c,y,l},j}\mathrm{sgn}\left(i_{\mathrm{Lpv,y,l},j}\right) \tag{1.2}$$

The dynamics of SM capacitor voltages ($v_{\mathrm{c,y,l},j}$) in the PV-SM are given by

$$C_{\mathrm{SM}}\frac{\mathrm{d}v_{\mathrm{c,y,l},j}}{\mathrm{d}t} = -\frac{v_{\mathrm{c,y,l},j}}{R_p} - i_{\mathrm{y,l},j} + \left(1 - S_{\mathrm{yl3},j}\right)\left(i_{\mathrm{Lpv,y,l},j}\mathrm{sgn}\left(i_{\mathrm{Lpv,y,l},j}\right)\right) \tag{1.3}$$

where

$$i_{\mathrm{y,l},j} = -S_{\mathrm{yl1},j}i_{\mathrm{y},j} - \left(1 - S_{\mathrm{yl1},j}\right)\left(1 - S_{\mathrm{yl2},j}\right)\mathrm{sgn}\left(i_{\mathrm{y},j}\right)$$

The PV input capacitor dynamics ($v_{\mathrm{cpv,y,l},j}$) are given by

$$C_{\mathrm{pv}}\frac{\mathrm{d}v_{\mathrm{cpv,y,l},j}}{\mathrm{d}t} = i_{\mathrm{pv,y,l},j} - i_{\mathrm{Lpv,y,l},j} \tag{1.4}$$

1.7. ESS-SM

The ESS system is integrated into the SM using a bidirectional dc-dc converter. The inductor current (i_{Less}) dynamics in the bi-directional converter are given by

$$L_{\mathrm{ess}}\frac{\mathrm{d}i_{\mathrm{Less,y,l},j}}{\mathrm{d}t} = v_{\mathrm{cess,y,l},j} - S_{\mathrm{yl4},j}\left(1 - S_{\mathrm{yl3},j}\right)v_{\mathrm{c,y,l},j} \times \left(1 - S_{\mathrm{yi3},j}\right)\left(1 - S_{\mathrm{yi4},j}\right)v_{\mathrm{cyi},j}\,\mathrm{sgn}\left(i_{\mathrm{Less,y,l},j}\right) \tag{1.5}$$

The dynamics of the SM capacitor voltages in the ESS-SM are given by

$$C_{\mathrm{SM}}\frac{\mathrm{d}v_{\mathrm{c,y,l},j}}{\mathrm{d}t} = -\frac{v_{\mathrm{c,y,l},j}}{R_p} - i_{\mathrm{y,l},j} + S_{\mathrm{yl4},j}\left(1 - S_{\mathrm{yl3},j}\right)i_{\mathrm{Less,y,l},j} + \left(1 - S_{\mathrm{yl4},j}\right)\left(1 - S_{\mathrm{yl3},j}\right) \times \left(i_{\mathrm{Less,y,l},j}\,\mathrm{sgn}\left(i_{\mathrm{Less,y,l},j}\right)\right) \tag{1.6}$$

The ESS input capacitor dynamics ($v_{\mathrm{cess,y,l},j}$) are given by

$$C_{\mathrm{ess}}\frac{\mathrm{d}v_{\mathrm{cess,y,l},j}}{\mathrm{d}t} = i_{\mathrm{ess,y,l},j} - i_{\mathrm{Less,y,l},j} \tag{1.7}$$

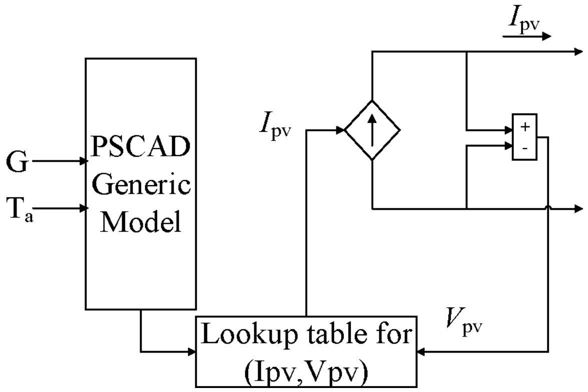

Figure 1.2. Implementation of five-point model

1.8. PV AND ESS MODELS

A single diode PV model [13] is computationally very expensive to implement in real-time simulation studies, because of the presence of an exponential term in the diode current of the current-voltage equation. To reduce the computational burden, a five-point PV model based on simulation and empirical data is developed and validated with a generic PV model in PSCAD. The premise of this model is to generate a look-up table that outputs the current generated from the PV (i_{pv}) based on the variation of the voltage measured at the PV terminals (v_{pv}). The five-point model contains five points in the i_{pv}-v_{pv} curve obtained from the PV panel datasheet. The five points are (0, I_{sc}), (V_{mp}, I_{mp}), ($V_{\mathrm{oc}}/2$, i_3), (($V_{\mathrm{oc}}+V_{\mathrm{mp}})/2$, i_4), and (0, V_{oc}). The terms i_3 and i_4 are obtained from the i_{pv}-v_{pv} curves. The remainder of the currents are obtained from extrapolating these known points. Based on these extrapolated curves, i_{pv} is generated which feeds into the dc-dc converter. The implementation is summarized in Figure 1.2.

The ESS model consists of a voltage source E_b and an internal series resistance R_{batt}. In this model, the battery's state of charge (SOC) is considered.

1.9. SIMULATION ALGORITHM FOR THE HIGH-FIDELITY MARS SYSTEM MODEL

The MARS system can be represented as a non-linear non-autonomous switched system and is derived as a system of semi-explicit differential algebraic equations (DAEs). The derived high-fidelity model of the MARS system is partitioned based on the numerical stiffness associated with the states and then the separated states are discretized using the hybrid discretization method.

Numerical stiffness is observed in arm currents and inductor currents dynamics of both the PV and ESS SMs under a blocked condition scenario. This is due to the presence of the sgn function in (1.1d). In the capacitor voltages' dynamics, numerical stiffness is not observed, because the sgn function present in them is treated as an external input.

The SM capacitor voltages' dynamics and PV and ESS input capacitor dynamics, are discretized using forward-Euler, which is a non-stiff explicit discretization algorithm. Implicit discretization algorithms with stiff-decay and A-stable properties such as backward-Euler are used to discretize the arm current dynamics and inductor current dynamics. In comparison to a conventional simulation of the MARS system, hybrid discretization-based simulation reduces the matrix size to (5×5) from $(6(N_{norm} + N_{pv} + N_{ess}) + 5) \times (6(N_{norm} + N_{pv} + N_{ess}) + 5)$. In addition to the system matrix size reduction, a matrix size reduction in the dc-dc converter is also observed. If hybrid discretization is applied as in [11] alone, the PV- and ESS- dc-dc converters will require $6(N_{pv}+N_{ess})$ inversions of (2×2) matrices in comparison to the simple arithmetic computations of $6(N_{\text{pv}} + N_{ess})$ equations. This results in a large reduction of computational costs as inverting a (5×5) matrix and calculating simple arithmetic equations is computationally inexpensive.

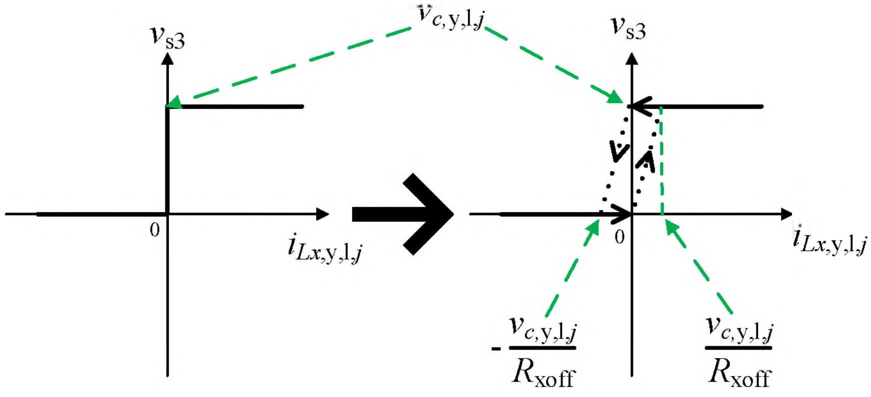

Figure 1.3. Hysteresis relaxation technique for PV- and ESS-SM

To reduce the stiffness in the PV and ESS SMs, a hysteresis relaxation technique is introduced that approximates the voltage across the switches in the dc-dc converters of the PV and ESS SMs. The proposed hysteresis relaxation technique is shown in Figure 1.3. In the case of PV and ESS SM, the modified voltage across the dc-dc converter switch under the blocked operating condition is implemented as follows:

$$\tilde{v}_{\mathrm{s3}}[k] = v_{\mathrm{s3nx,y,1},j}[k] + i_{\mathrm{Lx,y,1},j}[k] R_{\mathrm{x,y,1},j}[k], \tag{1.8}$$

where $v_{\mathrm{s3nx,y,1},j}[k]$, $i_{\mathrm{Lx,y,1},j}[k]$, and $R_{\mathrm{x,y,1},j}[k]$ are defined in (1.9) and k is the time instant. The detailed implementation of the MARS-HVdc simulation algorithm is summarized in Figure 1.4.

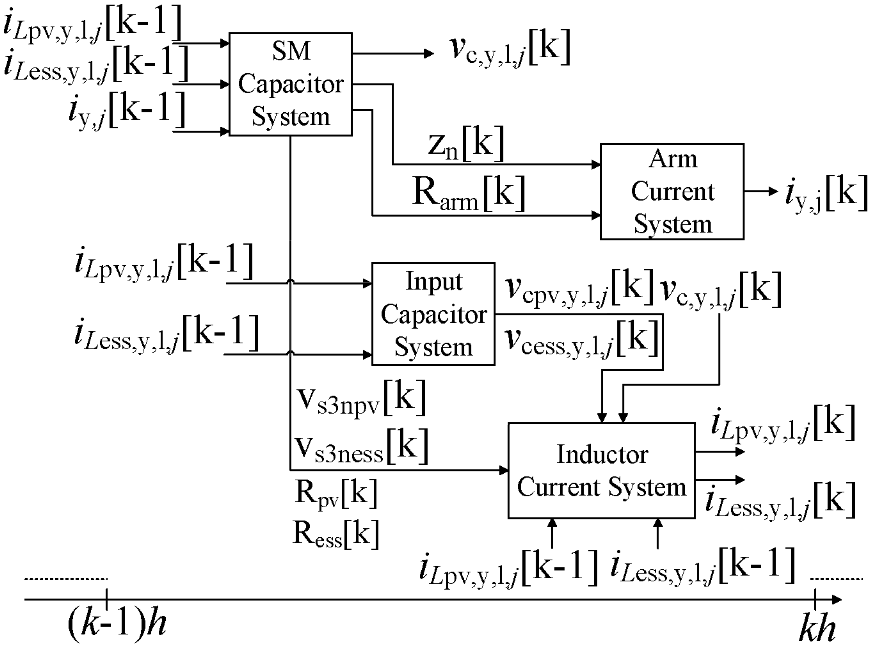

Figure 1.4. Detailed implementation of the MARS-HVdc simulation

$$v_{\mathrm{s3nx,y,l},j}[k] = \begin{cases} 0, & \text{if} \left(i_{\mathrm{Lx,y,l},j}[k-2] < 0 \quad \text{and} \quad i_{\mathrm{Lx,y,l},j}[k-1] < -\dfrac{v_{\mathrm{c,y,l},j}[k]}{R_{\mathrm{xoff}}} \right), \\ 0, & \text{if} \left(i_{\mathrm{Lx,y,l},j}[k-2] < 0 \quad \text{and} \quad i_{\mathrm{Lx,y,l},j}[k-1] > 0 \right) \quad \text{or} \\ & \left(0 < i_{\mathrm{Lx,y,l},j}[k-1] < \dfrac{v_{\mathrm{c,y,l},j}[k]}{R_{\mathrm{xoff}}} \right), \\ v_{\mathrm{c,y,l},j}[k], & \text{otherwise.} \end{cases} \tag{1.9a}$$

$$R_{\mathrm{x,y,l},j}[k] = \begin{cases} 0, & \text{if} \left(i_{\mathrm{Lx,y,l},j}[k-2] < 0 \quad \text{and} \quad i_{\mathrm{Lx,y,l},j}[k-1] < -\dfrac{v_{\mathrm{c,y,l},j}[k]}{R_{\mathrm{xoff}}} \right), \\ 0, & \text{if} \left(i_{\mathrm{Lx,y,l},j}[k-2] > 0 \quad \text{and} \quad i_{\mathrm{Lx,y,l},j}[k-1] > \dfrac{v_{\mathrm{c,y,l},j}[k]}{R_{\mathrm{xoff}}} \right), \\ R_{\mathrm{xoff}}, & \text{otherwise.} \end{cases} \tag{1.9b}$$

where $i_{\mathrm{Lx,y,l},j} = i_{\mathrm{Lpv,y,l},j}$ or $i_{\mathrm{Less,y,l},j}$; $R_{\mathrm{xoff}} = R_{\mathrm{pvoff}}$ or R_{essoff};

$v_{\mathrm{s3nx,y,l},j} = v_{\mathrm{s3npv,y,l},j}$ or $v_{\mathrm{s3ness,y,l},j}$

1.10. REDUCED-ORDER MODEL

The reduced-order model of the MARS system consists of the equivalent model of the hardware circuit as shown in Figure 1.5 and the upper-level controller. In the equivalent model of the MARS system hardware, the voltage in each arm is averaged to remove the switching dynamics in (1.1d). The voltage in each arm is modeled using an externally controlled voltage source, with the external input signal dependent on the upper-level controller. In this model, the capacitor voltages of all of the SMs in the arms are assumed to be balanced and the same. The reduced-order model of the MARS system is controlled to generate dispatched active and reactive powers into the grid. The upper-level controller takes power commands as inputs to control the ac-side currents in the MARS system, where the power commands are the function of dispatch commands. Based on the available PV and ESS power ratings, and the MARS system active and reactive power ratings, maximum and minimum power limits are imposed on the upper-level controller.

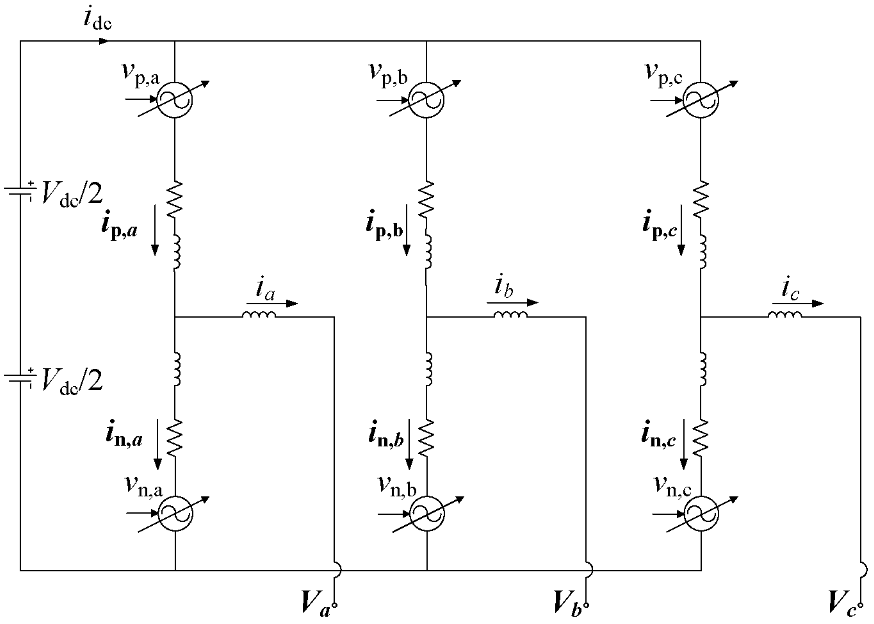

Figure 1.5. Schematic of reduced-order model

1.11. SIMULATION RESULTS & VALIDATION

The proposed algorithm is tested on a benchmark test system based on the Trans Bay Cable project in Pittsburg, California [14]. Assuming 150 kW, 1 kV PV and ESS submodules (SMs), the number of each type of SM required in the Pittsburg MARS are tabulated in Table 1.1. The size of the PV and ESS SMs are determined based on utilizing 200 A, 3.3 kV SiC devices. The total number of SMs per arm are determined by the dc-link voltage in that location and based on the installed HVdc substation (in the Trans Bay Cable project). The following case studies are considered to compare the results obtained from the proposed simulation algorithm with the reference results: (i) base-case with no PV and ESS generation; (ii) with only PV generation (PV); (iii) with only ESS discharging (ESS); (iv) with PV generation and ESS sending power into the ac grid (discharging) (PV + ESS); (v) with PV system and ESS system receiving (charging) (PV + ESSr); and (vi) with ESS charging (ESSr). The corresponding results are shown in Figure 1.6 - Figure 1.11 for the MARS Pittsburg system. The total simulation time required is 0.033 secs and the time taken for the developed algorithm to complete the required simulation is less than 10 seconds. Whereas, the time taken for the HVdc reference models developed in PSCAD for the required simulation is on the order of days. The improvement in observed speed-up in simulation time is about 8000 times. The developed model simulation results are promising in comparison to reference PSCAD models with an accuracy of 99%.

Table 1.1. Pittsburg MARS system parameters

Parameter	**Value**
System rating	400 MW
dc bus voltage (V_{dc})	±200 kV
ac side voltage (V_{ac})	220 kV
PV system power rating (P_{PV})	100 MW
ESS system power rating (P_{ESS})	32.8 MW
Number of normal SMs per arm (N_{norm})	102
Number of PV SMs per arm (N_{pv})	111
Number of ESS SMs per arm (N_{ess})	37
Total number of SMs per arm (N)	250
Arm inductance (L_{o})	30.0 mH
Arm resistance (R_{o})	0.1 Ω
Grid side inductance (L_{s})	40.0 mH
Grid side resistance (R_{s})	0.83333 Ω
SM capacitor voltage (V_{SM})	1.6 kV
SM capacitance	7.7 mF

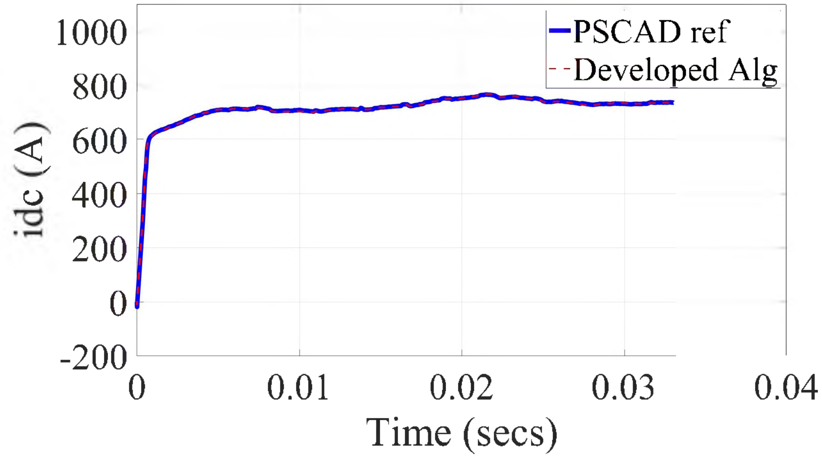

Figure 1.6. dc grid side currents for the base-case with no PV and ESS generation

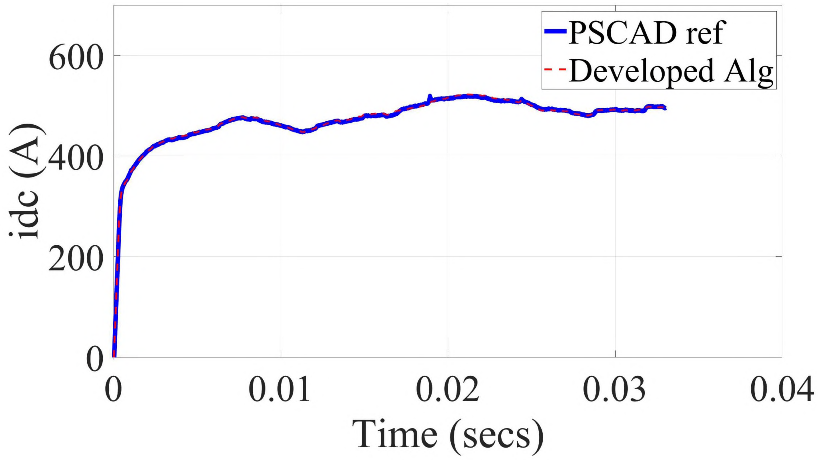

Figure 1.7. dc grid side currents with PV

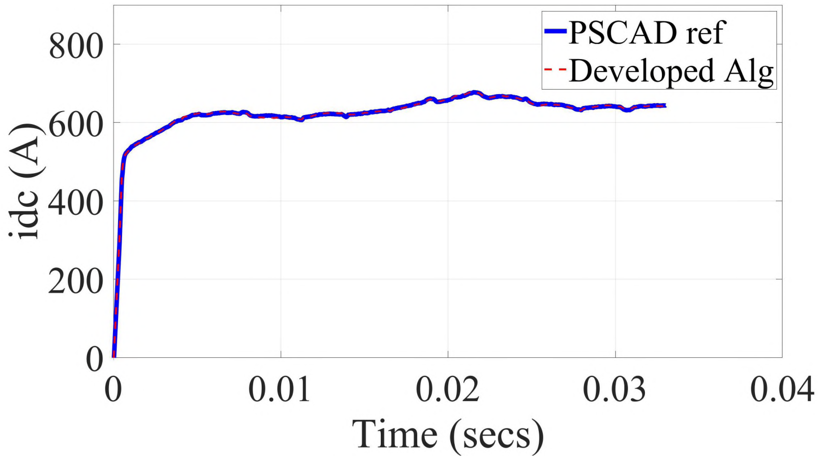

Figure 1.8. dc grid side currents with ESS

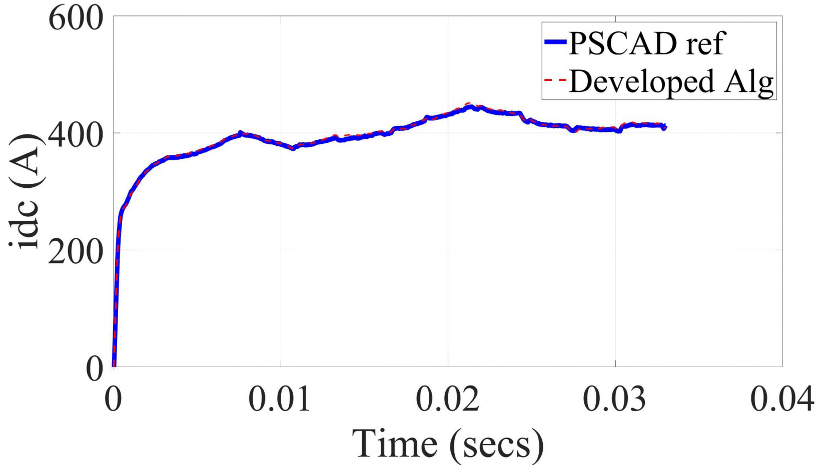

Figure 1.9. dc grid side currents with PV + ESS

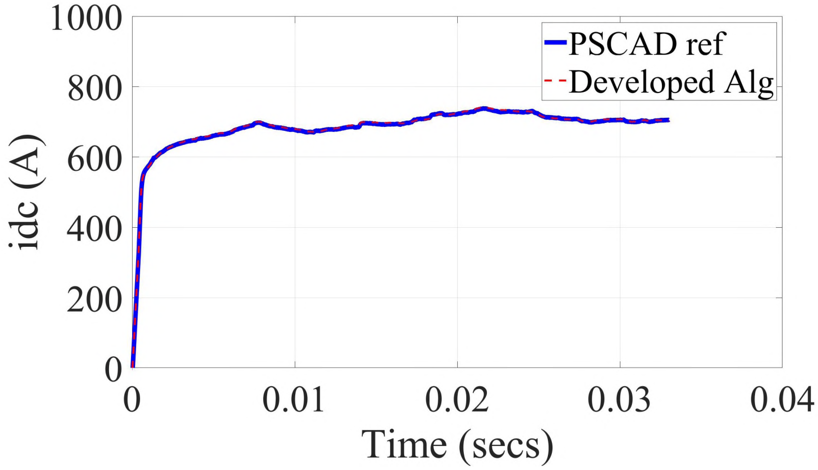

Figure 1.10. dc grid side currents with PV + ESSr

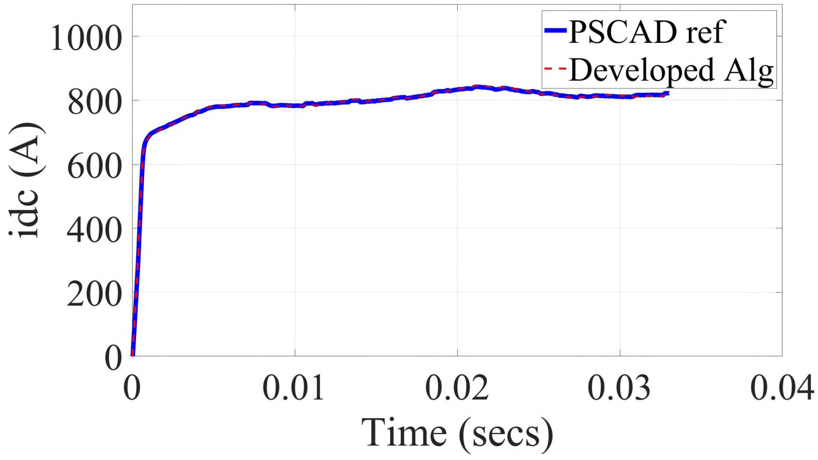

Figure 1.11. dc grid side currents with ESSr

PAPER

I. SYNCHRONVERTER-BASED CONTROL OF MULTI-PORT AUTONOMOUS RECONFIGURABLE SOLAR PLANTS (MARS)

ABSTRACT

The control of integrated photovoltaic (PV) plants with energy storage systems (ESSs) has become an important research and development topic in recent times. In this context, a Multi-port Autonomous Reconfigurable Solar (MARS) plant that integrates PV and ESS to the alternating current (ac) transmission grid and high-voltage direct current (HVdc) links is studied in this paper. With a high penetration of power electronic-based resources in the grid, the grid's capability to recover from frequency or voltage disturbances is reduced. Therefore, one of the vital objectives of any new grid integrated power electronic resource is to provide advanced control functions such as voltage and frequency support to the grid during disturbances. In this research work, a detailed implementation of a synchronverter-based control algorithm for the MARS system is presented. The proposed control algorithm and the MARS system control architecture are evaluated through simulations on a PSCAD/EMTDC simulation platform to showcase the performance in different operating conditions. In addition, they are evaluated in Opal-RT offline simulation models which can also be used to perform control-hardware-in-the-loop (cHIL) tests.

Keywords: Synchronverter, HVdc, PV, ESS, VSG

1. INTRODUCTION

There is increased interest in the planning of mixed high-voltage ac-dc transmission systems (or hybrid transmission systems) [1], due to the advantages provided by modular multilevel converters (MMCs) [2]. The integrated development of photovoltaic (PV) systems and battery-based energy storage systems (ESSs) is being explored at a greater pace than ever before due to the associated techno-economic benefits. Following these developments, research on the integration of PV and ESS to high-voltage dc (HVdc) systems has gained prominence in recent times. In this area, the integrated development of PV and ESS connecting to the transmission alternating current (ac) grid and HVdc systems through a multi-port autonomous reconfigurable solar plant (MARS) is presented in this paper. One of the concerns with increased penetration of power electronics systems in the grid is the reduction in the grid's capability to recover from voltage or frequency disturbances. Advanced control functions in power electronics systems and the use of hybrid ac-dc systems can enhance the stability of the grid. On this front, this paper presents a synchronverter-based (SG-based) control algorithm in the MARS system that can improve the grid's capability to respond to voltage or frequency disturbances. The control algorithm can provide frequency support during events in the grid that cause frequency disturbances. In addition to the frequency support, the proposed control algorithm provides voltage support in the events of balanced faults, and ensures no service outages occur. Typically, service outages may be observed in traditional PV or ESS plants due to reduced/increased voltages or varying frequency during these events. The hierarchical control architecture of the MARS system is presented in this paper that can support the synchronverter-based control algorithm.

Simulation studies to evaluate the performance of the proposed MARS control architecture and synchronverter algorithm [3], [4], [5], [6] under various test cases and extreme operating conditions are performed on PSCAD simulation software. The proposed algorithm is compared with the Virtual Synchronous Generator (VSG) [7], [8] control

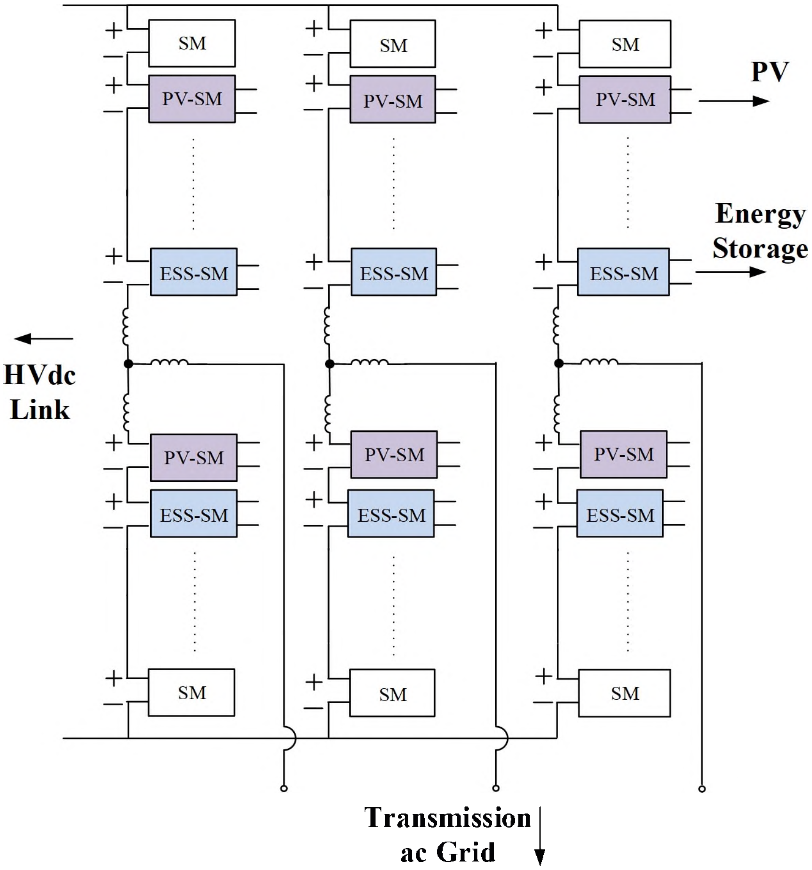

Figure 1. Overview of the MARS system architecture

method and the merits of the proposed control scheme in comparison to the VSG-based control method are presented. The comparison is specifically shown for connection of the MARS system to weak and low-inertia grids, which are expected to grow with increased penetration of power electronics-based resources in the grid. The control algorithms are evaluated in Opal-RT offline simulations, and the models developed can be used to perform control hardware-in-the-loop (cHIL) simulations in future.

A brief discussion of the MARS circuit configuration and high-fidelity electromagnetic transient (EMT) simulation models of the MARS system are given in Section 2. The overall MARS system control architecture is included in Section 3. A detailed description of the proposed SG-based control is presented in Section 4. A VSG-based control method is described in Section 5. Simulation results are included in Section 6. Directions of future research work are presented in Section 7.

2. MARS SYSTEM MODELS

The overview of the architecture of the MARS system is shown in Figure 1. In total, it has six arms, with each arm subdivided into N_{norm} normal submodules (SMs), N_{pv} PV-SMs, and N_{ess} ESS-SMs. The normal SMs are based on half-bridges, which are also the front-end of PV and ESS SMs. The PV systems in the PV-SMs are connected to the front-end through a uni-directional dc-dc converter. The ESS systems in the ESS-SMs are connected to the front-end through a bidirectional dc-dc converter. The mathematical modeling is based on a similar method to the mathematical modeling of MMCs described in [9].

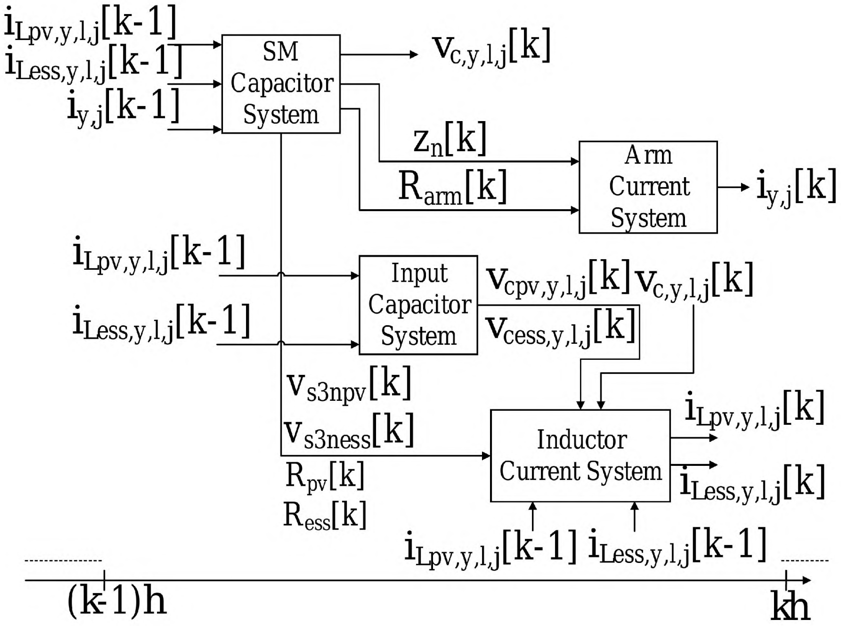

Figure 2. MARS simulation algorithm

The simulation of MARS systems on traditional simulation platforms is highly time-consuming and computationally expensive. Therefore it is imperative to use advanced models and fast simulation algorithms to test the control architectures of MARS systems. Detailed models of the MARS system and simulation algorithms to speed-up simulation are developed based on the method applied to MMCs in [9]. The developed MARS system model is represented by differential algebraic equations (DAEs) and is segregated based on the numerical stiffness present in the states of the DAEs. The segregated systems are then discretized based on their associated stiffness properties to reduce the imposed computational complexity. The comprehensive summary of the simulation algorithm to simulate the MARS system is illustrated in Figure 2.

3. HIERARCHICAL CONTROL ARCHITECTURE OF MARS

The MARS control system, shown in Figure 3, consists of a: (i) L-1 controller, (ii) L-2 controller, and a (iii) L-3 controller. Functionalities of the L-1 controller include voltage and frequency support to the grid, active and reactive power control, dc-link voltage control, ac-/dc-side current control, and energy balance between different types of SMs (PV, ESS, and normal). The voltage and frequency support in L-1 controller is based on a SG-based control algorithm that determines the rotor angle (θ_{sg}), angular frequency (ω_{sg}), and

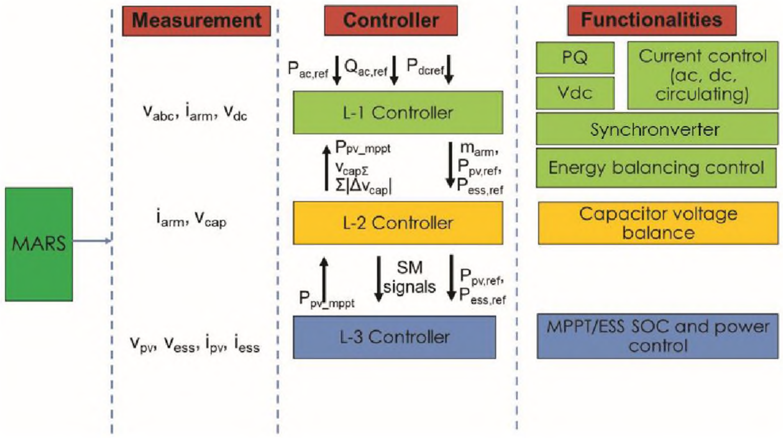

Figure 3. MARS control architecture

the MARS system three-phase output voltage e_{abc}. The L-1 controller also determines the reference power commands of the PV and ESS in the MARS system ($P_{\mathrm{pv,ref}}$ and $P_{\mathrm{ess,ref}}$). The reference power commands of the PV and ESS depend upon the power dispatch commands ($P_{\mathrm{ac,ref}}$, $P_{\mathrm{dc,ref}}$, and $Q_{\mathrm{ac,ref}}$), the power requirements from the SG-based control, the maximum available PV power ($P_{\mathrm{pv,mppt}}$), and the rating of the ESS SMs ($P_{\mathrm{ess,rating}}$). The reference active and reactive powers at the ac-side of the MARS system are the sum of the corresponding dispatch commands and the corresponding power requirements from the SG-based control. Based on the determined θ_{sg}, ω_{sg}, and e_{abc}, the qd current control of the ac-side currents are calculated to generate modulation indices m_{abc}.

The energy balancing control generates the reference circulating current within the phase legs that is controlled by the circulating current control to generate $m_{\mathrm{circ},abc}$. The circulating current control includes the 1st, 2nd, and 4th harmonics controlled using a qd transformation based on [10]. While the 1st harmonic is controlled based on the energy balancing control generated reference, the 2nd and 4th harmonics are controlled to zero. The modulation indices $m_{\mathrm{circ},abc}$ and m_{abc} are combined to generate the arm modulation indices $m_{abc}^{p,n}$ based on [10]. The L-1 controller sends the modulation indices of each arm, reference PV power, and reference ESS power to the L-2 controller. The L-2 controller maintains the capacitor voltages and also generates the switching signals for the front-end half-bridges of all the SMs based on [10]. The L-3 controller controls the power from the PV and ESS SMs, controls the dc-dc converter currents, and sends the switching commands to the dc-dc converters.

4. SYNCHRONVERTER-BASED CONTROL ALGORITHM

The SG-based control algorithm implemented in the control system of the MARS system is shown in Figure 4. It is comprised of a governor loop, inertial loop, reactive power loop, active power loop, and current control loop. The governor model is a time constant T_{D} with a gain D_{p1}. The time constant T_{D} of the governor delay is used to emulate the delayed

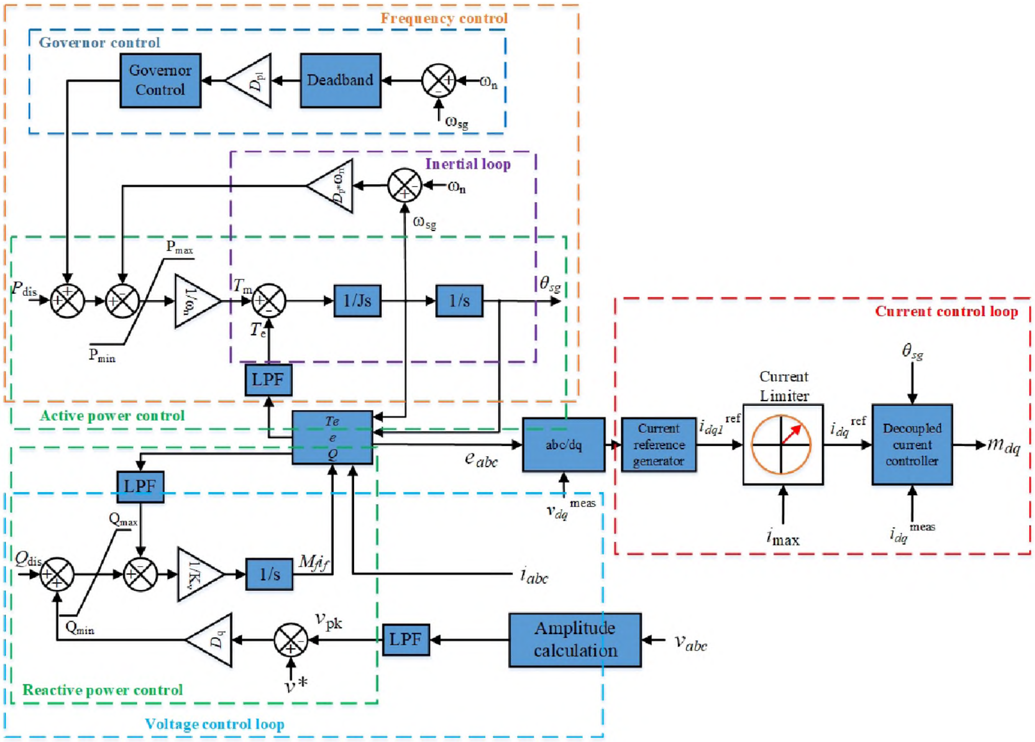

Figure 4. Synchronverter-based control algorithm

mechanical response of the synchronous generator's physical governor. The term $\mathrm{D_{p1}}$ is the frequency - power droop coefficient. The upper limit of the active power (P_{max}) is the maximum available power at that instant that can be used (i.e. summation of the $P_{\mathrm{dc,ref}}$, $P_{\mathrm{pv,mppt}}$, and $P_{\mathrm{ess,rating}}$). The lower limit of the active power (P_{min}) is the minimum available power at the instant that can be used (i.e. summation of the $P_{\mathrm{dc,ref}}$, and -$P_{\mathrm{ess,rating}}$ (used for charging)). The governor's control mechanism shown in Figure 4 can be expressed in the Laplace domain as

$$P_{\mathrm{gov}}(s) = \frac{\mathrm{D_{p1}}}{(1 + \mathrm{T_D}s)}(\omega_n(s) - \omega_{sg}(s)) \tag{1}$$

where ω_{n} is the reference angular frequency reference and ω_{sg} is the calculated angular frequency from the SG-based control. While the representation of the governor control is in the Laplace domain, the implementation was carried out in the time domain by discretizing (1) using the forward-Euler method.

The inertial loop, active power loop, and reactive power loop are based on the synchronverter concept detailed in [3]. The electromagnetic torque T_{e}, the MARS system three-phase output voltage e_{abc}, and the reactive power Q are given by the following:

$$T_{\mathrm{e}} = M_{\mathrm{f}} i_{\mathrm{f}} < \mathbf{i}, \widetilde{(\cos(\theta))} >, \tag{2}$$

$$e_{\mathrm{abc}} = \dot{\theta} M_{\mathrm{f}} i_{\mathrm{f}} \widetilde{(\cos(\theta))}, \tag{3}$$

$$Q = \dot{\theta} M_{\mathrm{f}} i_{\mathrm{f}} < \mathbf{i}, \widetilde{(\sin(\theta))} >, \tag{4}$$

where the vectors $\mathbf{i}$, $\widetilde{\cos(\theta)}$, and $\widetilde{\sin(\theta)}$ are defined in [3].

The current reference generator calculates the qd frame reference currents based on circuit equations that utilize the difference between e_{abc} and ac-side voltage $\mathbf{v}_{\mathrm{s}}$. The discretized circuit equations that are used to calculalte the abc frame of reference currents are given in (5) and are discretized using the backward-Euler method. From the calculated abc frame of reference currents, the qd frame of reference currents are calculated based on the Park's transformation given in [11]:

$$\begin{aligned}
i_{\mathrm{a}}[k] &= \frac{i_{\mathrm{a}}[k-1] + \frac{h}{L_{\mathrm{s}}+L_{\mathrm{o}}/2} \times (e_{\mathrm{a}}[k] - v_{\mathrm{a}}[k])}{(1 + \mathrm{h} \times \frac{R_{\mathrm{s}}+R_{\mathrm{o}}/2}{L_{\mathrm{s}}+L_{\mathrm{o}}/2})} \\
i_{\mathrm{b}}[k] &= \frac{i_{\mathrm{b}}[k-1] + \frac{h}{L_{\mathrm{s}}+L_{\mathrm{o}/2}} \times (e_{\mathrm{b}}[k] - v_{\mathrm{b}}[k])}{(1 + \mathrm{h} \times \frac{R_{\mathrm{s}}+R_{\mathrm{o}}/2}{L_{\mathrm{s}}+L_{\mathrm{o}}/2})} \\
i_{\mathrm{c}}[k] &= \frac{i_{\mathrm{c}}[k-1] + \frac{h}{L_{\mathrm{s}}+L_{\mathrm{o}/2}} \times (e_{\mathrm{c}}[k] - v_{\mathrm{c}}[k])}{(1 + \mathrm{h} \times \frac{R_{\mathrm{s}}+R_{\mathrm{o}}/2}{L_{\mathrm{s}}+L_{\mathrm{o}}/2})}
\end{aligned} \tag{5}$$

where $\mathrm{L_o}$ and $\mathrm{R_o}$ are the arm inductance and the arm resistance; $\mathrm{L_s}$ and $\mathrm{R_s}$ are the grid inductance and the grid resistance respectively; and h is the simulation time step.

As the SG-based control is primarily implemented as a voltage source implementation, it does not have overcurrent limit protection. Therefore, a current limiter is provided to limit the overcurrents in the system. The decoupled current controller consists of qd control of ac-side currents which generate the required modulation indices. The theta (θ_{sg}) calculated from the SG-based control is used in the circulating current control and the qd current control.

5. VIRTUAL SYNCHRONOUS GENERATOR BASED CONTROL

The proposed SG-based method is compared with the VSG-based control [7]. This section briefly describes the implemented VSG-based control. The L-1 controller uses a VSG-based control method to determine the active and reactive power commands based on the measured ac-side voltages of the MARS system (v_{abc}). The ac-side voltages of the MARS system are processed by a phase-locked loop (PLL) to determine the peak value and frequency of the voltages (v_{pk} and f). The peak value and frequency are, respectively, utilized to determine the additional components to be added to the dispatched active and reactive power commands. The controller is summarized in Figure 5.

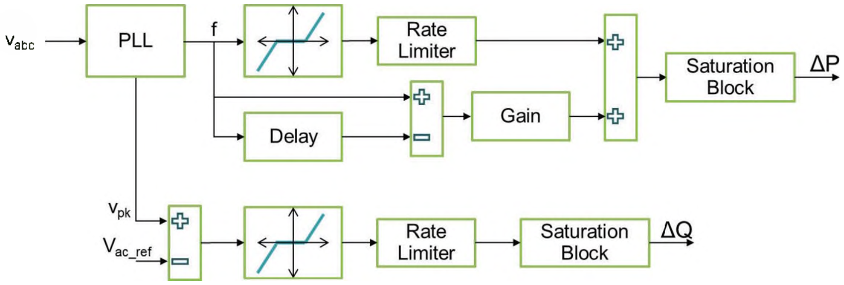

Figure 5. VSG-based control

6. SIMULATION RESULTS & VALIDATION

6.1. TESTING SYSTEMS

The proposed algorithm is tested on a MARS system that has been proposed for Pittsburg, California. This test system is based on upgrades to the TransBay Cable project in Pittsburg, California [12]. Assuming 150 kW, 1 kV PV, and ESS SMs, the number of SMs per arm are 111 PV, 37 ESS, and 81 Normal SMs. The size of the PV and ESS SMs are determined based on utilizing 200 A, 3.3 kV SiC devices in the dc-dc converters. The total number of SMs per arm are determined by the dc-link voltage at the installation location and based on the installed HVdc substation (in the TransBay Cable project).

6.2. USE CASES FOR THE MARS SYSTEM WITH ac GRID MODELS

Multi-level multi-rate MARS system Pittsburg models are developed and tested with the Western Interconnection (WECC)-based ac grid models for different operating condtions. The ac grid in the WECC is modeled based on WSEIG1 to accurately represent the frequency data available [13]. The developed comprehensive MARS Pittsburg system models are tested for different low short circuit ratio (SCR) ac grid conditions and low inertia conditions. The MARS system based on traditional control methods is particularly vulnerable to weak grid conditions for the following reasons [14]:

1. The MARS system does not have inertia because of no rotating masses being present.
2. The electronic controls depend on the stable voltage reference from the grid to provide active and reactive power.
3. As the system becomes weaker, the control specifications can affect the system behavior.

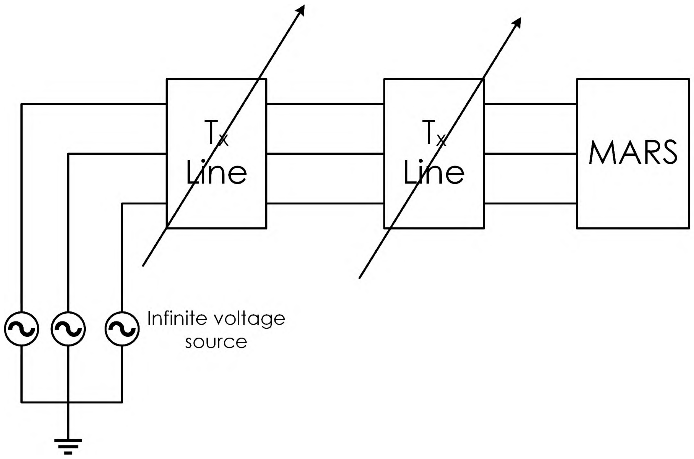

Figure 6. Simulation model setup for low SCR Tests

To overcome these issues, a proposed advanced control is designed to ensure successful operation of the MARS system in these weaker systems. To test the performance of the proposed controller, the MARS system is tested during different SCR and low inertia conditions. There are numerous methods to measure the system strength. One of the ways to determine the system strength of a power system is the SCR, as the measurement of the system strength is related to the equivalent impedance seen from the MARS system terminals to the power system. Therefore to emulate high renewable penetration grids with low SCR, the transmission line lengths between the MARS system and the ac grid system are varied. The procedure is simulated in PSCAD and the simulation setup is shown in Figure 6. The transmission line lengths for different SCRs is tabulated in Table 1.

Table 1. SCR ratios for different line lengths

SCR	Resistance (Ω)	Inductance (H)	Line Length (km)
0.5	14.369	0.6715	861.5
2	3.5535	0.1661	198
4	1.7547	0.0820	87.65
10	0.6333	0.0296	18.85

Two use cases are identified and tested for the operating condition of $P_{\mathrm{ac}} = P_{\mathrm{dc}} = 100$ MW for SCR cases 0.5, 2, 4, and 10. They are: (a) 804.44 MW loss of generation at t = 14.0 secs based on Haynes3 generator in WECC grid, and (b) a balanced three phase fault at t = 4 secs with a duration of 0.2 secs. The inertia of the system (H) in all of these use cases is 23 secs. A special case of low SCR and low inertia is documented in Section 6.2.3.

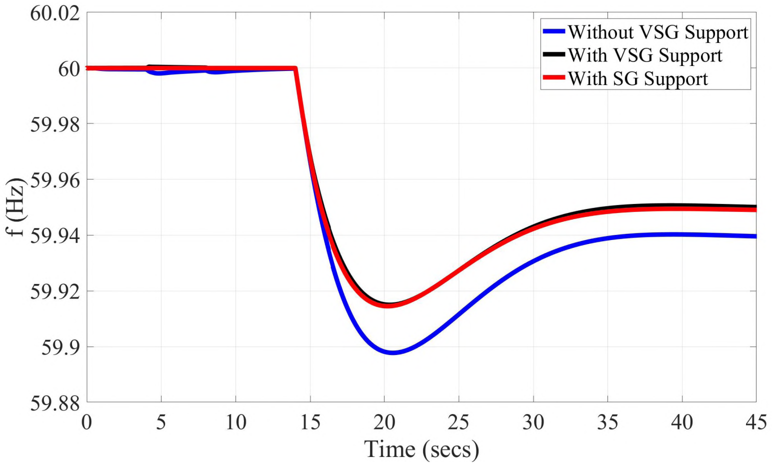

Figure 7. Grid Frequency response for LOG in WECC for SCR = 10

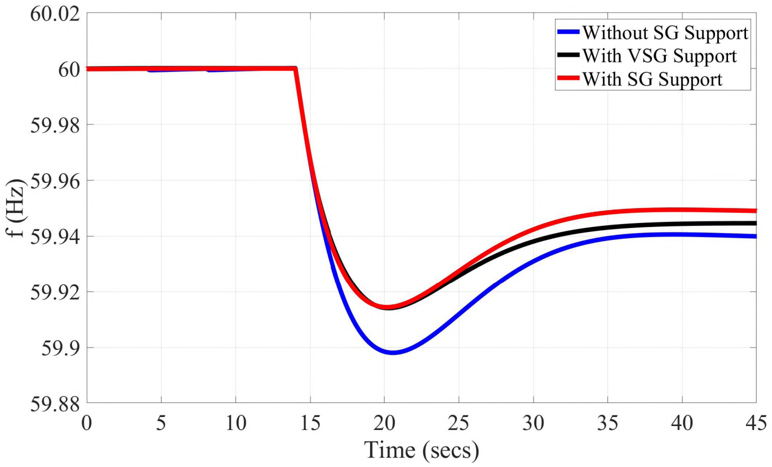

Figure 8. Grid Frequency response for LOG in WECC for SCR = 4

6.2.1. Use Case 1: 804.44 Loss of Generation. An event of 804.44 MW loss of generation (LOG) in the WECC is simulated at t = 14 s. The frequency response measured at Pittsburg for different SCR cases without support, with SG support, and with VSG support from the MARS system are shown in Figure 7 - Figure 10.

In the strong grids with a higher SCR, the frequency support provided by the MARS system through the VSG control method is greater than the frequency support provided by the MARS system through the SG control method as illustrated in Figure 7. As the strength of

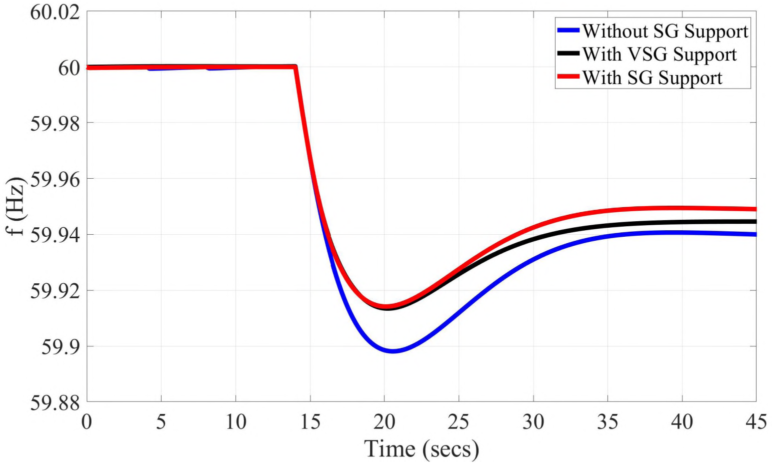

Figure 9. Grid Frequency response for LOG in WECC for SCR = 2

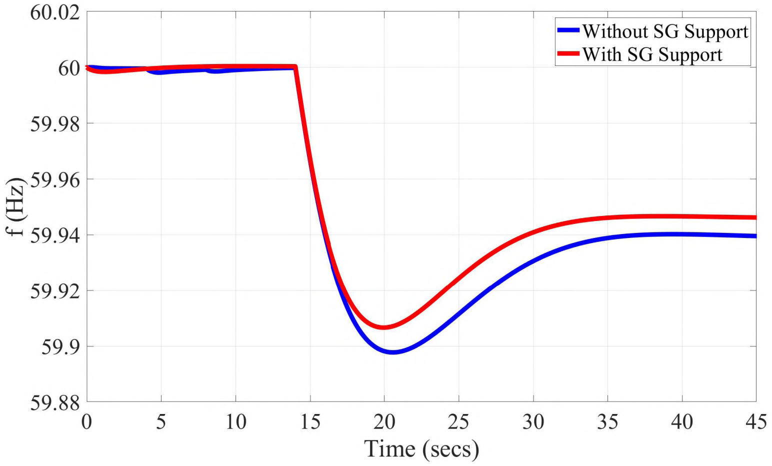

Figure 10. Grid Frequency response for LOG in WECC for SCR = 0.5

Table 2. Improvement in frequency response for different SCRs

SCR	Improvements			
	SG		VSG	
	nadir	steady state	nadir	steady state
0.5	8.69 %	11.00 %	UNSTABLE	
2	15.75 %	15.07 %	15.05 %	7.67 %
4	16.04 %	15.18 %	15.72 %	7.81 %
10	16.37 %	15.66 %	16.87 %	17.34 %

the system decreases in terms of SCR, the frequency support provided by the MARS system through the SG-based control method is greater in comparison to the frequency support provided by the MARS system through the VSG-based control method. This phenomenon can be observed in Figure 8 - Figure 10. This is because the VSG-based control method is implemented with much slower controllers. The VSG-based control method includes a frequency derivative term and its measurement through the PLL is highly challenging in weak grids. The operation of the VSG-based control with faster controllers may induce oscillations which can lead to unstable operation because of this derivative frequency term. Therefore, the VSG control should be operated with slower controllers. This problem is not evident in SG based control, as this method is devoid of both PLL and derivative terms. The frequency improvements in nadir and steady state for each SCR condition and for each type of controller are tabulated in Table 2.

6.2.2. Use Case 2: 3-Phase Fault. A 3-phase fault is simulated on the transmission line between the grid and the MARS system at t = 4.0 s with a fault duration of 0.2 s. After 0.2 s, the fault is self-cleared. Improvement in the voltage profiles of phase-*a* with the help of VSG support and SG support during the fault in different SCR conditions is shown in Figure 11 - Figure 13 and are tabulated in Table 3.

Table 3. Improvement in voltage response for different SCRs

SCR	Improvements	
	SG	VSG
0.5	STABLE	UNSTABLE
2	21.25 %	17.21 %
4	14.16 %	10.98 %
10	6.81 %	5.33 %

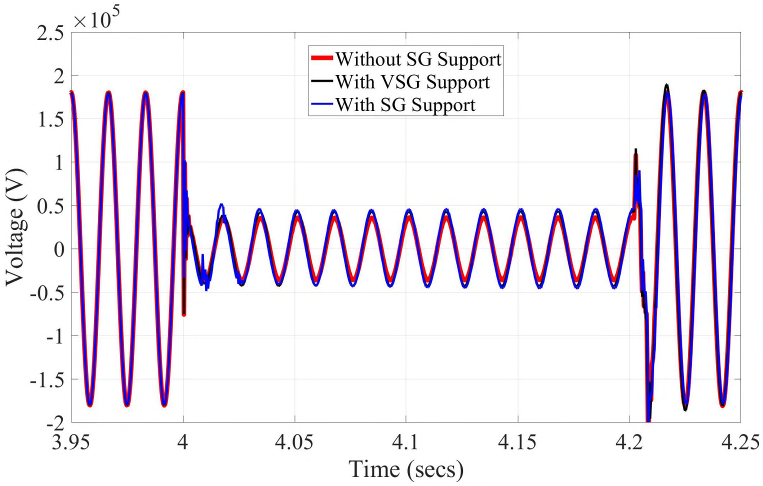

Figure 11. Phase-a grid voltage profile for a 3-phase fault for SCR = 10

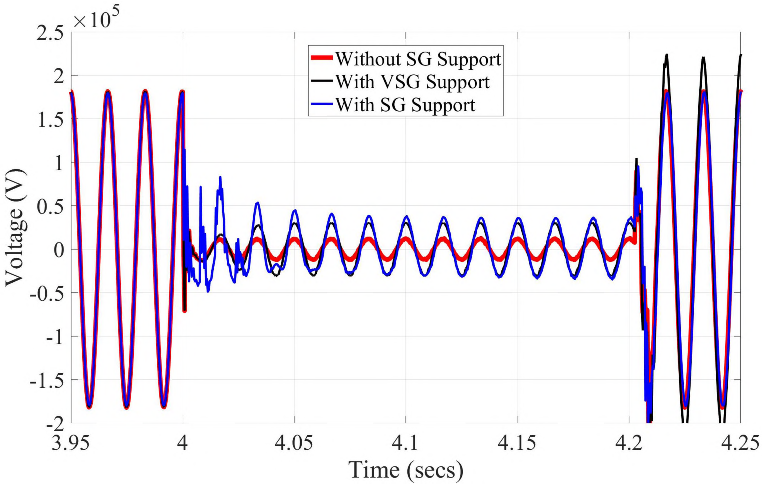

Figure 12. Phase-a grid voltage profile for a 3-phase fault for SCR = 4

For the different SCR cases, the voltage support provided by the MARS system through the SG-based control method is higher in comparison to the voltage support provided by the MARS system through the VSG-based control method. However, in the case of SCR

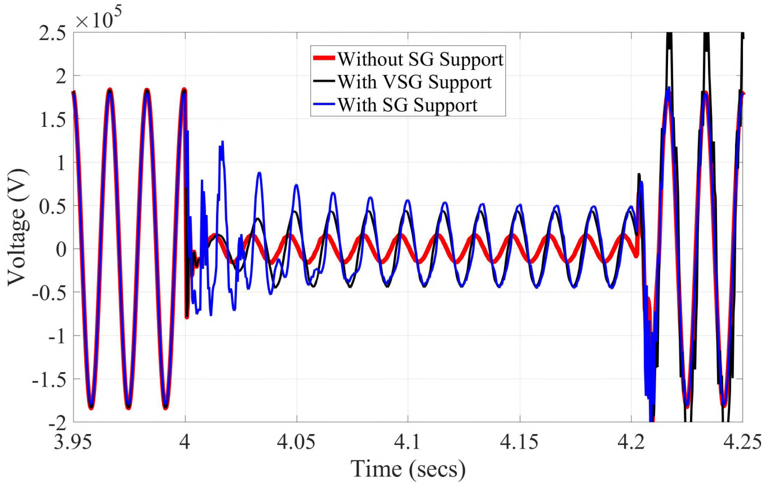

Figure 13. Phase-a grid voltage profile for a 3-phase fault for SCR = 2

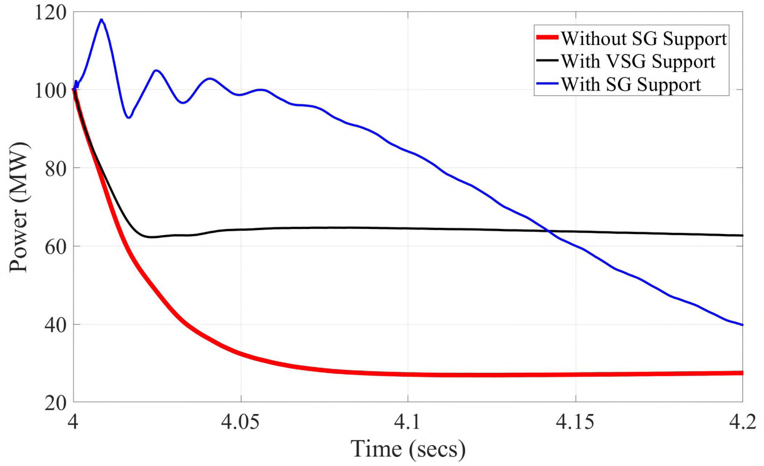

Figure 14. Active power support during a 3-phase fault for SCR = 10

= 10, the active power provided by the SG-based control method is less than the VSG-based control method as shown in Figure 14. Slower controllers are used in the VSG-based control implementation because the PLL measurement is highly sensitive to changes in the grid. This results in inaccurate estimation of the ac-side peak voltage amplitude. Therefore, the proportional control gain used in the reactive power controller is reduced to ensure that the additional reactive power is not affected by the oscillations introduced in the inaccurate peak voltage. The active power and reactive power provided by the MARS system during the fault without support, with VSG support, and SG support are shown in Figure 14 - Figure 19.

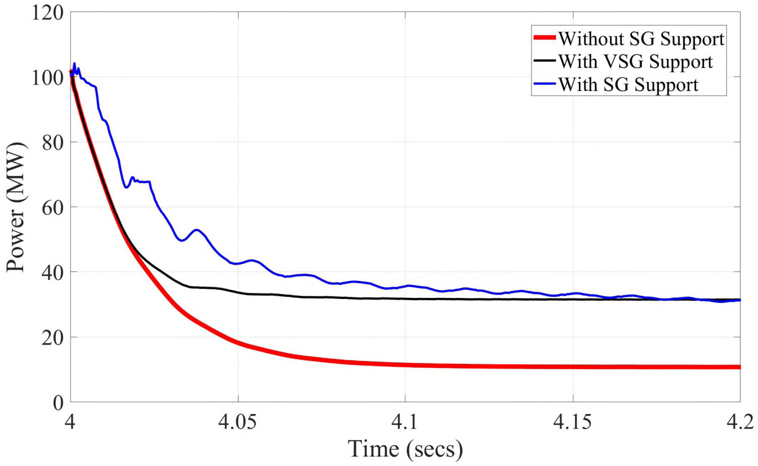

Figure 15. Active power support during a 3-phase fault for SCR = 4

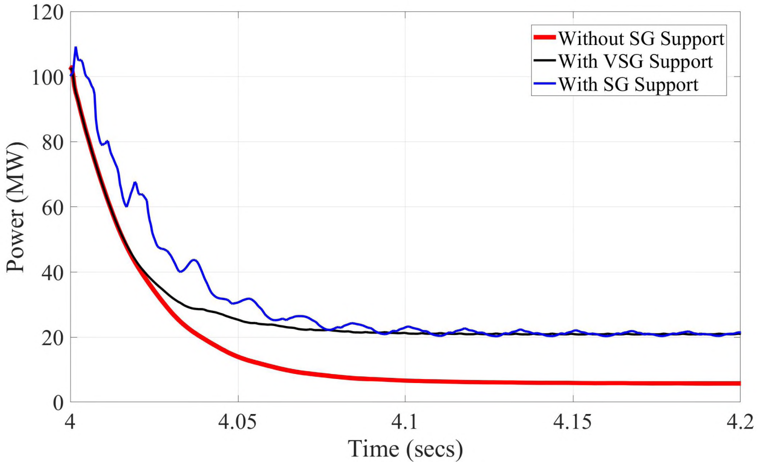

Figure 16. Active power support during a 3-phase fault for SCR = 2

It is observed from Figure 15, that for the SCR case 4, the active power provided by the MARS system with SG-based control method is higher than the active power provided by the VSG-based control method untill 4.15 s and becomes equal at 4.2 s. From Figure 16, for the SCR case 2, the active power provided by the MARS system with the SG-based control method is higher than the active power provided by the VSG-based control method untill 4.075 s and becomes equal at 4.1 s. The increase in voltage profiles for SCR cases 2, 4, and 10 can be attributed to the corresponding reactive power profiles. From Figure 17 - Figure 19, it can be observed that the reactive power provided by the MARS system using

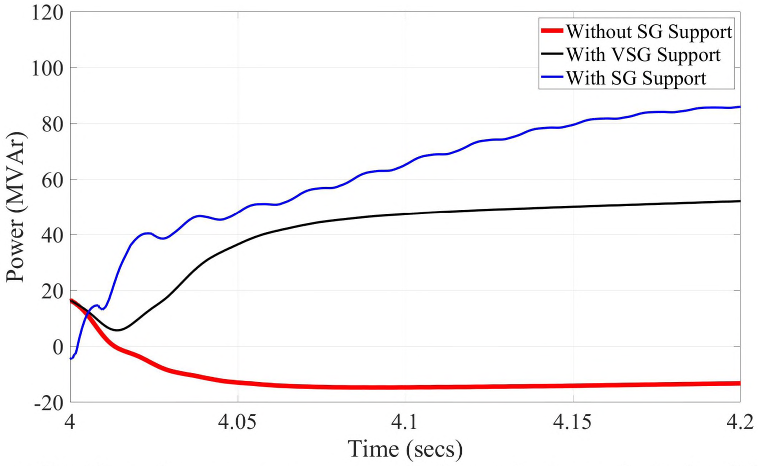

Figure 17. Reactive power support during a 3-phase fault for SCR = 10

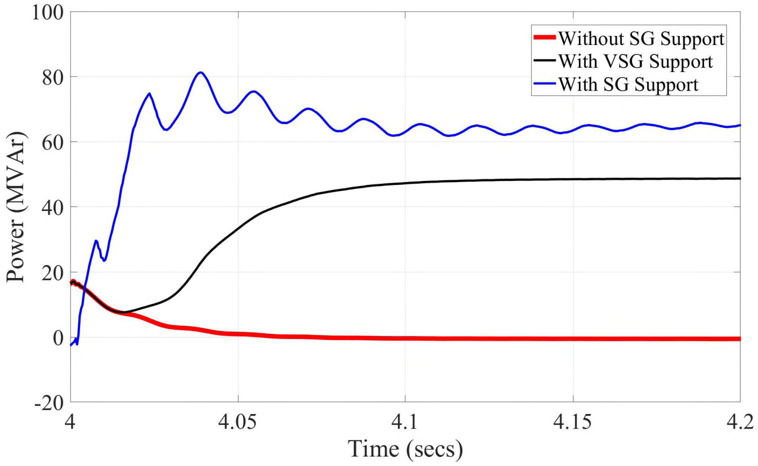

Figure 18. Reactive power support during a 3-phase fault for SCR = 4

the SG-based control method is greater than the reactive power provided by the MARS system using the VSG-based control method. For the SCR = 0.5 case, the voltage response provided by the VSG-based control method resulted in unstable operation while the voltage response provided by the SG-based control method resulted in stable operation. This is because the interactions between the PLL and the VSG-based controller lead to stability issues.

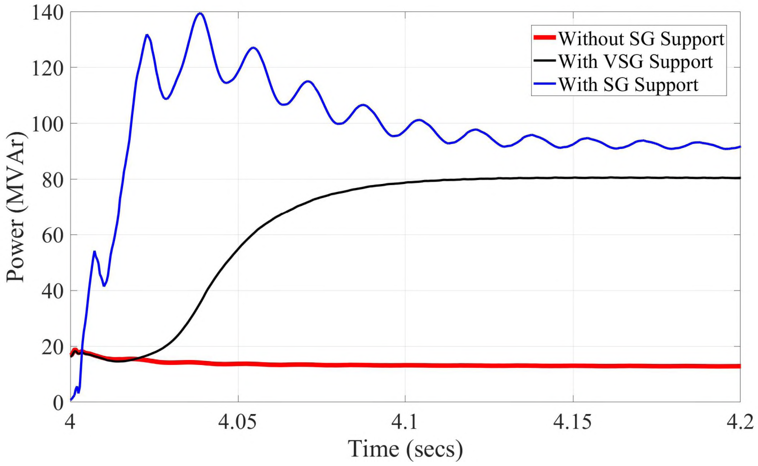

Figure 19. Reactive power support during a 3-phase fault for SCR = 2

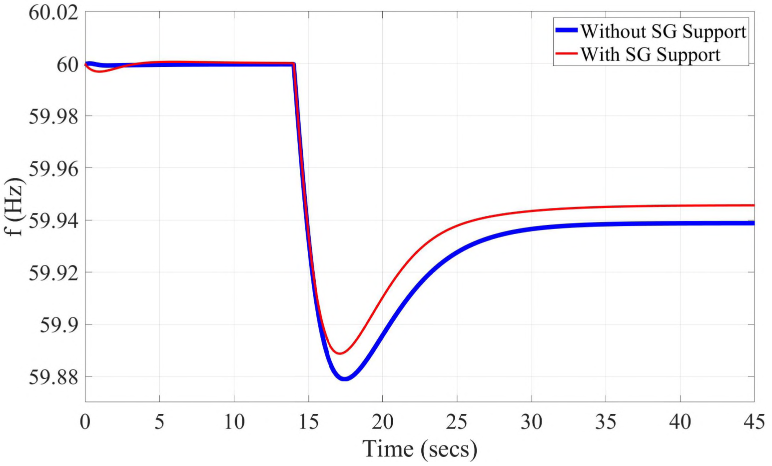

Figure 20. Grid frequency response for LOG in WECC for SCR = 0.5 and H = 11 secs.

6.2.3. Use Case 3: 804.44 Loss of Generation in Low SCR and Low Inertia System. For the operating condition P_{ac} = P_{dc} = 100 MW, SCR = 0.5, and H = 11 secs, the LOG event detailed in Section 6.2.1 is tested. The grid frequency response for SCR = 0.5 and H = 11 secs is shown in Figure 20. The improvement in the frequency nadir is 8.10 % and improvement in steady state is 11.19 %.

6.3. OPAL-RT MODEL SIMULATION

The OPAL RT model consists of a frequency-controlled voltage source, 2 pi-line sections, a synchronverter based controller, and the reduced-order model of the MARS system. The model is shown in Figure 9.

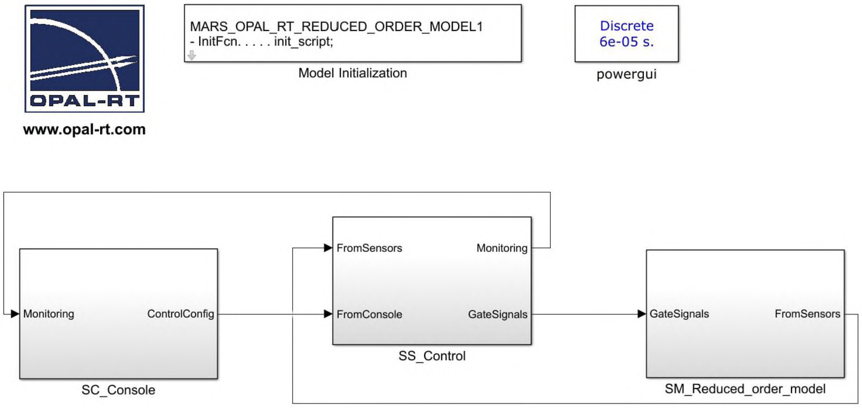

Figure 21. OPAL-RT Model

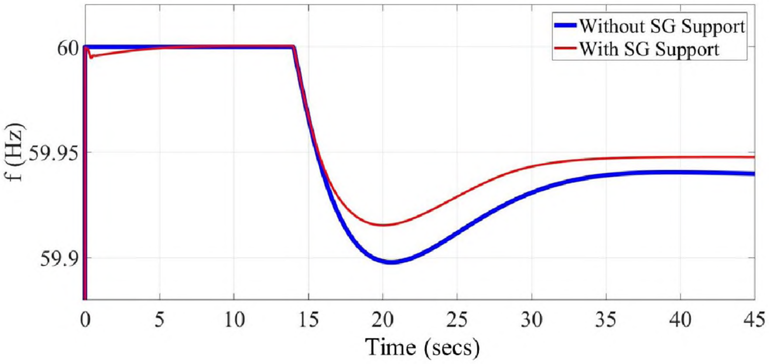

Figure 22. Grid frequency response for LOG in WECC for SCR = 10 using the OPAL-RT simulation model.

The pi-line section is tuned after disconnecting the reduced-order model and is based on the contingency results of a line-to-line fault at Gates near Pittsburg in the 179-bus WECC model in PSCAD. The ac grid model is modeled the same as the one utilized in the

PSCAD simulation (i.e. WSEIG1) [13]. The grid frequency response for the same use case described in Section 6.2.1 for SCR = 10 case is shown in Figure 22. The improvement in the frequency nadir is 17.12 % and improvement in steady state is 13.11 %.

7. FUTURE WORK

The performance of the synchronverter during unbalanced faults is a research avenue yet to be explored and still poses an open question [15]. One of the key challenges during the unbalanced faults is to capture the rapidly varying ac side voltage dynamics. The inability to accurately capture ac side voltage dynamics results in unreasonable ac side grid currents. Synchronverter performance during the unbalanced faults is studied in [15] and [16] to an extent. Advanced control methods are needed to provide stable operations under unbalanced faults.

8. CONCLUSION

This paper presents the synchronverter algorithm and control architecture of the MARS system to provide support to ac grid under different events in the grid. The SG-based control algorithm is proposed to support the ac grid frequency and voltage during disturbances in the grid. In addition, a brief description of the overall control architecture of the MARS system is presented. The proposed control algorithm and the MARS control architecture is evaluated and validated for the MARS system at Pittsburg in a PSCAD/EMTDC simulation environment. OPAL-RT offline simulation models required to perform the cHIL tests are also developed. The developed models and proposed control algorithm were tested for different grid scenarios. To summarize the results, for the specific study system considered in this paper, the MARS system with the SG-based control provides better frequency support in terms of higher frequency nadir and higher frequency steady state during frequency excursions in comparison to the VSG-based control method. Also the MARS systems with SG-based control provide better voltage support by injecting more reactive power into the system during balanced phase faults in comparison to the VSG-based control method. The key takeaway point identified from this research endeavor is that for the specific study system considered in this paper, the SG-based control method is more stable and gives better performance in terms of frequency nadir and steady state improvement. For the voltage response, the SG-based control method is better than the VSG-based control method for different SCR conditions tested.

ACKNOWLEDGEMENT

This paper is based upon work supported by the U.S. Department of Energy's Office of Energy Efficiency and Renewable Energy (EERE) under Solar Energy Technologies Office (SETO) Agreement Number 34019. Authors would like to thank Dr. Jiuping Pan, Dr. Jian Fu, Dr. Hariharan Krishnaswami, and Dr. John Seuss for overseeing the project developments and providing guidance.

REFERENCES

[1] S. Debnath and M. Chinthavali, "Control of MMC-HVdc in low-inertia weak grids," in *Proc. 2017 IEEE 12th International Conference on Power Electronics and Drive Systems (PEDS)*, pp. 435–441.

[2] S. Debnath, J. Qin, B. Bahrani, M. Saeedifard, and P. Barbosa, "Operation, control, and applications of the modular multilevel converter: A review," *IEEE Transactions on Power Electronics*, vol. 30, pp. 37–53, Jan 2015.

[3] Q. Zhong and G. Weiss, "Synchronverters: Inverters that mimic synchronous generators," *IEEE Transactions on Industrial Electronics*, vol. 58, pp. 1259–1267, April 2011.

[4] Q. Zhong, P. Nguyen, Z. Ma, and W. Sheng, "Self-synchronized synchronverters: Inverters without a dedicated synchronization unit," *IEEE Transactions on Power Electronics*, vol. 29, no. 2, pp. 617–630, 2014.

[5] M. Amin, A. Rygg, and M. Molinas, "Self-synchronization of wind farm in an MMC-based HVdc system: A stability investigation," *IEEE Transactions on Energy Conversion*, vol. 32, no. 2, pp. 458–470, 2017.

[6] M. Amin and M. Molinas, "Self-synchronisation of wind farm in MMC-based HVdc system," in *Proc. 2016 IEEE Electrical Power and Energy Conference (EPEC)*, pp. 1–6.

[7] U. Tamrakar, D. Shrestha, M. Maharjan, B. P. Bhattarai, T. M. Hansen, and R. Tonkoski, "Virtual inertia: Current trends and future directions," *Applied Sciences*, vol. 7, no. 7, p. 654, 2017.

[8] M. P. N. Van Wesenbeeck, S. W. H. De Haan, P. Varela, and K. Visscher, "Grid tied converter with virtual kinetic storage," in *Proc. 2009 IEEE Bucharest PowerTech*, pp. 1–7.

[9] S. Debnath and M. Chinthavali, "Numerical-stiffness-based simulation of mixed transmission systems," *IEEE Transactions on Industrial Electronics*, vol. 65, pp. 9215–9224, Dec 2018.

[10] S. Debnath and M. Chinthavali, "MMC-HVdc: Simulation and control system," in *Proc. 2016 IEEE Energy Conversion Congress and Exposition (ECCE)*, pp. 1–8.

[11] P. Krause, O. Wasynczuk, S. Sudhoff, S. Norrga, and S. Pekarek, *Analysis of Electric Machinery and Drive Systems*. Wiley-IEEE Press, 2013.

[12] H. Knaak, "Modular multilevel converters and HVdc/FACTS: A success story," in *Proc. 2011 14th European Conference on Power Electronics and Applications*, pp. 1–6.

[13] S. Debnath and J. Sun, "Fidelity requirements with fast transients from VSC-HVdc," in *Proc. IECON 2018 - 44th Annual Conference of the IEEE Industrial Electronics Society*, pp. 6007–6014.

[14] WECC Renewable Energy Modeling Task Force, "WECC Solar Plant Dynamic Modeling Guidelines," 2014.

[15] Z. Shuai, W. Huang, C. Shen, J. Ge, and Z. J. Shen, "Characteristics and restraining method of fast transient inrush fault currents in synchronverters," *IEEE Transactions on Industrial Electronics*, vol. 64, no. 9, pp. 7487–7497, 2017.

[16] M. Wang, H. Li, and L. Li, "Fault through technique of synchronverter based on voltage feedforward compensation," in *Proc. 2018 International Conference on Power System Technology (POWERCON)*, pp. 2056–2061.

II. MODEL BASED PREDICTIVE CONTROL FOR FREQUENCY SUPPORT IN MULTI-PORT AUTONOMOUS RECONFIGURABLE SOLAR PLANTS

ABSTRACT

Primary frequency support functionality can be an added advantage for any new grid integrated power electronics resource. With increased penetration of power electronic based resources, inertial and primary frequency response capabilities are decreasing. In this research paper, an advanced model-based predictive control (MBPC) algorithm for providing frequency support to a new topology of integrated photovoltaic (PV), battery-based energy storage systems (ESS), and high-voltage direct current (HVdc) systems called multi-port autonomous reconfigurable solar (MARS) plants is proposed. The proposed control algorithm for frequency support is based on the synchronverter-based control. The simulation of a MARS-HVdc system with the proposed control strategy is simulated and validated for MARS connected to low short circuit ratio (SCR) grids in the PSCAD/EMTDC simulation environment. The control algorithm proposed showcases better performance in terms of frequency nadir improvement and frequency steady state improvement with respect to no frequency control.

Keywords: Synchronverter, HVdc, MMC, VSG, MPC

1. INTRODUCTION

One of the concerns with power electronic based systems with renewable energy integration is reduction in the overall inertia of the grid. This is because the power electronics-based systems have no physical inertia in comparison to conventional power systems. Virtually strengthening the system with inertia through advanced control methods is one of the solutions towards stabilizing the grid in the case of frequency related events.

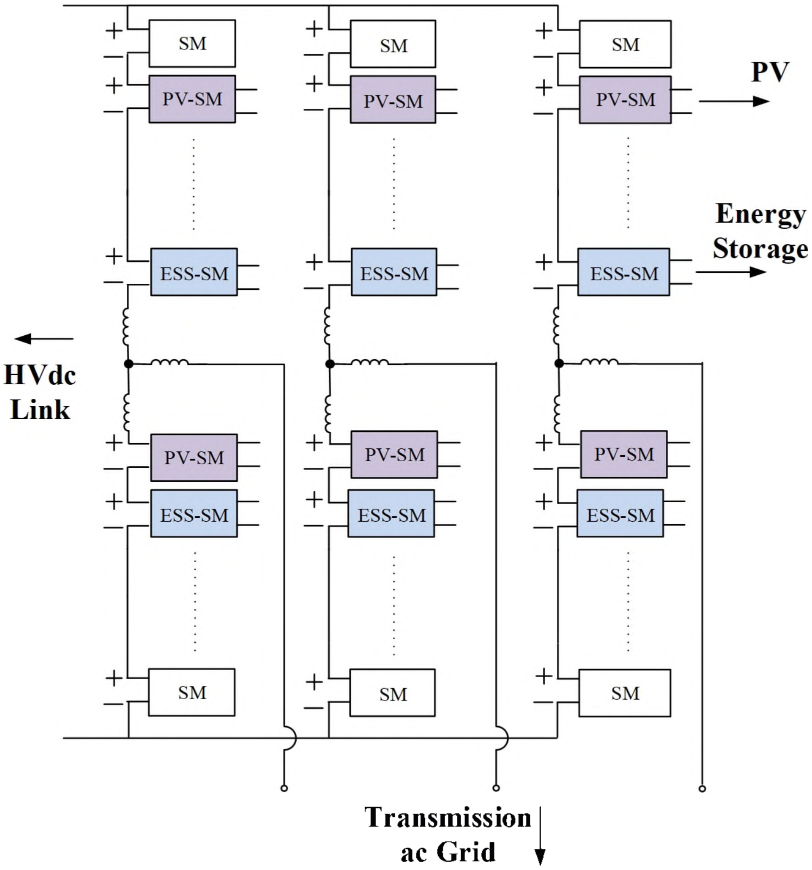

Figure 1. Overview of the MARS system architecture

The key goal of this paper is to propose a model-based predictive control (MBPC) based advanced control scheme that can provide frequency support during unforeseen frequency deviations. In comparison to conventional control methods, MBPC is chosen for frequency support due to its inherent advantages such as inclusion of constraints, system state prediction, and better dynamic performance [1] [2]. The proposed MBPC-based control method is part of a novel power electronics resource-based system called Multi-port Autonomous Reconfigurable Solar Plants (MARS) [3]. The MARS system is an integrated development for photovoltaic (PV) and battery-based energy storage systems (ESS) connected to alternating current (ac) transmission grid and high-voltage direct current (HVdc) links as shown in Figure 1.

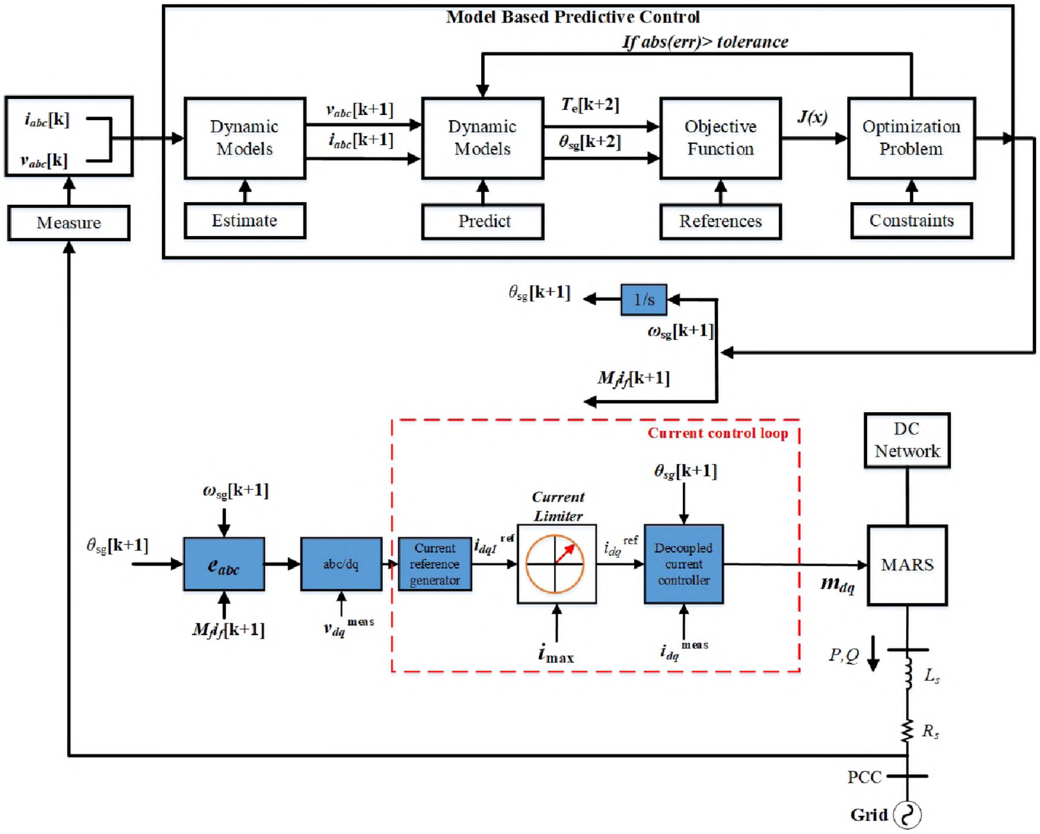

Figure 2. MBPC-based control for the MARS system

The control architecture of the MARS system is hierarchical in nature and highly complex. It consists of three layers with different functionalities. Firstly, the upper-level (L-1) controller incorporates the active power control, reactive power control, MBPC-based frequency control, ac-side voltage control, and dc-side voltage control. Second, the intermediate-level (L-2) controller consists of capacitor voltage balancing control and ESS and PV cumulative power control. Lastly, the lower-level (L-3) control comprises of maximum power point tracking (MPPT) control for PV sub modules (SMs) and state of charge (SOC) control for ESS SMs. In this research work, MBPC-based control method for frequency support in L-1 controller is proposed.

Synchronverters mimic synchronous generator's properties in providing frequency support and voltage support. The frequency and voltage models used in the objective function of MBPC-based control method are modeled based on the synchronous generator model. The proposed optimization problem solves for angular frequency (ω_{sg}). The proposed control architecture is tested on advanced high-fidelity three-phase MARS system models that utilize ultra-fast simulation algorithms connected to reduced-order ac grid models [3] [4]. The MARS test system (that consists of 250 SMs in an arm and 1500 SMs in total) is based on upgrades in the Trans-Bay Cable project in Pittsburg, California. The effectiveness of the proposed control algorithm is tested and evaluated for different test cases in PSCAD/EMTDC simulation environment.

2. MODEL PREDICTIVE CONTROL

2.1. AN OVERVIEW

The block diagram for the MBPC-based synchronverter control is shown in Figure 2. It includes the dynamic models to estimate and predict system states, an objective function to translate control goals into a scalar cost value, and an optimization problem to minimize the objective function. The idea of MBPC-based synchronverter control is to generate optimal values of ω_{sg} by minimizing the objective function. The details regarding each block are provided in the following sections.

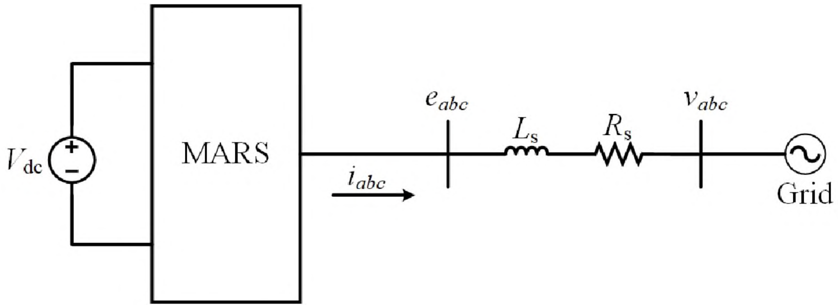

Figure 3. Single-line diagram of MARS connected to grid

2.2. MODEL FORMULATION

2.2.1. MARS-HVdc Internal Dynamic Model. A single-line diagram of the MARS system connected to the grid is shown in Figure 3. The MARS system is a three-phase system with a total of six arms that integrate PV and ESS using power electronics and can connect to HVdc and the high-voltage transmission ac grid. Each arm consists of normal SMs, PV, and ESS-SMs along with an arm inductance (L_o) and an arm resistance (R_o). The PV systems in each PV-SM are connected to the SM through either isolated or non-isolated dc-dc converter. The ESS systems in each ESS-SM are connected through a bidirectional dc-dc converter. Each phase of the converter is interfaced with the utility grid via a series RL branch (R_s and L_s) [5]. In this section, a dynamic continuous-time model and a discrete-time model of the MARS system based on the discretization of the continuous-time model are developed. The developed discrete model is used in the digital implementation of the MBPC method. The equivalent reduced order model schematic of MARS system is illustrated in Figure 4.

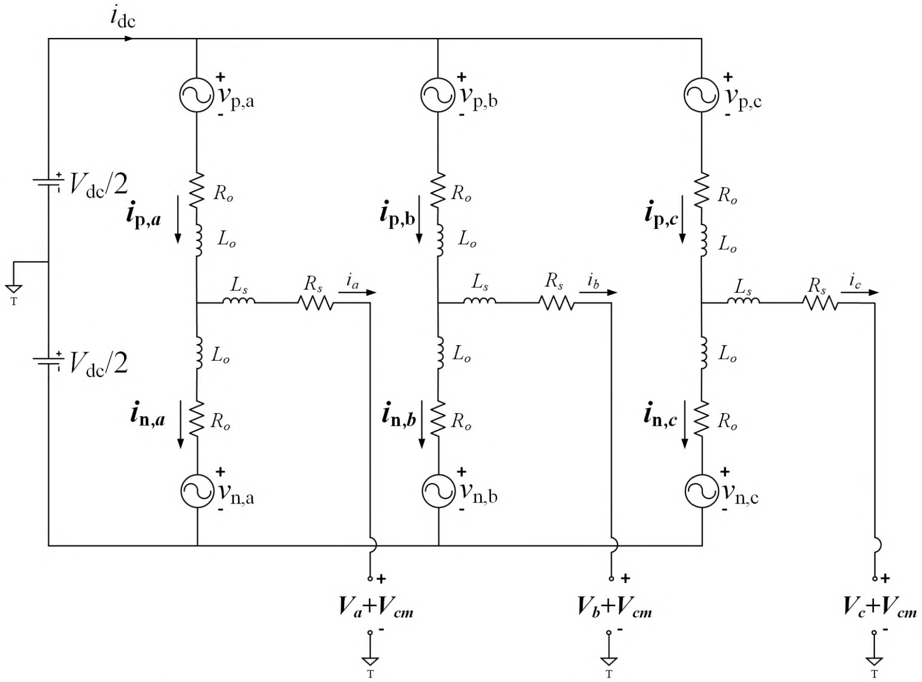

Figure 4. MARS reduced order model schematic

The upper arm voltage ($v_{\mathrm{p},j}$) and lower arm voltage ($v_{\mathrm{n},j}$) of phase-j are given by:

$$v_{\mathrm{p},j} = V_{\mathrm{dc}} - L_{\mathrm{o}}\frac{\mathrm{d}i_{\mathrm{p},j}}{\mathrm{d}t} - R_{\mathrm{o}}i_{\mathrm{p},j} - L_{\mathrm{s}}\frac{\mathrm{d}i_j}{\mathrm{d}t} - R_{\mathrm{s}}i_j - v_j - v_{\mathrm{cm}}, \forall j \in (a, b, c), \tag{1a}$$

$$v_{\mathrm{n},j} = V_{\mathrm{dc}} - L_{\mathrm{o}}\frac{\mathrm{d}i_{\mathrm{n},j}}{\mathrm{d}t} - R_{\mathrm{o}}i_{\mathrm{n},j} + L_{\mathrm{s}}\frac{\mathrm{d}i_j}{\mathrm{d}t} + R_{\mathrm{s}}i_j + v_j + v_{\mathrm{cm1}}, \forall j \in (a, b, c), \tag{1b}$$

where V_{dc} is the dc side voltage, and $v_{\mathrm{cm1}} = v_{\mathrm{cm}} - V_{\mathrm{dc}}$; $i_{\mathrm{p},j}$ and $i_{\mathrm{n},j}$ are the upper arm and lower arm currents

The dynamic continuous-time model of MARS system shown in Figure 3 is given by (1) and is obtained by adding (1a) and (1b) with the following assumptions: (i) SM capacitor voltages are balanced; and (ii) common mode voltages (v_{cm} and v_{cm1}) are neglected:

$$(L_s + L_o/2)\,\frac{\mathrm{d}i_j}{\mathrm{d}t} + (R_s + R_o/2)\,i_j = e_j - v_j, \forall j \in (a, b, c) \tag{2}$$

where i_j are the three phase grid currents; v_j are the three phase grid voltages, and the three phase output voltage (e_j) of the MARS system is given by

$$e_j = \frac{-v_{\mathrm{p},j} + v_{\mathrm{n},j}}{2}, \forall j \in (a, b, c)$$

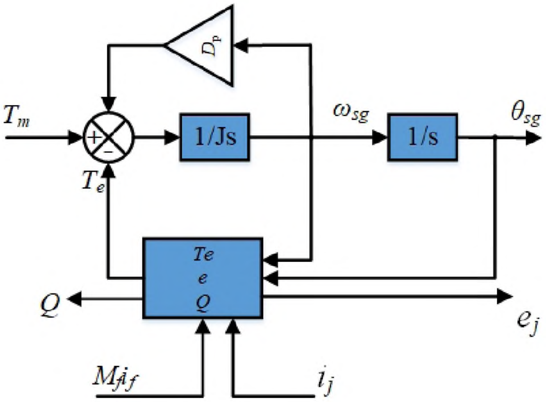

Figure 5. Synchronverter control block

The discrete-time model of the MARS system is obtained by discretizing (1) using the forward-Euler method and is given by:

$$i_a[k] = \left(1 - h\frac{R_s + R_o/2}{L_s + L_o/2}\right)(i_a[k-1]) + \frac{h}{L_s + L_o/2}(e_a[k-1] - v_a[k-1]) \tag{3a}$$

$$i_b[k] = \left(1 - h\frac{R_s + R_o/2}{L_s + L_o/2}\right)(i_b[k-1]) + \frac{h}{L_s + L_o/2}(e_b[k-1] - v_b[k-1]) \tag{3b}$$

$$i_c[k] = \left(1 - h\frac{R_s + R_o/2}{L_s + L_o/2}\right)(i_c[k-1]) + \frac{h}{L_s + L_o/2}(e_c[k-1] - v_c[k-1]) \tag{3c}$$

where h is the simulation time – step and k is the time instant.

2.3. SYNCHRONVERTER BASED FREQUENY MODEL

The frequency model is based on the synchronverter model. Synchronverters mimic synchronous generator's properties in providing frequency support and voltage support during grid events that lead deviations in frequency or voltage [6]. The synchronverter-based (SG-based) control block is derived using the mathematical model of the three-phase round rotor synchronous generator [6] and [7] and is shown in Figure 5.

The discrete-time representation of electromagnetic torque (T_e), e_j, and reactive power (Q) are given in

$$T_e[k] = M_f i_f[k](i_a[k]\cos(\theta_{sg}[k]) + i_b[k]\cos(\theta_{sg}[k] - 2\pi/3) + i_c[k]\cos(\theta_{sg}[k] - 4\pi/3)) \tag{4a}$$

$$\begin{aligned} e_a[k] &= \omega_{sg}[k]M_f i_f[k]\cos(\theta_{sg}[k]) \\ e_b[k] &= \omega_{sg}[k]M_f i_f[k]\cos(\theta_{sg}[k] - 2\pi/3) \\ e_c[k] &= \omega_{sg}[k]M_f i_f[k]\cos(\theta_{sg}[k] - 4\pi/3) \end{aligned} \tag{4b}$$

$$\begin{aligned} Q[k] = {} & -\omega_{sg}[k]M_f i_f[k] i_a[k]\sin(\theta_{sg}[k]) + i_b[k]\sin(\theta_{sg}[k] - 2\pi/3) \\ & + i_c[k]\sin(\theta_{sg}[k] - 4\pi/3) \end{aligned} \tag{4c}$$

where $M_{\mathrm{f}}i_{\mathrm{f}}$ in (4) is control input to the synchronverter [6]. From Figure 5, the rotor angle (θ_{sg}) can be calculated by

$$\theta_{\mathrm{sg}}[k] = \theta_{\mathrm{sg}}[k-1] + h\omega_{\mathrm{sg}}[k-1] \tag{5}$$

The frequency dynamics of the system are represented by the discrete-time model represented by

$$\omega_{\mathrm{sg}}[k] = \omega_{\mathrm{sg}}[k-1]\left(1 - \frac{h\mathrm{D_p}}{J}\right) + \frac{h}{J}\left(T_{\mathrm{m}}[k] - T_{\mathrm{e}}[k] - \mathrm{D_p}\left(\omega_{\mathrm{n}}[k]\right)\right) \tag{6}$$

where J is the moment of inertia, T_{m} is the mechanical torque, $\mathrm{D_p}$ is the damping factor, and ω_{n} is the reference angular frequency .

2.4. OBJECTIVE FUNCTION

The objective function based on the discrete-time models modeled in the earlier sections is given by

$$\begin{aligned}
&\min_{x} \quad J(x) \\
\text{s.t.} \quad & \mathbf{e}[k+1] = \omega_{\mathrm{sg}}[k+1]M_{\mathrm{f}}i_{\mathrm{f}}[k](\cos(\widetilde{\theta_{\mathrm{sg}}[\mathbf{k}+\mathbf{1}]})) \\
& \theta_{\mathrm{sg}}[k+1] = \theta_{\mathrm{sg}}[k] + h\omega_{\mathrm{sg}}[k] \\
& T_{\mathrm{e}}[k+2] = M_{\mathrm{f}}i_{\mathrm{f}}[k] < \mathbf{i}[k+2], (\cos(\widetilde{\theta_{\mathrm{sg}}[\mathbf{k}+\mathbf{2}]})) >; \\
& T_{\mathrm{m}}[k+2] = \frac{P_{\mathrm{ac,ref}}[k+2]}{\omega_{\mathrm{n}}[k+1]};
\end{aligned} \tag{7}$$

where x and $J(x)$ are given by

$$\begin{aligned}
x &= \left(\omega_{\mathrm{sg}}[k+1]\right)^T \\
J(x) &= J_1(x) + J_2(x)
\end{aligned} \tag{8}$$

where

$$J_1(x) = \lambda_1 \left(T_e[k+2] - T_m[k+2]\right)^2$$

$$J_2(x) = \lambda_2 \left(\omega_n[k+1] - \omega_{sg}[k+1]\right)^2$$

where λ_1, and λ_2 are the weights of the cost function; $P_{ac,ref}$ is the ac side power dispatch command; and the vectors $\mathbf{i}$, $\widetilde{\cos(\theta)}$, and $\widetilde{\sin(\theta)}$ are defined in [6].

2.5. TORQUE CONTROL

The quadratic cost function definition for torque control is given by $J_1(x)$. T_e is calculated using (4a) and is predicted at the $(k+2)^{th}$ instant. T_e is controlled to regulate the active power in the system during frequency excursions. Whenever the electrical load in the system increases or decreases (equivalently electrical generation decreases or increases), the system frequency decreases or increases. In this case, T_e increases or decreases accordingly with the system frequency change. To compensate for the increased or decreased T_e, optimal active power is injected into the system based on the deviation in ω_{sg} with respect to ω_n.

2.6. ANGULAR FREQUENCY CONTROL

The quadratic cost function for angular frequency control is given by $J_2(x)$. The angular frequency control emulates the frequency droop property of synchronous generators. ω_{sg} at $[k+1]^{th}$ instant is obtained based on optimizing (T_e -T_m) at the $[k+2]^{th}$ instant.

2.7. IMPLEMENTATION FOR PROPOSED CONTROL METHOD

The implementation for the SG-based MBPC is briefly explained in this section. i_j and v_j are measured from the ac grid models used in the simulation at the $[k]^{th}$ instant. Once the i_j is measured at the $[k]^{th}$ instant, using the dynamic model in (3) the i_j at $[k+1]^{st}$ instant is estimated. As the variation of v_j is slower compared to the MARS system dynamics, in this implementation the v_j at the $[k+1]^{st}$ instant are assumed to be equal to the v_j at the $[k]^{th}$ instant. θ_{sg} at the $[k+1]^{st}$ is estimated based on (3). Then, T_{e} at the $[k+2]^{th}$ instant is predicted using (4a). The predicted state is included in the cost function $J(x)$ and it is then minimized using an unconstrained optimization to obtain the optimal value $\omega_{\mathrm{sg}}[k+1]$. In predicting T_{e} at the $[k+2]^{th}$ instant, the initial guess for ω_{sg} at the $[k+1]^{st}$ instant is ω_{sg} at the $[k]^{th}$ instant. Based on the optimal value, e_j is updated and qd frame reference currents ($i_{\mathrm{qd,ref}}$), phase, and arm modulation indices (m_j and m_j^y) are generated that are sent to L-2 controller in the MARS system based on the decoupled current controller implementation detailed in [7].

2.8. UNCONSTRAINED OPTIMIZATION

The cost function $J(x)$ is minimized using Newton's method described in [8]. The $\omega_{\mathrm{sg}}[k+1]$ at every time step is calculated by the following recursive formula for the $(n+1)^{st}$ iteration given

$$x[k+1]^{(n+1)} = x[k+1]^{(n)} - F\left(x[k+1]^{(n)}\right)^{-1} g[k+1]^{(n)} \tag{9}$$

where

$$F\left(x[k+1]^{(n)}\right) = \left[\frac{\partial g[k+1]^{(n)}}{\partial x[k+1]}\right]; g[k+1]^{(n)} = \left[\frac{\partial J\left(x[k+1]^{(n)}\right)}{\partial x[k+1]}\right];$$

3. SIMULATION RESULTS & VALIDATION

3.1. TESTING SYSTEMS

The proposed algorithm is tested on a MARS system that is being developed for Pittsburg, California. This test system is based on upgrades to the TransBay Cable project in Pittsburg, California [9]. There are 111 PV, 37 ESS, and 81 normal SMs per arm in this test system. The PV and ESS are rated at 150 kW, 1 kV. The size of the PV and the ESS

SMs are determined based on utilizing 200 A, 3.3 kV SiC devices in the dc-dc converters. The total number of SMs per arm are determined by the dc-link voltage in the location and based on the installed HVdc substation (in the TransBay Cable project).

3.2. USE CASES FOR MARS WITH ac GRID MODELS

Multi-level multi-rate MARS system Pittsburg models are developed. The dynamic model of the MARS system is connected to the dynamic model of the Western Interconnection (WI) grid. The ac grid in the WI is modeled based on WSEIG1 to accurately represent the frequency data available [10]. The short circuit ratio (SCR) of the connected ac grid to the MARS system is varied to evaluate the performance of the proposed control system in the MARS system. Different SCR conditions are emulated based on the variation of the transmission line lengths in the PSCAD simulation environment for the PSCAD simulation setup detailed in [7].

The following use case is identified and tested for the operating condition of P_{ac} = P_{dc} = 100 MW: 804.44 MW loss of generation at t = 14 s based on Haynes3 generator in the WI grid. An event of 804.44 MW loss of generation (LOG) in the western electric

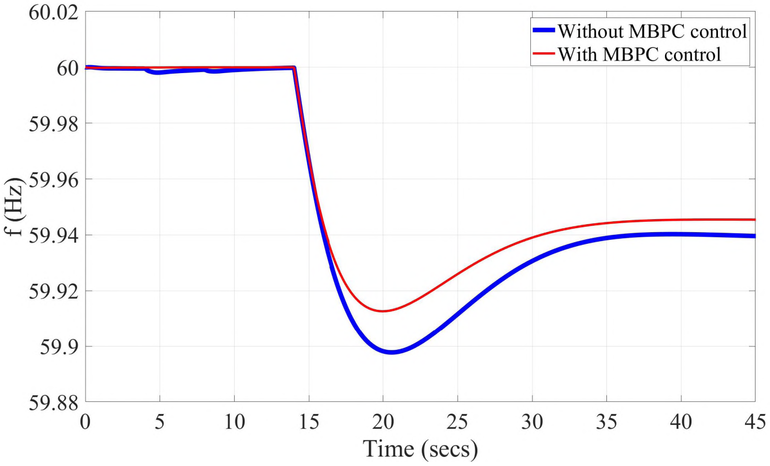

Figure 6. Grid Frequency response for LOG in WECC for SCR = 10

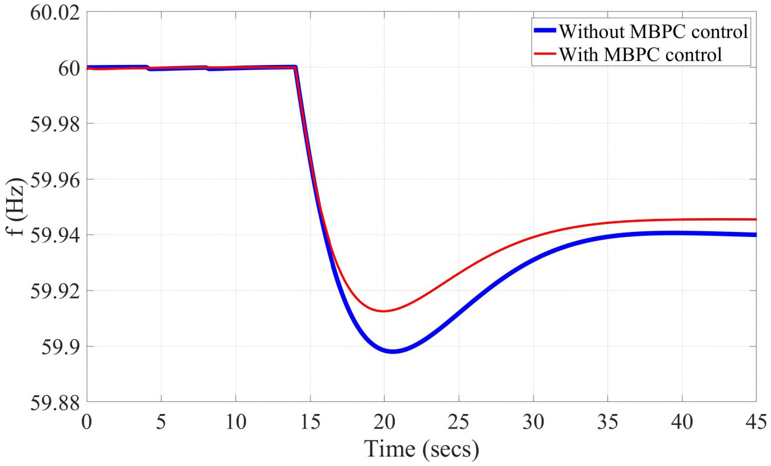

Figure 7. Grid Frequency response for LOG in WECC for SCR = 4

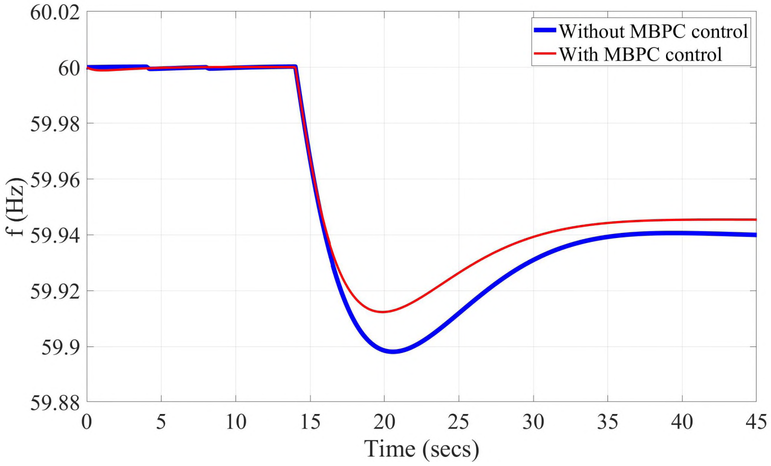

Figure 8. Grid Frequency response for LOG in WECC for SCR = 2

coordinating council (WECC) is simulated at t = 14 s. The frequency response measured at Pittsburg for different SCR cases without support and with MBPC-based support from the MARS system are shown in Figure 6 - Figure 9. The frequency improvements in nadir and steady state for each SCR condition and for each type of controller are tabulated in Table 1.

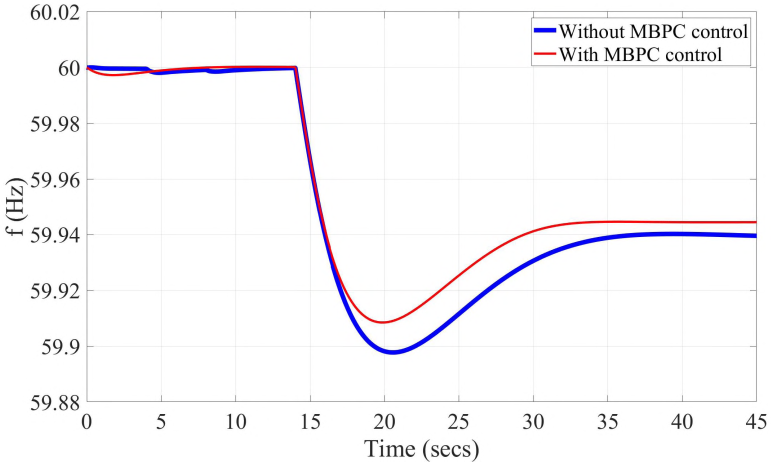

Figure 9. Grid Frequency response for LOG in WECC for SCR = 0.5

Table 1. Improvement in frequency response for different SCRs

SCR	Improvements	
	MBPC-based method	
	nadir	steady state
0.5	8.29 %	6.04 %
2	13.96 %	9.10 %
4	14.19 %	9.19 %
10	14.53 %	9.73 %

4. CONCLUSION

This paper presents the MBPC-based control algorithm for the MARS system to provide support to the ac grid when frequency changes are observed in the grid. The MBPC-based control is based on a synchronverter-based control algorithm. The proposed control algorithm and the MARS system control architecture is evaluated on a MARS system installed at Pittsburg, California on the PSCAD/EMTDC simulation environment. The simulation results showcase the improvement in frequency nadir and frequency steady state provided by the MARS system through MBPC control.

ACKNOWLEDGEMENT

This paper is based upon work supported by the U.S. Department of Energy's Office of Energy Efficiency and Renewable Energy (EERE) under Solar Energy Technologies Office (SETO) Agreement Number 34019. The authors would like to thank Dr. John Seuss for overseeing the project developments and providing guidance. The views expressed herein do not necessarily represent the views of the U.S. Department of Energy or the United States Government.

REFERENCES

[1] J. Rodriguez and P. Cortes, *Predictive Control of Power Converters and Electrical Drives.* Wiley-IEEE Press, 2012.

[2] S. Du, A. Dekka, Bin.Wu, and N. Zargari, *Analysis, Control, and Applications.* Wiley-IEEE Press, 2018.

[3] P. R. V. Marthi, S. Debnath, Q. Xia, and M. Saeedifard, "Advanced models and fast simulation algorithms for mars plants," in *Proc. 2020 IEEE/PES Transmission and Distribution Conference and Exposition (T & D)*, Chicago, Illinois, USA, pp. 1–5.

[4] S. Debnath and M. Chinthavali, "Numerical-stiffness-based simulation of mixed transmission systems," *IEEE Transactions on Industrial Electronics*, vol. 65, no. 12, pp. 9215–9224, Dec 2018.

[5] S. Debnath, P. Marthi, Q. Xia, J. Pan, M. Saeedifard, V. N. Vipin, S. Chakraborty, and M. Arifujjaman, "Renewable integration in hybrid ac-dc systems using multi-port autonomous reconfigurable solar power plant (MARS)," *IEEE Transactions on Power Systems*, pp. 1–1, 2020.

[6] Q. Zhong and G. Weiss, "Synchronverters: Inverters that mimic synchronous generators," *IEEE Transactions on Industrial Electronics*, vol. 58, no. 4, pp. 1259–1267, April 2011.

[7] P. R. V. Marthi, S. Debnath, and M. L. Crow, "Synchronverter-based control of multiport autonomous reconfigurable solar plants (MARS)," in *Proc. 2020 IEEE Energy Conversion Congress and Exposition (ECCE)*, pp. 5019–5026.

[8] E. K. P. Chong and S. H. Zak, *An Introduction to Optimization.* Wiley, 2004.

[9] H. Knaak, “Modular multilevel converters and HVDC/FACTS: A success story,” in *Proc. 2011 14th European Conference on Power Electronics and Applications*, pp. 1–6.

[10] S. Debnath and J. Sun, “Fidelity requirements with fast transients from VSC-HVdc,” in *Proc. IECON 2018 - 44th Annual Conference of the IEEE Industrial Electronics Society*, pp. 6007–6014.

III. A PREDICTIVE GRID FORMING CONTROL FOR MULTI-PORT AUTONOMOUS RECONFIGURABLE SOLAR PLANTS

ABSTRACT

In this paper, a new grid forming control for Multi-port Autonomous Reconfigurable Solar Plants (MARS) based on a model based predictive control (MBPC) methodology is proposed. The MARS system technology connects utility-scale photovoltaic (PV) plants and energy storage systems (ESSs) to high-voltage direct current (HVdc) lines and high-voltage alternating current (ac) grids. The proposed *grid forming* control for the MARS system uses an MBPC-based frequency support method and the synchronous generator based voltage support method. The performance and implementation of the proposed *grid forming* control algorithm in the MARS system is evaluated through offline simulations on the PSCAD/EMTDC simulation environment and real-time simulations on OPAL-RT platforms. Finally, the following analysis are provided in this paper: i) a theoretical proof of attaining the minima of the objective function using the proposed MBPC algorithm; and ii) a theoretical proof of convergence for the proposed MBPC-based frequency support in each time-step that indicates fast convergence.

Keywords: Synchronverter, HVdc, MMC, VSG, MPC

1. INTRODUCTION

The rapid decline in utility-scale solar photovoltaic (PV) costs [1], mandates from utilities to install energy storage systems (ESSs) [2], and the use of high-voltage direct current (HVdc) links to transfer renewables [3] [4] has led to the integrated development of PV and ESS connecting to HVdc links and high-voltage transmission alternating current (ac) grid. This technology is called as multi-port autonomous reconfigurable solar power plant

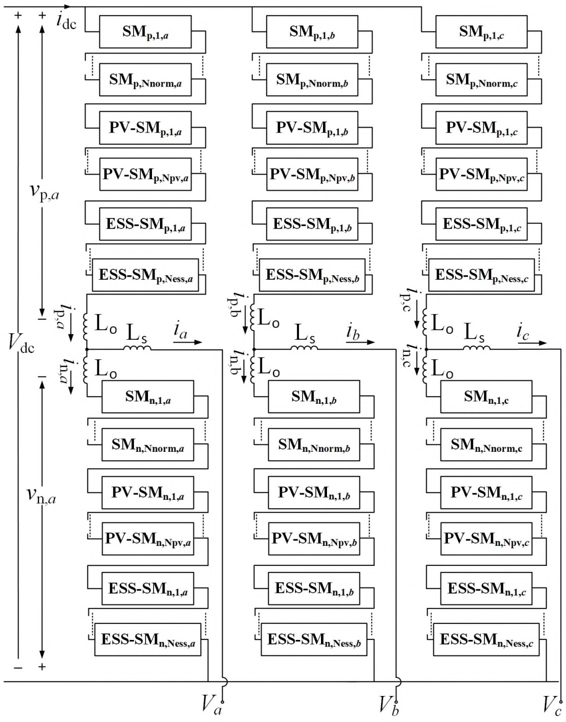

Figure 1. Overview of the MARS system architecture

(MARS) that is shown in Figure 1 [5]. The characteristics of the MARS system include: modularity; autonomous reconfigurability based on available energy; capability to provide enhanced support during ac grid disturbances; increased reliability and reduced losses as compared to discrete development of PV, ESS, and HVdc converters [5][6]; and reduced transient instabilities as compared to discrete development. Most of the power electronic-based (PE-based) systems like the MARS system employ *grid-following* control algorithms. Integrating PE-based resources which employ such control algorithms to low short circuit ratio (SCR) and low inertia systems might pose new control and stability challenges [7]. One of the potential solutions for enhanced stability and operation of PE-based resources is the inclusion of *grid forming* control methods.

Grid forming control based PE systems are defined as the systems that regulate instantaneous terminal voltages without help of phase-locked loop (PLL) [8]. *Grid forming* control methods can be mainly categorized into: a) synchronous generator (SG) based control; b) droop control; or c) virtual oscillators [8]. SG control methods employed in PE-based resources have been developed based on the strategies that emulate the inherent characteristics of conventional synchronous generators [6] [9] [10] [11]. Droop control-based PE systems utilize conventional frequency droop and voltage droop characteristics to regulate active and reactive powers [12]. In virtual oscillator controllers, the model used in the electronic stage of the PE-based system to modulate its power stage is based on the emulation of nonlinear oscillator circuit with a natural frequency that tracks the ac grid frequency [8] [13]. In this paper, a *grid forming* control method for MARS using model based predictive control (MBPC) for primary frequency support is proposed. The proposed control method operates under the following conditions: a) high penetration of PE-based generation; and b) remote integration of the MARS system to weak grids. The dynamics of frequency used in the proposed MBPC-based *grid forming* control strategy are based on a SG. The rationale to use MBPC methodology for *grid forming* control comes from following: a) ability to generate the optimal control states by estimating and predicting the future states; b) inclusion of constraints; and c) a simple and intuitive approach [14].

In the recent years, the MBPC-based *grid forming* method has been proposed for microgrids [15] [16], multi-terminal direct current (MTdc) grids [17], and power system testbeds [18] [19]. In [15], a MBPC-based control strategy is used to obtain the optimal ESS capacity by not violating the pre-fixed frequency limits in an islanded microgrid. The frequency models used in this study are derived based on the virtual inertia emulator, which is based on SG. The implementation of the MBPC is done using Matlab/Simulink toolbox and is not tested in real-time. Therefore, the computational complexity may be significant in real-time. In [16], a finite-set model predictive control (FS-MPC) is proposed to improve the voltage control. However, in this application the MBPC is not applied to improve the frequency response. The frequency support is provided by a traditional SG-based control. In the application of MBPC-based control in MTdc systems, a MBPC-based frequency control is proposed in [17]. In this application, the frequency at the ac bus is obtained by a

PLL, thus operating the voltage source converters (VSCs) in *grid following* mode rather than in *grid forming* mode. Centralized and decentralized MBPC-based *grid forming* control methods are proposed in [18] [19]. In these approaches, the MBPC methods calculate the additional power set-points during disturbances and send them to outer control loops which employ active power and reactive power droop laws rather than calculating the angular frequency (ω) directly. Furthermore, the computational burden imposed in solving the optimization problem in a real-time implementation may be high with these methods.

In this paper, a MBPC-based *grid forming* control method is proposed for the MARS system to provide inertial and primary frequency support in real-time for various SCR and inertia grids. The goal of the proposed MBPC-based control is to compute the optimal angular frequency (ω_{sg}) that inherently identifies the additional power required from the MARS system. The objective function ($J(x)$) consists of quadratic terms of electromechanical torque (T_{e}) and ω_{sg} deviations with respect to mechanical torque (T_{m}) and reference angular frequency (ω_{n}), respectively, at future time steps. The objective function is solved using a Newton's method to obtain the optimal ω_{sg} with minimal computational burden at each time step in real-time. Based on the optimal ω_{sg}, the references and variables required in the rest of the control algorithms are computed.

Additionally, this paper includes the following: a) theoretical proofs characterizing the proposed control method; and b) a comparison of the operation of MARS with both *grid forming* and *grid following* under various operating conditions.

The proposed control architecture is tested with high-fidelity three-phase MARS models connected to reduced-order ac grid models. The MARS test system (that consists of 250 SMs in an arm and 1500 SMs in total) is based on the Trans-Bay Cable project in Pittsburg, California. Comprehensive off-line simulations of the MARS-HVdc system with

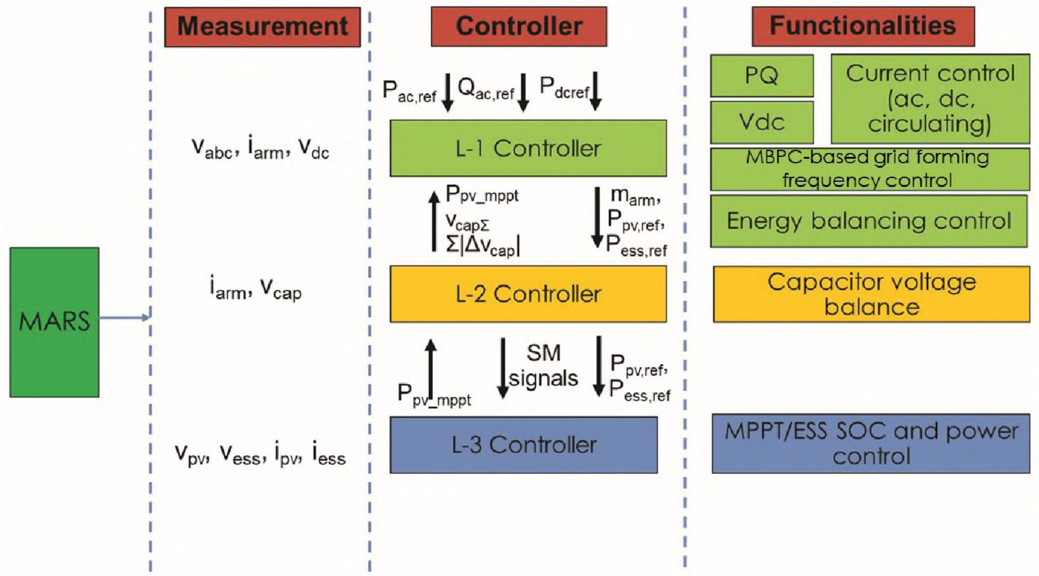

Figure 2. MARS system control architecture

the proposed control strategy are simulated in the PSCAD/EMTDC simulation environment. Finally, the effectiveness of the proposed control algorithms is tested and validated in real-time simulators under different operating conditions.

2. MARS HIGH-FIDELITY MODELS AND ITS CONTROL ARCHITECTURE

2.1. MARS SYSTEM HARDWARE ARCHITECTURE AND HIGH-FIDELITY MODELS

The MARS is a three-phase system with each phase consisting of two arms. Each arm consists of N_{norm} normal sub-modules (SMs), N_{pv} PV-SMs, and N_{ess} ESS-SMs along with arm inductance (L_{o}) and arm resistance (R_{o}), as shown in Figure 1. The PV systems in each PV-SM are connected to the SM through either an isolated or non-isolated dc-dc converter. The ESS systems in each ESS-SM are connected through a bidirectional dc-dc converters. Each phase of the converter is interfaced with the utility grid via a series RL branch (R_{s} and L_{s}) [5]. The high-fidelity MARS system models are developed based on the advanced simulation algorithms and techniques used in [20] [21].

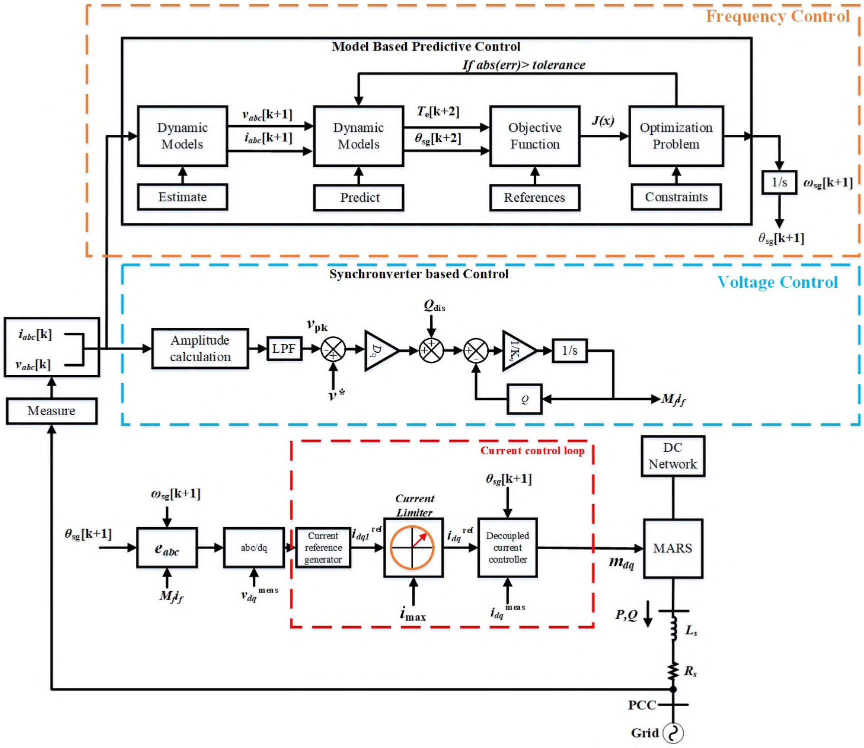

Figure 3. MBPC-based control for the MARS system

2.2. MARS SYSTEM CONTROL ARCHITECTURE

The MARS control system is hierarchical in nature and is shown in Figure 2. It consists of: (i) L-1 controller, (ii) L-2 controller, and (iii) L-3 controller. The functionalities of the L-1 controller are voltage and frequency support to the grid, active and reactive power control, dc-link voltage control, ac-/dc-side current control, and energy balance between different types of SMs (PV, ESS, and normal). The frequency control algorithm and voltage control algorithm are shown in Figure 3. The frequency support in the L-1 controller is based on the MBPC-based control algorithm that determines the ω_{sg}, and optimizes any additional power requirements dispatched by the MARS system. The control algorithm in the L-1 controller for voltage support generates additional reactive power based on the voltage deviations observed in the grid. Based on the additional reactive power requirement, the control algorithm, based on traditional SG control, then determines the required $M_f i_f$ used in the calculation of generated three-phase output voltage (e_{abc}). The reference active power commands of the PV and ESS ($P_{\mathrm{pv,ref}}$ and $P_{\mathrm{ess,ref}}$) depend upon the power dispatch commands ($P_{\mathrm{ac,ref}}$, and $P_{\mathrm{dc,ref}}$), the maximum available PV power ($P_{\mathrm{pv,mppt}}$), and the rating of the ESS SMs ($P_{\mathrm{ess,rating}}$). Based on the determined ω_{sg}, θ_{sg}, $M_{\mathrm{f}}i_{\mathrm{f}}$, and T_{m}, the qd current control of the ac-side currents are calculated to generate modulation indices (m_{abc}). Details about the energy balancing control, L-2 controller, and L-3 controller are given in [5] [6].

3. MODEL BASED PREDICTIVE CONTROL IN MARS

The block diagram of MBPC-based frequency control for the MARS system is shown in Figure 3. The MBPC-based control includes the following main parts: a) dynamic models to estimate and predict the variables; b) an objective function to evaluate the system control objectives; and c) an optimization to calculate the optimal control variables.

3.1. DYNAMIC MODELS

In this section, the dynamic models used in the MBPC-based control are described.

3.1.1. MARS System Models. Based on the reduced order model described in [20], the dynamic continuous-time model of the MARS system is given by

$$\left(L_s + \frac{L_o}{2}\right)\frac{\mathrm{d}i_j}{\mathrm{d}t} + \left(R_s + \frac{R_o}{2}\right)i_j = e_j - v_j, \quad \forall j \in (a, b, c) \tag{1}$$

where i_j are the phase$-j$ grid currents; v_j are the phase$-j$ grid voltages, and the phase$-j$ output voltage (e_j) of the MARS system is given by

$$e_j = \frac{-v_{\mathrm{p},j} + v_{\mathrm{n},j}}{2}, \quad \forall j \in (a, b, c)$$

3.1.2. SG-Based Frequency Dynamic Model. SG mimic synchronous generators' properties in providing frequency support and voltage support during grid events that lead to deviations in frequency or voltage[9]. The SG control block is derived using the mathematical model of the three-phase round rotor synchronous generator [9] and [6]. The discrete-time representation for T_e at time-step $k+2$, e_j at time-step $k+1$, and reactive power (Q) at time-step k are given by

$$\begin{aligned}
T_\mathrm{e}[k+2] &= M_\mathrm{f} i_\mathrm{f}[k](i_\mathrm{a}[k+2]\cos(\theta_\mathrm{sg}[k+2]) \\
&\quad + i_\mathrm{b}[k+2]\cos(\theta_\mathrm{sg}[k+2]-2\pi/3) \\
&\quad + i_\mathrm{c}[k+2]\cos(\theta_\mathrm{sg}[k+2]-4\pi/3)) \qquad (2a) \\
e_\mathrm{a}[k+1] &= \omega_\mathrm{sg}[k+1] M_\mathrm{f} i_\mathrm{f}[k]\cos(\theta_\mathrm{sg}[k+1]) \\
e_\mathrm{b}[k+1] &= \omega_\mathrm{sg}[k+1] M_\mathrm{f} i_\mathrm{f}[k]\cos(\theta_\mathrm{sg}[k+1]-2\pi/3) \qquad (2b) \\
e_\mathrm{c}[k+1] &= \omega_\mathrm{sg}[k+1] M_\mathrm{f} i_\mathrm{f}[k]\cos(\theta_\mathrm{sg}[k+1]-4\pi/3) \\
Q[k] &= -\omega_\mathrm{sg}[k] M_\mathrm{f} i_\mathrm{f}[k](i_\mathrm{a}[k]\sin(\theta_\mathrm{sg}[k]) \\
&\quad + i_\mathrm{b}[k]\sin(\theta_\mathrm{sg}[k]-2\pi/3) \\
&\quad + i_\mathrm{c}[k]\sin(\theta_\mathrm{sg}[k]-4\pi/3)) \qquad (2c)
\end{aligned}$$

where $M_\mathrm{f} i_\mathrm{f}$ in (2a)-(2c) is the control input to the SG [9]. The rotor angle (θ_sg) is calculated by

$$\theta_\mathrm{sg}[k+2] = \theta_\mathrm{sg}[k+1] + h\omega_\mathrm{sg}[k+1] \qquad (3)$$

where h is the integration step size and k is the current time instant.

The frequency dynamics of the system are given by the discrete-time model represented by

$$\begin{aligned}
\omega_\mathrm{sg}[k+2] =& \omega_\mathrm{sg}[k+1]\left(1-\frac{h\mathrm{D_p}}{J}\right) \qquad (4) \\
&+ \frac{h}{J}\left(T_\mathrm{m}[k+1] - T_\mathrm{e}[k+1] - \mathrm{D_p}\left(\omega_\mathrm{n}[k+1]\right)\right)
\end{aligned}$$

where J is the moment of inertia, T_m is the mechanical torque, $\mathrm{D_p}$ is the damping factor, and ω_n is the reference angular frequency.

3.2. OBJECTIVE FUNCTION

The control goal of MBPC-based frequency control is to generate an optimal ω_{sg} by solving the objective function using an optimization method. The objective function $J(x)$ is given by

$$J(x) = J_1(x) + J_2(x) \tag{5}$$

where

$$x = \left(\omega_{\mathrm{sg}}[k+1]\right)^T$$

$$J_1(x) = \lambda_1 \left(T_{\mathrm{e}}[k+2] - T_{\mathrm{m}}[k+2]\right)^2$$

$$J_2(x) = \lambda_2 \left(\omega_{\mathrm{n}}[k+1] - x\right)^2$$

and λ_1 and λ_2 are the weights of the cost function. The two main goals of the objective function in the proposed MBPC-based frequency control are: a) to track the ω_{sg} with respect to the reference angular frequency ω_{n}; and b) generate optimal changed torque T_{e} based on the deviations observed in the ω_{sg}. The first goal is realized by minimizing the quadratic error between ω_{sg} and ω_{n} and is defined by $J_2(x)$. The second goal is realized by minimizing the quadratic error between T_{m} and T_{e} and is defined by $J_1(x)$.

3.2.1. Torque Control. The quadratic cost function definition for torque control is given by $J_1(x)$. T_{e} is calculated using (2a) and is predicted at $(k+2)^{\mathrm{th}}$ instant. The electrical torque T_{e} is controlled to regulate the active power in the system during frequency excursions. Whenever the electrical load in the system increases or decreases (equivalently electrical generation decreases or increases), the system frequency decreases or increases. In this case, the T_{e} increases or decreases accordingly with the system frequency change. To compensate for the increased or decreased T_{e}, the angular frequency at the MARS system terminal needs to be changed.

3.2.2. Angular Frequency Control. The quadratic cost function for angular frequency control is given by $J_2(x)$. The goal is to reduce the variation of ω_{sg} with respect to ω_{n}, while maintaining T_{e} close to T_{m} simultaneously. The frequency ω_{sg} at the $[k+1]^{\mathrm{st}}$ instant is obtained based on optimizing $(T_{\mathrm{e}} - T_{\mathrm{m}})$ at the $[k+2]^{\mathrm{th}}$ instant.

3.3. OPTIMIZATION

The problem formulation for the objective function defined in (5) is given by

$$\begin{aligned} &\min_{x} \quad J(x) \\ \text{s.t.} \quad & \mathbf{e}[k+1] = xM_{\mathrm{f}}i_{\mathrm{f}}[k](\cos\widetilde{(\theta_{\mathrm{sg}}[\mathbf{k}+\mathbf{1}]}))\\ & \theta_{\mathrm{sg}}[k+1] = \theta_{\mathrm{sg}}[k] + h\omega_{\mathrm{sg}}[k] \\ & T_{\mathrm{e}}[k+2] = M_{\mathrm{f}}i_{\mathrm{f}}[k] < \mathbf{i}[k+2], (\cos\widetilde{(\theta_{\mathrm{sg}}[\mathbf{k}+\mathbf{2}]})) > \\ & T_{\mathrm{m}}[k+2] = \frac{P_{\mathrm{ac,ref}}[k+2]}{\omega_{\mathrm{n}}} \end{aligned} \tag{6}$$

where x and $J(x)$ are given in (5), $P_{\mathrm{ac,ref}}$ is the ac side power dispatch command, and the vectors $\mathbf{i}$, and $\widetilde{\cos(\theta_{\mathrm{sg}})}$ are as defined in [9].

The objective function $J(x)$ is transformed into an unconstrained optimization problem by substituting the equality terms in (6) to $J(x)$. Thereafter, the transformed objective function is minimized using Newton's method described in [22]. The detailed derivation of $J(x)$ used in the optimization is provided in the Appendix. The $\omega_{\mathrm{sg}}[k+1]$ at every time step is calculated by the following recursive formula for $(n+1)^{th}$ iteration given by

$$x^{(n+1)} = x^{(n)} - F\left(x^{(n)}\right)^{-1} g(x^{(n)}) \tag{7}$$

where

$$F\left(x^{(n)}\right) = \left[\frac{\partial g(x^{(n)})}{\partial x}\right]; \; g(x^{(n)}) = \left[\frac{\partial J(x^{(n)})}{\partial x}\right]$$

3.4. ANALYSIS OF UNCONSTRAINED OPTIMIZATION

In this section, the analysis of the Newton's method employed for the unconstrained optimization is given. In general, MBPC-based methods are computationally exhaustive. With the Newton's method used for optimizing (16), the computational burden was reduced and produced an optimal solution. To validate the stated claim, the following proofs are presented: a) proof of minima, and b) proof of convergence.

3.4.1. Proof of Minima.

3.4.1. Proof of Minima. The cost function function $J(x)$ is a well-defined convex function, since $J''(x)$ (or $F(x)$) $> 0 \; \forall \; x \in \mathbb{R}, \lambda_1$ and $\lambda_2 > 0$.

Proof. Based on the cost function defined in (5), The gradient $g(x)$ and Hessian $F(x)$ are derived from $J(x)$ and are given as

$$g(x) = 2\lambda_1 \left(T_\mathrm{e}[k+2] - T_\mathrm{m}[k+2]\right) \frac{\partial T_\mathrm{e}[k+2]}{\partial x} - 2\lambda_2 \left(\omega_\mathrm{n} - x\right) \tag{8}$$

$$F(x) = 2\lambda_1 \left(T_\mathrm{e}[k+2] - T_\mathrm{m}[k+2]\right) \frac{\partial^2 T_\mathrm{e}[k+2]}{\partial x^2} + 2\lambda_1 \left(\frac{\partial T_\mathrm{e}[k+2]}{\partial x}\right)^2 + 2\lambda_2 \tag{9}$$

where $\frac{\partial T_\mathrm{e}[k+2]}{\partial x}$ is given in (10) and $\frac{\partial^2 T_\mathrm{e}[k+2]}{\partial x^2}$ is given in (11).

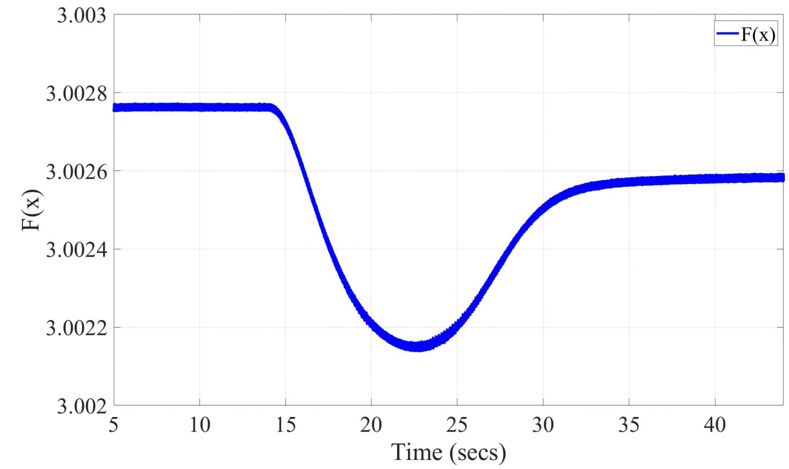

Figure 4. F(x) for the use case of 804.44 MW LOG in WI

$$
\begin{aligned}
\frac{\partial T_{\mathrm{e}}[k+2]}{\partial x} = {} & \left(t_1 (M_{\mathrm{f}} i_{\mathrm{f}}[k])^2 (\cos(\theta_a)^2\right) - h\,(t_2)\, M_{\mathrm{f}} i_{\mathrm{f}}[k] i_{\mathrm{a}}[k+1] \sin(\theta_a) \\
& - 2ht_1 (M_{\mathrm{f}} i_{\mathrm{f}}[k])^2 \cos(\theta_a) \sin(\theta_a) x + ht_1 M_{\mathrm{f}} i_{\mathrm{f}}[k+1] v_{\mathrm{a}}[k+1] \sin(\theta_a) \\
& + (t_1 (M_{\mathrm{f}} i_{\mathrm{f}}[k])^2 (\cos(\theta_b)^2) - h\,(t_2)\, M_{\mathrm{f}} i_{\mathrm{f}}[k] i_{\mathrm{b}}[k+1] \sin(\theta_b) \\
& - 2ht_1 (M_{\mathrm{f}} i_{\mathrm{f}}[k])^2 \cos(\theta_b) \sin(\theta_b) x + ht_1 M_{\mathrm{f}} i_{\mathrm{f}}[k] v_{\mathrm{b}}[k+1] \sin(\theta_b) \\
& + \left(t_1 (M_{\mathrm{f}} i_{\mathrm{f}}[k])^2 (\cos(\theta_c))^2\right) - h\,(t_2)\, M_{\mathrm{f}} i_{\mathrm{f}}[k] i_{\mathrm{c}}[k+1] \sin(\theta_c) \\
& - 2ht_1 (M_{\mathrm{f}} i_{\mathrm{f}}[k])^2 \cos(\theta_c) \sin(\theta_c) x + ht_1 M_{\mathrm{f}} i_{\mathrm{f}}[k] v_{\mathrm{c}}[k+1] \sin(\theta_c) \\
& \text{where } t_1 = \frac{h}{L_{\mathrm{s}} + L_{\mathrm{o}}/2} \text{ and } t_2 = 1 - h\frac{R_{\mathrm{s}} + R_{\mathrm{o}}/2}{L_{\mathrm{s}} + L_{\mathrm{o}}/2}; \\
& \theta_a = \theta_{\mathrm{sg}}[k+1]; \theta_b = \theta_{\mathrm{sg}}[k+1] - 2\pi/3; \theta_c = \theta_{\mathrm{sg}}[k+1] - 4\pi/3
\end{aligned} \tag{10}
$$

$$
\frac{\partial^2 T_{\mathrm{e}}[k+2]}{\partial x^2} = -2ht_1 (M_{\mathrm{f}} i_{\mathrm{f}}[k])^2 \left(\cos(\theta_a)\sin(\theta_a) + \cos(\theta_b)\sin(\theta_b) + \cos(\theta_c)\sin(\theta_c)\right) \tag{11}
$$

From (9), (11), and since λ_1 and $\lambda_2 > 0$, the first term in (9) is always 0 (under balanced grid conditions), the second term in (9) is always greater than or equal to 0, and the third term in (9) is always greater than 0. In summary, it can be deduced from (9), (10), (11), and λ_1 and $\lambda_2 > 0$, that $F(x)$ is always $> 0 \; \forall \, x \in \mathbb{R}$. Thus, J(x) is a well-defined convex function. As $J(x)$ is convex, the optimization problem converges to a global minimum at each iteration [23]. For example, in Figure 4, the $F(x)$ generated in the proposed method when MARS is connected to the Western Interconnection (WI) grid in the US and there is a loss of generation (LOG) of 804.44 MW at t = 14 s is shown. From Figure 4, it can be observed that $F(x)$ is always greater than 0.

3.4.2. Proof of Convergence. The calculation of the optimal x at every time-step by solving the optimization problem of (6) is a computationally challenging task. In the case of the MARS system, the time-step employed is 60 μs in the L-1 controller, which makes it imperative to minimize the iterations needed for convergence of the optimization algorithm. The optimization problem in (6) has good convergence properties and was solved well under

60 μs. In this case, the optimization problem converges to x^* with an order of convergence of atleast 2 in case of unbalanced grid conditions and of atleast 4 in case of balanced grid conditions.

Proof. To prove the order of convergence of the proposed optimization problem, the following were used: a) cost function $J(x) \in C^5$, as may be noted in (16) b) $x^* \in \mathbb{R}$ is a point such that $g(x^*) = 0$, and c) $F(x)$ has an inverse, as $F(x)$ is always greater than 0. Based on the properties stated above and from the $F(x)$ given in (9), $F(x)^{-1}$ exists because from (10), (11), and $\lambda_1, \lambda_2 > 0$, the minimum value of $F(x)$ is $2\lambda_2$ and therefore always satisfies

$$|F(x)^{-1}| \le \frac{1}{2\lambda_2} \qquad \forall\, x \in \mathbb{R} \tag{12}$$

Taylor's series expansion of $g(x)$ about x^n

$$g(x) - g(x^n) - F(x^n)(x - x^n) - \frac{F'(x^n)}{2}(x - x^n)^2 - \frac{F''(x^n)}{6}(x - x^n)^3 \le O(x - x^n)^4 \tag{13}$$

From $J(x) \in C^5$ and $F(x)$ is invertible, there exists constants $\epsilon > 0$, and $c_1 > 0$, $\ni$ if $x^n \in \{x : |x - x^*| \le \epsilon\}$ and substituting $x = x^*$ in (13)

$$|F(x^n)||x^{n+1} - x^* - \frac{F'(x^n)F^{-1}(x^n)}{2}(x^n - x^*)^2 + \frac{F''(x^n)F^{-1}(x^n)}{6}(x^n - x^*)^3| \le c_1|x^n - x^*|^4 \tag{14}$$

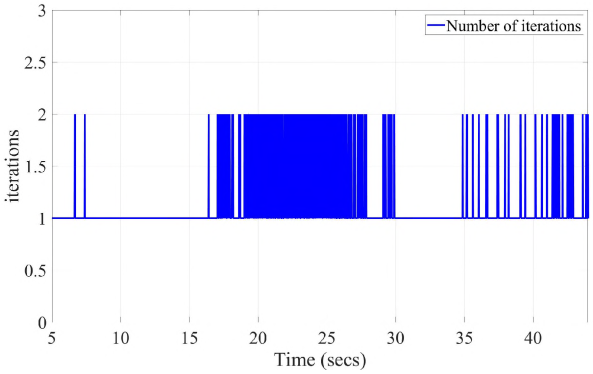

Figure 5. Number of iterations for use case 804.44 MW LOG in WI

$$|x^{n+1}-x^*| \le |\frac{3F'(x^n)F^{-1}(x^n)(x^n-x^*)^2-F''(x^n)F^{-1}(x^n)(x^n-x^*)^3}{6}|+|c_1F^{-1}(x^n)||x^n-x^*|^4 \tag{15}$$

From (15), the order of convergence is atleast 2 in the case of unbalanced grid conditions and atleast 4 in the case of balanced grid conditions since $F'(x)$ and $F''(x)$ are 0. In Figure 5, the number of iterations for each simulation time step are shown for the test case of 804.44 MW generation loss in WI. From Figure 5, it can be observed that the maximum number of iterations taken by optimization method to converge to optimal solution is never more than 2, indicating that very few iterations are needed to converge to the minima.

3.5. IMPLEMENTATION OF THE PROPOSED CONTROL METHOD

The flowchart for the proposed MBPC-based control method is shown in Figure 6. The implementation for the MBPC-based frequency control is briefly explained in this section. i_j and v_j are measured from the point of interconnection of MARS to transmission grid. Once the i_j is measured at $[k]^{\text{th}}$ instant, using dynamic model in (1), the i_j at $[k+1]^{\text{st}}$ instant is estimated. As the variation of v_j is slower compared to the MARS system dynamics, in this implementation the v_j at $[k+1]^{\text{st}}$ instant are assumed to be equal to the v_j at $[k]^{\text{th}}$ instant. θ_{sg} at $[k+1]^{\text{st}}$ is estimated based on (3). e_j at $[k+1]^{\text{st}}$ is calculated using (2b). The estimated values of i_j at $[k+1]^{\text{st}}$, e_j at $[k+1]^{\text{st}}$, and v_j at $[k+1]^{\text{st}}$ are used in predicting i_j at $[k+2]^{\text{th}}$ using (1). Then, T_{e} at $[k+2]^{\text{th}}$ instant is predicted using (2a) by substituting i_j at $[k+2]^{\text{th}}$. The predicted state is included in the cost function $J(x)$ and then it is minimized using unconstrained optimization to obtain the optimal value x. In predicting T_{e} at $[k+2]^{\text{th}}$ instant, the initial guess for ω_{sg} at $[k+1]^{\text{st}}$ instant is ω_{sg} at $[k]^{\text{th}}$ instant. Based on the optimal value x, e_j is updated and qd frame reference currents ($i_{\text{qd,ref}}$). The $i_{\text{qd,ref}}$ are used in the decoupled current controller to determine the phase modulation index (m_j) and then m_j is used to generate arm modulation indices (m_j^y) that are sent to L-2 controller in the MARS system [6].

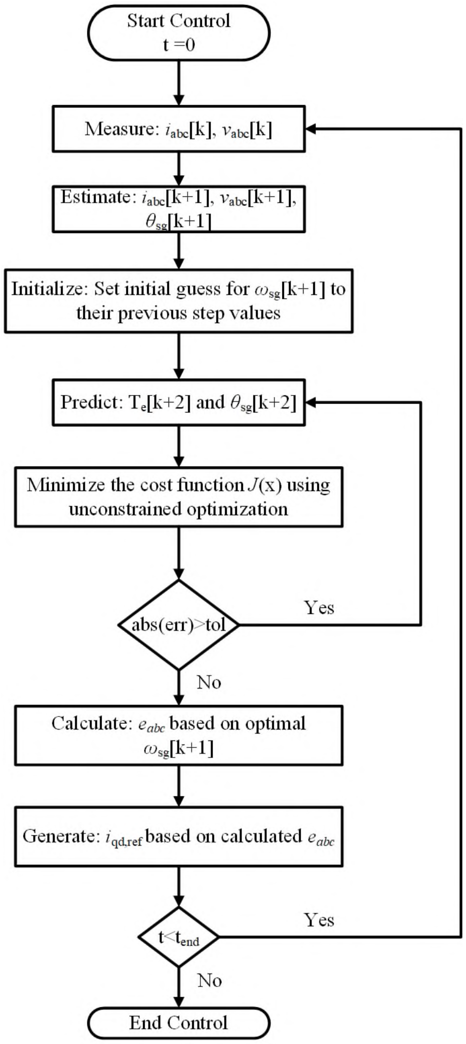

Figure 6. Implementation of MBPC-based frequency control

4. PSCAD OFFLINE SIMULATION RESULTS

4.1. TEST SYSTEMS

To evaluate the performance of the proposed controller, an offline simulation model of the MARS system connecting to WI ac grid is developed. The frequency dynamics of the WI ac grid are modeled based on WSEIG1 to accurately represent the dynamics of frequency reported in [24]. The MARS system is configured as an upgrade to the HVdc substation in Pittsburg, California, of the TransBay Cable project [25]. Assuming 150 kW, 1 kV PV and ESS SMs, the number of SMs per arm are 111 PV, 37 ESS and 81 normal SMs. The size of the PV and ESS SMs are determined based on utilizing 200 A, 3.3 kV SiC devices in the dc-dc converters. The total number of SMs per arm are determined by the dc-link voltage in the installed HVdc substation (in the TransBay Cable project). The proposed controller in the MARS system is tested under various SCR and inertia conditions which reflect the high penetration of PV scenarios and remote connections of the MARS system. Several different SCR conditions are emulated based on the variation of the transmission line lengths in the ac grid model. Inertia is varied by changing the parameters in the model representing the frequency dynamics of the WI ac grid.

4.2. USE CASES

Two use cases are used to evaluate the proposed controller for the operating condition of $P_{\mathrm{ac,ref}} = P_{\mathrm{dc,ref}} = 100$ MW and varied SCR and inertia conditions: (a) 804.44 MW loss of generation at t = 14.0 s based on Haynes3 generator in WI grid and (b) a balanced three phase fault at t = 4 s with a duration of 0.2 s.

4.2.1. Use Case 1: 804.44 Loss of Generation.

An event of 804.44 MW LOG at t = 14 s in the WI is simulated. The frequency response measured at Pittsburg for SCR case = 0.5 and inertia = 11 without support, with MBPC-based support (*grid forming* mode of

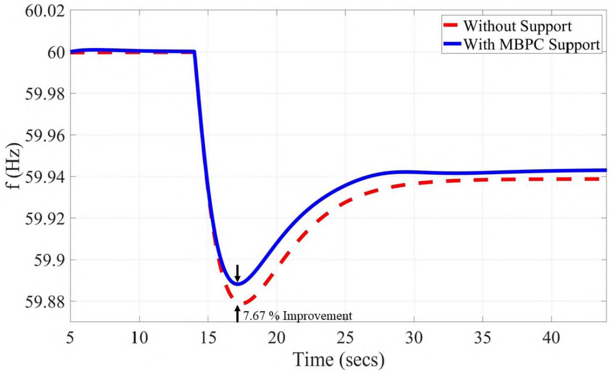

Figure 7. Grid Frequency response for LOG in WI for SCR = 0.5 and inertia =11

control) and with the VSG support (*grid following* mode of control) from the MARS system [5] are shown in Figure 7. The frequency improvements in nadir and steady state for each SCR condition and inertia = 23 and for each type of controller are tabulated in Table 1. The MBPC-based frequency control is enabled throughout the simulation. From Figure 7, it can be observed that system is in a stable mode of operation. In this case, both ac and dc power dispatch requirements are satisfactorily delivered with PV power being supplied to the ESS. Once the LOG is detected, the additional power requirements are met from available PV and ESS reserves. From Figure 7, it can be observed that the frequency improvement in the case of with and without MBPC-based control is 7.67%. In the case of SCR = 0.5 with VSG support, the MARS system operates in an unstable mode of operation due to the presence of instabilities in the controller. These instabilities arise from the inaccurate tracking of the voltage angle from the PLL. From Table 1, it is observed that for higher SCR conditions such as SCR = 10, the MARS with VSG support offers better frequency support in terms of frequency nadir and steady state in comparison to the MARS system with MBPC-based support. In the lower SCR conditions 0.5, and 2, from the Table 1, it is observed that the MARS system with MBPC-based support offers better frequency support in terms of frequency nadir and steady state indicating the MARS system with *grid forming* functionality offers enhanced support in comparison to the MARS system with *grid following* functionality during grid disturbances in the high penetration of PV scenarios and remote connection of the MARS system.

Table 1. Improvement in frequency response for different SCRs

SCR	Improvements			
	MBPC		VSG	
	nadir	steady state	nadir	steady state
0.5	8.29 %	6.04 %	UNSTABLE	
2	13.96 %	9.10 %	10.32 %	5.9 %
4	14.19 %	9.19 %	10.86 %	5.99 %
10	14.53 %	9.73 %	16.87 %	17.34 %

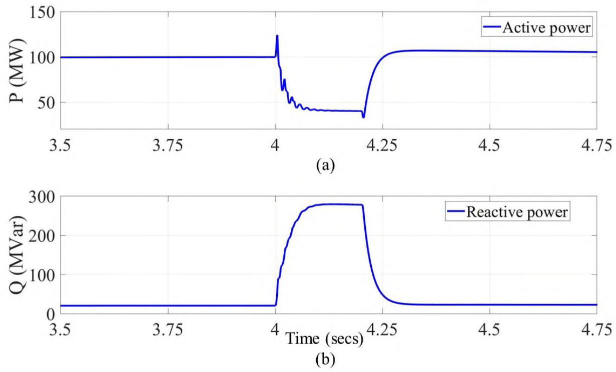

Figure 8. (a) active power- and (b) reactive power during a three phase fault for SCR = 0.5 and inertia = 11

4.2.2. Use Case 2: Balanced Three-Phase Fault. A three-phase fault is simulated on the transmission line between the grid and the MARS model at t = 4 s with a fault duration of 0.2 s. The simulation result for the proposed *grid forming* control-based voltage support for SCR = 0.5 and inertia = 11 case is shown in Figure 8. In this figure, the active and reactive power provided by the MARS system during a three-phase fault is shown. From Figure 8, it can be observed that the MARS system provides continuity of operation successfully during the fault and operates in a stable mode of operation during post-fault conditions. The MARS system with a *grid following* mode of control does not provide stable support for the same balanced fault condition. In this case, the internal states of the system oscillate and lead to instabilities. The improvement in the voltage response with SG-based support (*grid forming* mode of control) and VSG support for varied SCR and inertia = 23 is tabulated in Table 2.

Table 2. Improvement in voltage response for various SCR

Improvements				
SCR	0.5	2	4	10
SG	STABLE	27.17 %	15.07 %	16.17 %
VSG	UNSTABLE	23.06 %	14.71 %	14.45 %

5. REAL-TIME SIMULATION RESULTS

The proposed controller is tested through real-time simulation of a case-study of the MARS system connecting to WI ac grid. The real-time simulation is performed in Opal-RT OP5707 simulator. This evaluation provides an understanding of the resources utilized to perform proposed predictive grid-forming control. The model is shown in Figure 9. The pi-line section is tuned after disconnecting the reduced-order model and based on the contingency results of line-to-line fault at Gates near Pittsburg. The frequency dynamics are represented by a similar model as used in the PSCAD offline simulation. The simulation time-step for the system is 60 μs. The control system (L1) in the MARS system and the real-time simulation model of the MARS system connecting to WI ac grid are implemented in the central processing unit (CPU) of the OP5707. The functionalities described in L1 controller and real-time simulation system are implemented in two different CPU cores of OP5707. This implementation enables the identification of resource requirements to implement the proposed predictive *grid-forming* L1 controller in the MARS system and also emulates the delays associated with communication between the L1 controller and the MARS system hardware. The results for frequency response with and without MBPC support for SCR = 4 and inertia = 23 are shown in Figure 10. The improvement observed in

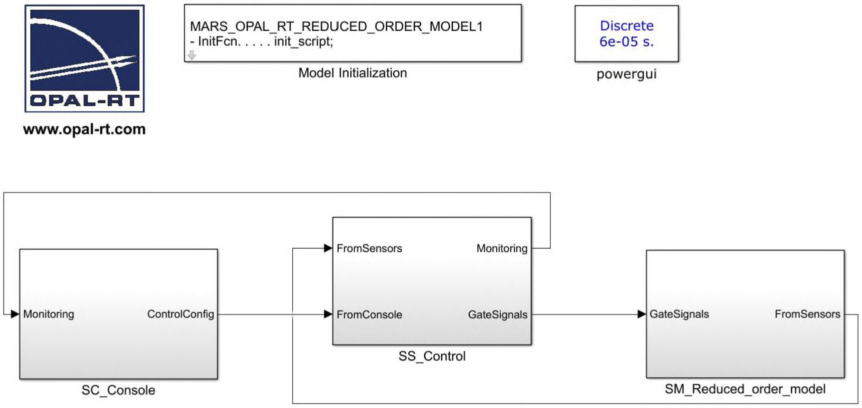

Figure 9. OPAL-RT model

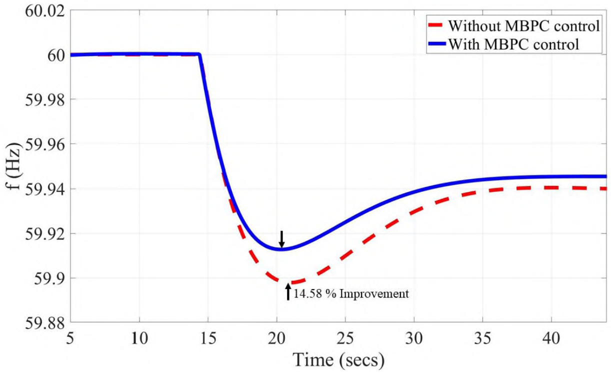

Figure 10. Grid Frequency response for LOG in WI for SCR = 4 and inertia = 23

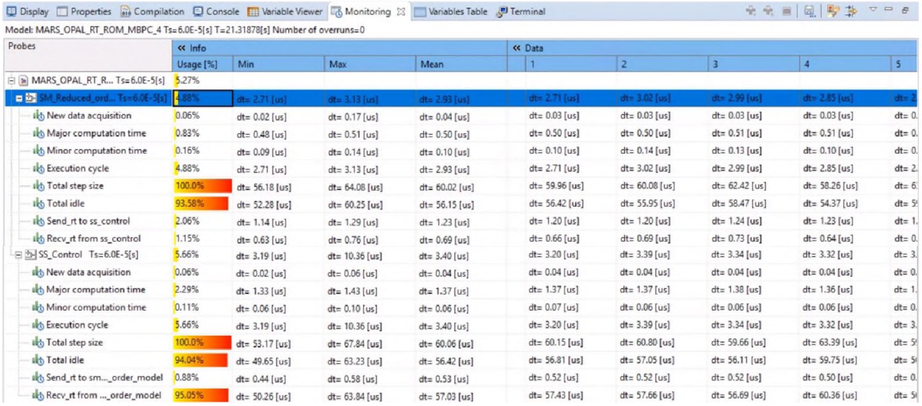

Model: MARS_OPAL_RT_ROM_MBPC_4 Ts=6.0E-5[s] T=21.31878[s] Number of overruns=0

Probes	« Info				« Data				
	Usage [%]	Min	Max	Mean	1	2	3	4	5
MARS_OPAL_RT_R... Ts=6.0E-5[s]	5.27%								
SM_Reduced_ord... Ts=6.0E-5[s]	4.88%	dt= 2.71 [us]	dt= 3.13 [us]	dt= 2.93 [us]	dt= 2.71 [us]	dt= 3.02 [us]	dt= 2.99 [us]	dt= 2.85 [us]	dt= 2.
New data acquisition	0.06%	dt= 0.02 [us]	dt= 0.17 [us]	dt= 0.04 [us]	dt= 0.03 [us]	dt= 0.03 [us]	dt= 0.03 [us]	dt= 0.03 [us]	dt= 0.
Major computation time	0.83%	dt= 0.48 [us]	dt= 0.51 [us]	dt= 0.50 [us]	dt= 0.50 [us]	dt= 0.50 [us]	dt= 0.51 [us]	dt= 0.51 [us]	dt= 0.
Minor computation time	0.16%	dt= 0.09 [us]	dt= 0.14 [us]	dt= 0.10 [us]	dt= 0.10 [us]	dt= 0.14 [us]	dt= 0.13 [us]	dt= 0.10 [us]	dt= 0.
Execution cycle	4.88%	dt= 2.71 [us]	dt= 3.13 [us]	dt= 2.93 [us]	dt= 2.71 [us]	dt= 3.02 [us]	dt= 2.99 [us]	dt= 2.85 [us]	dt= 2.
Total step size	100.0%	dt= 56.18 [us]	dt= 64.08 [us]	dt= 60.02 [us]	dt= 59.96 [us]	dt= 60.08 [us]	dt= 62.42 [us]	dt= 58.26 [us]	dt= 6
Total idle	93.58%	dt= 52.28 [us]	dt= 60.25 [us]	dt= 56.15 [us]	dt= 56.42 [us]	dt= 55.95 [us]	dt= 58.47 [us]	dt= 54.37 [us]	dt= 5
Send_rt to ss_control	2.06%	dt= 1.14 [us]	dt= 1.29 [us]	dt= 1.23 [us]	dt= 1.20 [us]	dt= 1.20 [us]	dt= 1.24 [us]	dt= 1.23 [us]	dt= 1.
Recv_rt from ss_control	1.15%	dt= 0.63 [us]	dt= 0.76 [us]	dt= 0.69 [us]	dt= 0.66 [us]	dt= 0.69 [us]	dt= 0.73 [us]	dt= 0.64 [us]	dt= 0.
SS_Control Ts=6.0E-5[s]	5.66%	dt= 3.19 [us]	dt= 10.36 [us]	dt= 3.40 [us]	dt= 3.20 [us]	dt= 3.39 [us]	dt= 3.34 [us]	dt= 3.32 [us]	dt= 3.
New data acquisition	0.06%	dt= 0.02 [us]	dt= 0.06 [us]	dt= 0.04 [us]	dt= 0.04 [us]	dt= 0.04 [us]	dt= 0.04 [us]	dt= 0.04 [us]	dt= 0.
Major computation time	2.29%	dt= 1.33 [us]	dt= 1.43 [us]	dt= 1.37 [us]	dt= 1.37 [us]	dt= 1.37 [us]	dt= 1.38 [us]	dt= 1.36 [us]	dt= 1.
Minor computation time	0.11%	dt= 0.06 [us]	dt= 0.10 [us]	dt= 0.06 [us]	dt= 0.07 [us]	dt= 0.06 [us]	dt= 0.06 [us]	dt= 0.06 [us]	dt= 0.
Execution cycle	5.66%	dt= 3.19 [us]	dt= 10.36 [us]	dt= 3.40 [us]	dt= 3.20 [us]	dt= 3.39 [us]	dt= 3.34 [us]	dt= 3.32 [us]	dt= 3.
Total step size	100.0%	dt= 53.17 [us]	dt= 67.84 [us]	dt= 60.06 [us]	dt= 60.15 [us]	dt= 60.80 [us]	dt= 59.66 [us]	dt= 63.39 [us]	dt= 5
Total idle	94.04%	dt= 49.65 [us]	dt= 63.23 [us]	dt= 56.42 [us]	dt= 56.81 [us]	dt= 57.05 [us]	dt= 56.11 [us]	dt= 59.75 [us]	dt= 5
Send_rt to sm..._order_model	0.88%	dt= 0.44 [us]	dt= 0.58 [us]	dt= 0.53 [us]	dt= 0.52 [us]	dt= 0.52 [us]	dt= 0.52 [us]	dt= 0.50 [us]	dt= 0.
Recv_rt from ..._order_model	95.05%	dt= 50.26 [us]	dt= 63.84 [us]	dt= 57.03 [us]	dt= 57.43 [us]	dt= 57.66 [us]	dt= 56.69 [us]	dt= 60.36 [us]	dt= 5

Figure 11. Snapshot of resource utilization during LOG in WI for SCR = 4 and inertia = 23

frequency nadir and steady state with MBPC-based support in the MARS system in real-time implementation from Figure 10 is 14.58 % and 9.37 % in comparison to without support in the MARS system. The results obtained from real-time implementation are similar to the results obtained from offline simulations. The snapshot of the resources used by entire model during simulation is shown in Figure 11. From Figure 11, it is observed that the proposed *grid forming* control uses less computational resources and is not computationally burdensome. The resource utilization of the L1 controller with the proposed *grid forming* control is 5.66 %, which is very small and validates the fast convergence theoretically proven earlier.

6. CONCLUSION

In this paper, a MBPC-based *grid forming* control for the MARS system to provide inertial and primary frequency response is proposed for varied SCR and varied inertia conditions. In addition to MBPC-based *grid forming* frequency support, a traditional synchronverter control based voltage support is also provided. The proposed control algorithm and the MARS system control architecture is evaluated and validated for the MARS system at Pittsburg, CA on the PSCAD/EMTDC simulation environment for comprehensive offline simulations and on OPAL-RT simulators for online real-time simulations. The proposed control algorithm were tested for different grid scenarios based on variations in SCR and inertia. For the study system considered in this paper, the MARS system with *grid forming* control provides better frequency support in terms of higher frequency nadir and higher frequency steady state during frequency excursions in comparison to VSG-based control method under low SCR operating conditions. The combination of the predictive frequency support with SG-based voltage support has been shown to be stable during fault studies that have been performed. The key takeaway point identified from this research endeavor is that for the study system considered in this paper, the MBPC-based control method is more stable and gives better performance in terms of frequency nadir and steady state improve-

$$
\begin{aligned}
J(x) = {} & \lambda_1(M_\mathrm{f} i_\mathrm{f}[k+1]((t_2)\, i_\mathrm{a}[k+1]\cos(\theta_a) + t_1 x(M_\mathrm{f} i_\mathrm{f}[k])(\cos(\theta_a))^2 - t_1 v_\mathrm{a}[k+1] \\
& \cos(\theta_a) - h\,(t_2)\, i_\mathrm{a}[k+1]\sin(\theta_a)x - h t_1 x^2(M_\mathrm{f} i_\mathrm{f}[k])\cos(\theta_a)\sin(\theta_a) + h t_1 \\
& v_\mathrm{a}[k+1]\sin(\theta_a)x + (t_2)\, i_\mathrm{b}[k+1]\cos(\theta_b) + t_1 x(M_\mathrm{f} i_\mathrm{f}[k])(\cos(\theta_b))^2 - t_1 v_\mathrm{b}[k+1] \\
& \cos(\theta_b) - h\,(t_2)\, i_\mathrm{b}[k+1]\sin(\theta_b)x - h t_1 x^2(M_\mathrm{f} i_\mathrm{f}[k])\cos(\theta_b)\sin(\theta_b) + h t_1 \\
& v_\mathrm{b}[k+1]\sin(\theta_b)x + (t_2)\, i_\mathrm{c}[k+1]\cos(\theta_c) + t_1 x(M_\mathrm{f} i_\mathrm{f}[k])(\cos(\theta_c))^2 - t_1 v_\mathrm{c}[k+1] \\
& \cos(\theta_c) - h\,(t_2)\, i_\mathrm{c}[k+1]\sin(\theta_c)x - h t_1 x^2(M_\mathrm{f} i_\mathrm{f}[k])\cos(\theta_c)\sin(\theta_c) + h t_1 \\
& v_\mathrm{c}[k+1]\sin(\theta_c)x) - T_\mathrm{m}[k+2])^2 + \lambda_2\,(\omega_\mathrm{n} - x)^2
\end{aligned}
\tag{16}
$$

ment for scenarios with high penetration of PE-based resources. Furthermore, theoretical proofs for superior performance of the proposed control method are provided along with validation of real-time performance of the proposed control method.

APPENDIX

In this section, a detailed derivation for $J(x)$ used in the analysis of unconstrained optimization section is presented. By substituting T_e from (2a) into (5), $J(x)$ can be written as given in (17).

$$\begin{aligned} J(x) = \lambda_1 (M_\mathrm{f} i_\mathrm{f}[k] (i_\mathrm{a}[k+2]\cos(\theta_\mathrm{sg}[k+2]) \\ + i_\mathrm{b}[k+2]\cos(\theta_\mathrm{sg}[k+2] - 2\pi/3) \\ + i_\mathrm{c}[k+2]\cos(\theta_\mathrm{sg}[k+2] - 4\pi/3)) - T_\mathrm{m}[k+2])^2 \\ + \lambda_2 (\omega_\mathrm{n} - x)^2 \end{aligned} \tag{17}$$

To obtain the final $J(x)$, the following steps are followed: a) θ_sg at the $[k+2]^\mathrm{th}$ instant based on (3) and i_j at the $[k+2]^\mathrm{th}$ instant based on (1) are substituted into (17), b) e_j at $[k+1]^\mathrm{st}$ based on (2b) is substituted into (1) while calculating for i_j at the $[k+2]^\mathrm{th}$ instant, and c) once the above steps are completed, a small signal approximation is applied: i.e. the cosine and sine terms in which the angles (hx) are very small $(hx << 1)$ are substituted with 1 and hx respectively. The final form of $J(x)$ after completing all these steps is given in (16).

ACKNOWLEDGEMENT

This paper is based upon work supported by the U.S. Department of Energy's Office of Energy Efficiency and Renewable Energy (EERE) under Solar Energy Technologies Office (SETO) Agreement Number 34019. Authors would like to thank Dr. John Seuss for overseeing the project developments and providing guidance. The views expressed herein do not necessarily represent the views of the U.S. Department of Energy or the United States Government.

REFERENCES

[1] "New solar opportunities for a new decade." [Online]. Available: https://www.energy.gov/eere/solar/sunshot-2030.

[2] M. Lewis, "Energy Storage Procurement Tracker," 2020. [Online]. Available: https://www.morganlewis.com/-/media/files/document/2020/energy_storage_tracker_2020.pdf

[3] Y. Li and J. D. McCalley, "Design of a high capacity inter-regional transmission overlay for the U.S." *IEEE Transactions on Power Systems*, vol. 30, no. 1, pp. 513–521, 2015.

[4] S. Debnath, M. Chinthavali, J. Sun, P. Marthi, S. Chinthavali, M. Lee, M. Elizondo, Y. Makarov, Q. Huang, M. Vallem, Y. Liu, A. Tbaileh, Q. Zhang, N. Samaan, H. Kirkham, J. Novacheck, and J. Lau, "Models and Methods for Assessing the Value of HVdc and MVdc Technologies in Modern Power Grids," 2020. [Online]. Available: https://info.ornl.gov/sites/publications/Files/Pub124776.pdf

[5] S. Debnath, P. Marthi, Q. Xia, J. Pan, M. Saeedifard, V. N. Vipin, S. Chakraborty, and M. Arifujjaman, "Renewable integration in hybrid ac-dc systems using multi-port autonomous reconfigurable solar power plant (MARS)," *IEEE Transactions on Power Systems*, pp. 1–1, 2020.

[6] P. R. V. Marthi, S. Debnath, and M. L. Crow, "Synchronverter-based control of multi-port autonomous reconfigurable solar plants (MARS)," in *Proc. ECCE2020 - Twelfth Annual IEEE Energy Conversion Congress and Exposition.*

[7] North American Electric Reliability Corporation, "Integrating Inverter-Based Resources into Low Short Circuit Strength Systems," 2018. [Online]. Available: https://www.nerc.com/comm/PC_Reliability_Guidelines_DL/Item_4a._Integrating%20_Inverter-Based_Resources_into_Low_Short_Circuit_Strength_Systems_-_2017-11-08-FINAL.pdf

[8] L. Yashen, J. H. Eto, B. B. Johnson, J. D. Flicker, R. H. Lasseter, H. N. V. Pico, G.-S. Seo, B. J. Pierre, and A. Ellis, "Research Roadmap on Grid-Forming Inverters," 2020. [Online]. Available: https://www.nrel.gov/docs/fy21osti/73476.pdf.

[9] Q. Zhong and G. Weiss, "Synchronverters: Inverters that mimic synchronous generators," *IEEE Transactions on Industrial Electronics*, vol. 58, no. 4, pp. 1259–1267, April 2011.

[10] M. Amin, A. Rygg, and M. Molinas, "Self-synchronization of wind farm in an MMC-based HVdc system: A stability investigation," *IEEE Transactions on Energy Conversion*, vol. 32, no. 2, pp. 458–470, 2017.

[11] U. Tamrakar, D. Shrestha, M. Maharjan, B. P. Bhattarai, T. M. Hansen, and R. Tonkoski, "Virtual inertia: Current trends and future directions," *Applied Sciences*, vol. 7, no. 7, p. 654, 2017.

[12] J. Rocabert, A. Luna, F. Blaabjerg, and P. Rodríguez, "Control of power converters in ac microgrids," *IEEE Transactions on Power Electronics*, vol. 27, no. 11, pp. 4734–4749, 2012.

[13] B. B. Johnson, S. V. Dhople, A. O. Hamadeh, and P. T. Krein, "Synchronization of parallel single-phase inverters with virtual oscillator control," *IEEE Transactions on Power Electronics*, vol. 29, no. 11, pp. 6124–6138, 2014.

[14] S. Du, A. Dekka, Bin.Wu, and N. Zargari, *Modular Multilevel Converters: Analysis, Control, and Applications*. Wiley-IEEE Press, 2018.

[15] N. Sockeel, J. Gafford, B. Papari, and M. Mazzola, "Virtual inertia emulator-based model predictive control for grid frequency regulation considering high penetration of inverter-based energy storage system," *IEEE Transactions on Sustainable Energy*, vol. 11, no. 4, pp. 2932–2939, 2020.

[16] C. Zheng, T. Dragicevic, and F. Blaabjerg, "Model predictive control based virtual inertia emulator for an islanded ac microgrid," *IEEE Transactions on Industrial Electronics*, pp. 1–1, 2020.

[17] L. Papangelis, M. Debry, T. Van Cutsem, and P. Panciatici, "Local control of ac/dc converters for frequency support between asynchronous ac areas," in *Proc. 2017 IEEE Manchester PowerTech*, pp. 1–6.

[18] O. Stanojev, U. Markovic, P. Aristidou, G. Hug, D. Callaway, and E. Vrettos, "MPC-based fast frequency control of voltage source converters in low-inertia power systems," *IEEE Transactions on Power Systems*, pp. 1–1, 2020.

[19] O. Stanojev, U. Markovic, E. Vrettos, P. Aristidou, D. Callaway, and G. Hug, "Enhanced MPC for fast frequency control in inverter-dominated power systems," in *Proc. 2020 International Conference on Smart Energy Systems and Technologies (SEST)*, pp. 1–6.

[20] P. R. V. Marthi, S. Debnath, Q. Xia, and M. Saeedifard, "Advanced models and fast simulation algorithms for mars plants," in *Proc. 2020 IEEE/PES Transmission and Distribution Conference and Exposition (T & D)*, Chicago, Illinois, USA, pp. 1–5.

[21] S. Debnath and M. Chinthavali, "Numerical-stiffness-based simulation of mixed transmission systems," *IEEE Transactions on Industrial Electronics*, vol. 65, no. 12, pp. 9215–9224, Dec 2018.

[22] E. K. P. Chong and S. H. Zak, *An Introduction to Optimization*. Wiley, 2004.

[23] S. Boyd and L. Vandenberghe, *Convex Optimization.* Cambridge University Press, 2004.

[24] S. Debnath and J. Sun, “Fidelity requirements with fast transients from VSC-HVdc,” in *Proc. IECON 2018 - 44th Annual Conference of the IEEE Industrial Electronics Society*, pp. 6007–6014.

[25] H. Knaak, “Modular multilevel converters and HVdc/FACTS: A success story,” in *Proc. 2011 14th European Conference on Power Electronics and Applications*, pp. 1–6.

IV. SUITE OF SOLUTIONS FOR REDUCING MOMENTARY CESSATION IN PV/HYBRID PV PLANTS IN LOW SCR AND LOW INERTIA GRIDS

ABSTRACT

With the increased penetration of power electronic (PE) based loads and sources, advanced solutions may be required for the enhancement of grid stability in regions with low short circuit ratio (SCR) and low inertia grids. The requirement of advanced solutions arises from the gradual paradigm shift of the electric grid from the traditional electric machine dominant system to a high penetration of PE-based system. One of the major challenges with such systems in recent times is the momentary cessation during ac grid transmission faults. During momentary cessation, PE-based resources cease to operate, thus creating probable reliability challenges for the grid. In this paper, potential feasible options to provide continuity of operation during such scenarios are presented. The options are considered through identifying upgrades in existing photovoltaic (PV) plants (discrete PV plants) and upgrades in existing and upcoming discrete development of PV and energy storage systems (ESS). The latter is termed as discrete hybrid PV plants. Additionally, an advanced concept of integrated development of PV and ESS connecting to ac transmission grid and high-voltage direct current (HVdc) links called multi-port autonomous reconfigurable solar power plant (MARS). A technical comparison is performed between different types of solutions (discrete PV, discrete hybrid PV, and MARS) for operating PV plants in low SCR and low inertia grids. The developed new solutions are evaluated in the PSCAD/EMTDC simulation environment under different grid event scenarios.

Keywords: Discrete development, PV, ESS, synchronous condenser, low SCR, multi-port, MARS

1. INTRODUCTION

There has been a significant drop in the levelized cost of electricity (LCOE) of utility-scale photovoltaic (PV) power plants in the United States in the past decade. These economic benefits have led to increased interest in PV power plants. In addition to the increased interest in PV power plants, utilities are mandating increased energy storage system (ESS) installations [1]. As the penetration of PV and hybrid PV-ESS plants increase in the grid, there will be plants that connect to low short-circuit ratio (SCR) and low inertia grids.

During transmission line faults, several utility-scale state-of-the-art PV plants and hybrid PV plants momentarily cease to operate [2] [3]. This phenomenon may be detrimental to the stability of the system. Although employing momentary cessation is acceptable for power electronic (PE) based inverters connected in distribution systems, it may cause instability in the bulk transmission system [4]. The Blue Cut fire disturbance and the Canyon fire disturbance occurred on August 16, 2016 and October 9, 2017 are example incidents where momentary cessation utilized in PE-based resources played an important role in the widespread loss of solar PV generation [5] [6]. Similar behavior was also observed in incidents recorded in 2018 and 2020 [7] [8]. Based on these events, recommendations for integration of future PE-based resources include: a) the use of momentary cessation should be as infrequent as possible; b) the maximum amount of active power (P_{poc}) and reactive power (Q_{poc}) that PE-based resources can provide during a transmission line fault should be utilized; c) PE-based resources should not trip within the "no trip zone" defined in the PRC-024-2 standard [9]; and d) studies are needed that employ detailed electromagnetic transient models [10].

Very few studies have been performed on momentary cessation and its effects on transmission system stability in low SCR and inertia grids [11][12][4][13]. In [11][12], the effects of momentary cessation on power system transient stability are studied and a critical operating point of momentary cessation is proposed such that the power system is stable. The proposed method is tested using PSS/e on a system where the PE-based resources provide the majority of power. In [4], an inverter model including momentary cessation during balanced three-phase faults is developed in PSS/e. In [13], suggestions to minimize momentary cessation based on acquired field experiences of PV plants, Type III and Type IV wind generator responses under transmission line system faults are presented. Rather than providing solutions for continuity of operation during normal and abnormal grid conditions, these studies assume momentary cessation of inverter-based resources during grid voltage disturbances. On the contrary, solutions to provide continuity of operation (without momentary cessation) during different transmission line faults in state-of-the-art discrete PV and hybrid discrete PV plants connected to low SCR and low inertia grids are proposed in this research work. These types of plants will need additional upgrades to ensure continuity of operation under faults [14][15]. Additional upgrades may include combination of synchronous condensers, shunt capacitor banks, and dampers in PV plants and hybrid PV plants. Alternatively, PV and ESS that can connect to high-voltage direct current (HVdc) and/or high-voltage alternating current transmission grids may also be considered [16]. This scenario leads to the discrete development of PV inverters, ESS inverters, associated upgrades, and several transformers in future grids with a high penetration of renewables.

One of the major challenges with discrete PV plants and discrete hybrid PV plants is ensuring transient stability. Transient instability may arise from grid disturbances such as transmission line faults and from control interactions [5][6][7]. In addition to the aforementioned discrete PV plants and discrete hybrid PV plants, new solutions such as the integrated development of PV and ESS connecting to high-voltage ac transmission grid and HVdc links through multi-port autonomous reconfigurable solar power plants (MARS) may also be considered [17].The MARS system solution, which has been shown to provide continuity of operations under transmission line faults [17] [18], is also evaluated in this paper. With the MARS system, problems such as increased cost, lower reliability, and reduced efficiency associated with discrete development of PV inverters, ESS inverters, HVdc converter, and several transformers in future grids can be reduced. The MARS-type solution may be leveraged in the presence of HVdc links [16] and/or for direct connection to high-voltage transmission ac grids.

In summary, in this research work: a) options to provide continuity of operation during balanced and unbalanced transmission line faults for state-of-art PV plants and hybrid PV plants in low SCR and low inertia grids are presented; b) detailed EMT models are developed for discrete PV plants, discrete hybrid PV plants, and MARS in the PSCAD/EMTDC simulation environment; and c) technical comparison is presented between the MARS system and hybrid PV plants for different potential upgrade options.

2. OPTIONS TO REDUCE MOMENTARY CESSATION

State-of-the-art utility-scale PV plants are large generation systems that are connected to the high-voltage ac transmission grid. These large PV plants have multiple medium-voltage radial feeders. They include many components such as PV arrays, cooling systems, and transmission substation apparatus (power transformers and circuit breakers). A typical PV power plant schematic is shown below in Figure 1. These PV plants do not

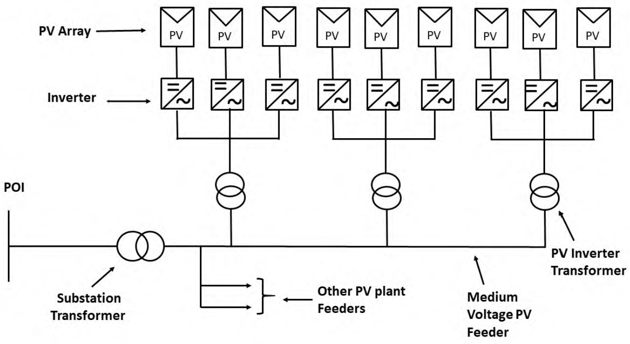

Figure 1. Typical PV power plant

have any rotating parts to contribute to inertial or primary frequency response support. As the penetration of PE-based generation and loads such as these plants increase in the grid, the following stability concerns have been identified:

1. Post-contingency instabilities, especially during high renewable and low load conditions, may be observed [16].
2. Momentary cessations and/or trips or shutdown in PV plants during faults may lead to frequency deviations [5][6][7].
3. Fast changes in inertia and reduced primary frequency response may be observed during loss of generations.

There are three possible options to provide improved stability with the increased penetration of PE-based generations. They are: (a) discrete development of PV plants with upgrades, (b) discrete development of PV and ESS plants with upgrades, and (c) a MARS system that connects directly to the HVdc and high-voltage transmission ac grid.

2.1. UPGRADES IN DISCRETE DEVELOPMENT OF PV PLANTS

The upgrades included in state-of-the-art PV plants for continuity of operation during grid disturbances are synchronous condensers, shunt capacitors, and dampers re-sized to ensure stable operation of plant with lower harmonics. An overview of state-of-the-art PV plants with upgrades is illustrated in Figure 2.

2.1.1. Models for Large Scale PV Plant.

The PV plants are modeled as an aggregation of multiple inverters, distribution lines, and transformers into one inverter and transformer in PSCAD. The aggregated model consists of a PV array, a boost converter, and an inverter that includes filters, transformers, and scaling components. The PV array generates power as a function of temperature and irradiation. The boost converter controls the dc voltage of the inverter to transfer the required power from the PV. Additionally, there

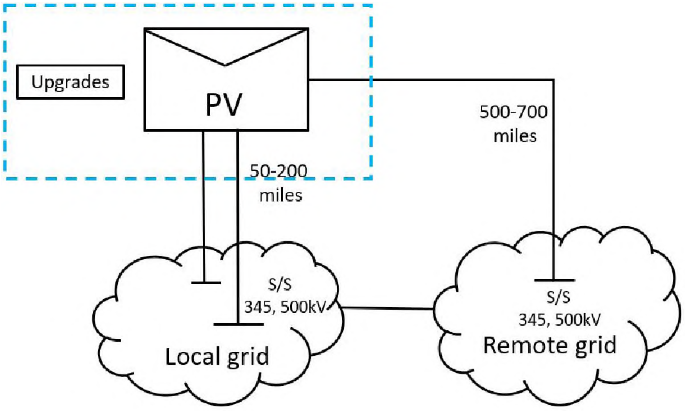

Figure 2. State-of-the-art PV plants with upgrades

are inverter and power plant controllers. The inverter controller controls the active power and reactive power dispatches. It may also control the voltage and frequency locally. The power plant controller identifies ride-through requirements and introduces voltage support at the terminals of the PV plant. A scaling component is used to model several units of inverters and distribution lines/transformers in the PV plants [19].

2.2. UPGRADES IN DISCRETE DEVELOPMENT OF PV AND ESS PLANTS

The upgrades included in the state-of-the-art hybrid PV plant include synchronous condensers, shunt capacitors, and dampers re-sized to ensure stable operation of plant with lower harmonics. They are shown and highlighted in Figure 3.

2.2.1. Models for Large Scale Hybrid PV Plants. The PV plants in hybrid PV plants are modeled in a similar way as described in Section 2.1.1. The ESS plants are also modeled based on an aggregated model that represents multiple inverters as a single inverter. The model consists of a battery and an inverter that includes filters, transformers, and scaling components. The scaling component is similar to that used in the PV plant in [19].

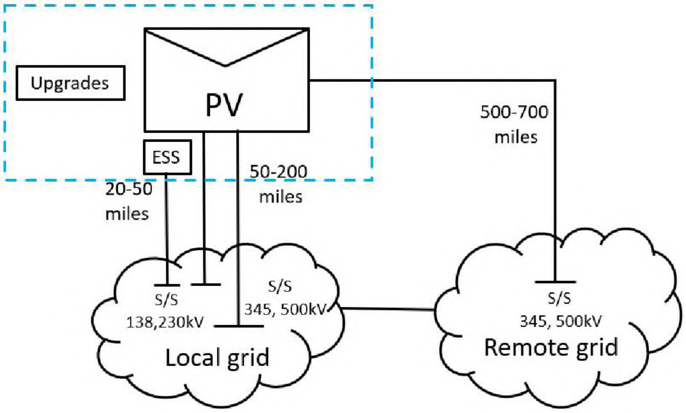

Figure 3. State-of-the-art hybrid PV plants with upgrades

2.3. MARS

2.3.1. MARS System Architecture. The architecture of the MARS system is shown in Figure 4. The MARS system is a three-phase system with six arms in total. Each arm consists of normal sub modules (SMs), PV, and ESS-SMs. The PV systems in each PV-SM are connected to the SM through either isolated or non-isolated dc-dc converters. The ESS systems in each ESS-SM are connected through a bidirectional dc-dc converter. The detailed modeling of the MARS system is described in [17] [18] [20].

2.3.2. MARS Control System. The control architecture in the MARS system is hierarchical in nature. It consists of the following functionalities: (a) voltage and frequency support to the ac grid, active and reactive power control, dc voltage link control, current control (ac current control, dc current control, and circulating current control), and energy balancing control in the L1 controller; (b) capacitor voltage balancing control in the L2 controller; and (c) PV and ESS SMs power control in the L3 controller [17] [18]. The voltage and frequency support to the ac grid can be designed using either *grid forming* control methods such as synchronverter based control [18] or *grid following* control methods

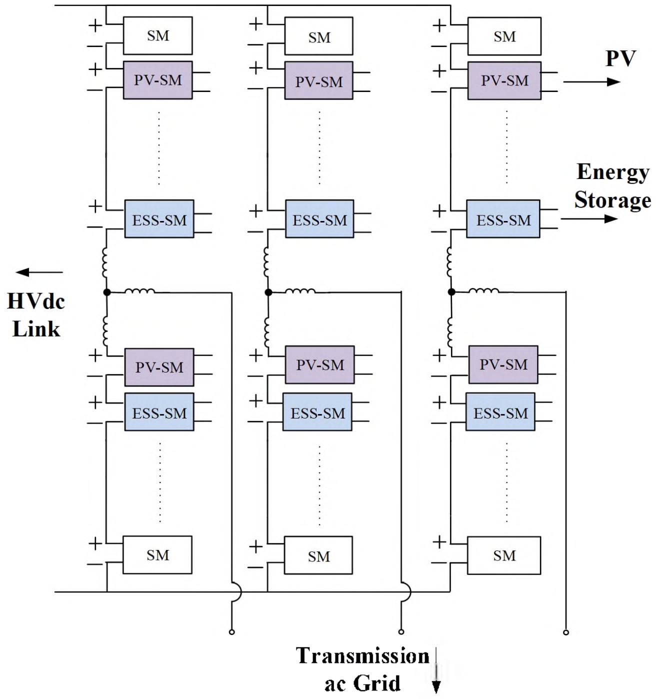

Figure 4. Overview of the MARS system architecture

such as virtual synchronous generator (VSG) based control [17]. In this paper, a VSG-based control method is employed in the MARS system power plant. The detailed implementation of the entire control architecture of the MARS system is described in [17].

3. PLANT INFORMATION AND UPGRADE NEEDS

In this study, the following plants are studied: (a) a PV plant with and without upgrades; (b) hybrid PV plants with and without upgrades, and (c) a MARS system when they are connected to an Western Interconnection (WI) based ac grid with very low SCR of 2 and inertia 11 at Victorville, California. The frequency dynamics of the ac grid are accurately included based on the data-driven approach [21].

3.1. MARS PLANT AT VICTORVILLE

The number of each type of SMs required in the MARS plant at Victorville, California is tabulated in Table 1. The size of the PV and ESS SMs is determined based on utilizing 200 A, 3.3 kV SiC devices. The total number of SMs per arm is determined by the dc-link voltage at the location.

Table 1. Victorville MARS system parameters

Parameter	Value
System rating	2000 MW
dc bus voltage (V_{dc})	±525 kV
ac side voltage (V_{ac})	500 kV
PV system power rating (P_{PV})	1000 MW
ESS system power rating (P_{ESS})	389.8 MW
ESS system energy rating (E_{ESS})	1232.3 MWh
Number of normal SMs per arm (N_{norm})	111
Number of PV SMs per arm (N_{PV})	208
Number of ESS SMs per arm (N_{ESS})	81
Total number of SMs per arm (N)	400
Arm inductance (L_{o})	90.0 mH
Arm resistance (R_{o})	0.1 Ω
Grid side inductance (L_{s})	40.0 mH
Grid side resistance (R_{s})	0.83333 Ω
SM capacitor voltage (V_{SM})	2.625 kV
SM capacitance	20.0 mF
Power rating of PV and ESS SMs	800 kW

3.2. PV PLANT AND HYBRID PV PLANT INFORMATION

The PV plant in both the state-of-the-art PV plant and the state-of-the-art hybrid PV plant is rated at 1000 MW (for a large plant) and is connected to a power transformer of 33 kV/500kV (based on typical voltages). The 500 kV side of the power transformer is connected to the ac grid model of the Western Electric Coordinating Council (WECC). The ac grid model of the WECC is described in [21]. The ESS plant is rated 389.8 MW.

Each inverter unit in the discrete PV plant and the discrete hybrid PV plants is rated 800 kW. There are 1248 inverter units in the PV plants of the discrete PV plant and the discrete hybrid PV plant. Each of the 486 inverter units in the ESS plant are also rated 800 kW.

3.3. SYNCHRONOUS CONDENSERS TO INCREASE SCR

In the scenarios of a high penetration of PE-based systems and a low traditional synchronous machine resource based system, the ac grid short circuit strength might be quite low. This inadequacy in providing sufficient short circuit strength may lead to stability problems while connecting newer PE-based systems. One of the potential solutions to such problems is installing synchronous condensers in the system. Therefore, synchronous condensers are installed as an “upgrade” in the ac grid to ensure stable operation of the discrete PV plant and the discrete hybrid PV plant considered in this study. The objective of installing synchronous condensers in the low SCR and low inertia grids along with these plants is to increase the SCR of the grid.

3.3.1. Selection of Synchronous Condensers Rating. The synchronous condenser installed in the ac grid is modeled based on a GENROU synchronous machine model with an IEEE Type-1 excitation system model. There is no governor attached to the turbine of

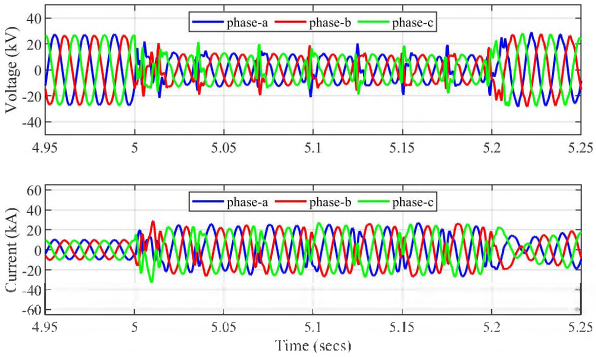

Figure 5. POC instantaneous grid voltage and currents for PV plant with synchronous condenser rating = 500 MVA

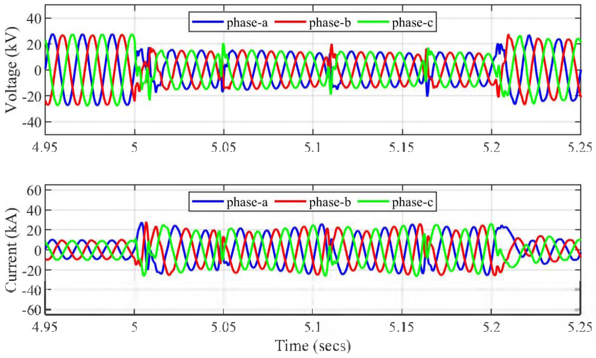

Figure 6. POC instantaneous grid voltage and currents for PV plant with synchronous condenser rating = 1000 MVA

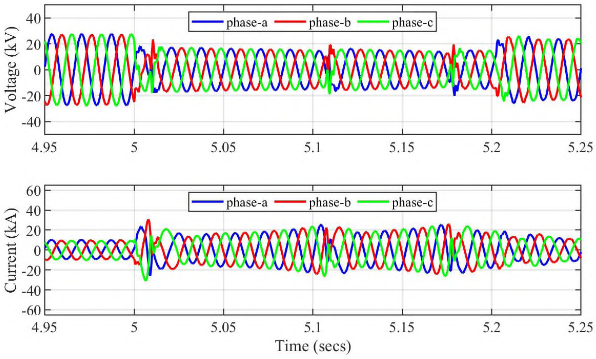

Figure 7. POC instantaneous grid voltage and currents for PV plant with synchronous condenser rating = 1500 MVA

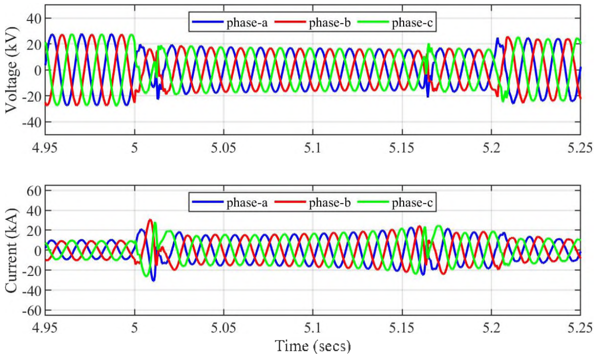

Figure 8. POC instantaneous grid voltage and currents for PV plant with synchronous condenser rating = 2000 MVA

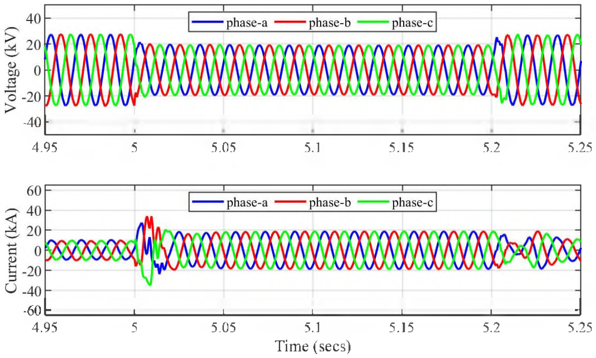

Figure 9. POC instantaneous grid voltage and currents for PV plant with synchronous condenser rating = 2500 MVA

the machine. The synchronous condensers are installed on the low voltage side of the power transformer. The selection of synchronous condenser ratings is based on the design studies performed for stable operation of PV plants and hybrid PV plants. In these studies, the total synchronous condenser rating is varied proportional to the PV plant rating. Simulation studies are performed in the PSCAD environment for synchronous condenser ratings of 500 MVA ($\frac{1}{2}$ of the PV plant rating), 1000 MVA (the PV plant rating), 1500 MVA (1.5 of the PV plant rating), 2000 MVA (twice the PV plant rating), and 2500 MVA (2.5 times the PV plant rating). The POC instantaneous grid voltages and POC instantaneous grid currents at the PV plant for different synchronous condenser ratings are shown in Figure 5 – Figure 9. It is observed from Figure 5 – Figure 8 that the POC instantaneous grid voltages and currents have oscillations during three-phase fault conditions. In these cases, in addition to the oscillations observed during fault period, the THD on the high voltage side is above the recommended limits of IEEE 519-2014 [22] during pre- and post-fault conditions. In Figure 9, the POC instantaneous grid voltages and currents are devoid of any oscillations. Based on these simulation analyses and observations, the rating of the synchronous condenser is identified to be 2500 MVA for stable and reliable operation of the PV plant. Based on a similar design approach, the synchronous condenser rating required

Table 2. Parameters of synchronous condensers

Parameter	Value
Total synchronous condenser rating (for discrete PV plant)	2500 MVA
Total synchronous condenser rating (for discrete hybrid PV plant)	3500 MVA
Rated RMS voltage (LL)	20 kV
Inertia constant (H)	4.1214 MW.s/MVA
Damping (D)	1.0 p.u.

for stable and reliable operation of the hybrid PV plant is identified to be 3500 MW (2.5 times the hybrid PV plant rating). With the installation of the synchronous condensers with identified rating, the SCR of the system is increased to 9.169. Based on a similar design approach, the synchronous condenser rating required for stable and reliable operation of the hybrid PV plant is identified to be 3500 MW (2.5 times the hybrid PV plant rating). In this case, the system SCR is identified to be 5.345.

The dynamic parameters of the GENROU model are based on typical values of synchronous machines. The rating and the dynamic parameters of the synchronous condensers are tabulated in Table 2. The rating of the synchronous condensers is different for the discrete PV plant and the discrete hybrid PV plant, but the per unit dynamic parameters are the same.

3.4. SHUNT CAPACITOR BANKS AND DAMPERS TO REDUCE THD

In the MARS system, the total harmonic distortion (THD) on the high-voltage side (500 kV) is well within the recommended limits specified in IEEE 519-2014 [22]. The multi-level nature of the voltage generated helps with maintaining the THD below the prescribed limits. Hence, no additional capacitor banks and/or dampers are necessary in MARS. In contrast to the MARS systems, the THD of the high-voltage side of the discrete

PV and the hybrid PV plants is greater than the recommend limits specified in IEEE 519-2014 [22]. Therefore it is necessary to install shunt capacitor banks along with upgrading dampers in the PV plant and hybrid PV plants to ensure that the THD of the plant is below the recommended limits. The shunt capacitors are installed on the low-voltage side (33 kV) of the power transformer based on the guidelines described in [19]. The dampers are installed on the low-voltage side of the PV inverter transformer in the PV plants and on the low-voltage side of ESS inverter transformer [19]. The dampers are upgraded accordingly to ensure THD and TDD recommended limits of IEEE 519-2014 are met.

3.4.1. PV Plant. The THD of the high-voltage side (500 kV) grid voltage of the PV plant is shown in Figure 10 with and without shunt capacitors. It is observed from Figure 10 that with the installation of 100 μF shunt capacitor banks on the low voltage side (33 kV) of the power transformer and upgrading dampers on the low voltage side of the PV inverter transformer, the THD reduces to the recommended limits of 1.5% (average value). Without installation of shunt capacitors and dampers the THD of approximately 12% is considerably above the recommended limits. The total demand distortion (TDD) of the grid current of PV plant at the high-voltage side is shown in Figure 11. It is observed from Figure 11 that the TDD is 1.75% without the installation of shunt capacitors and dampers. It is observed from Figure 11 that the TDD is reduced to 0.4% (i.e. within the recommended limits) with

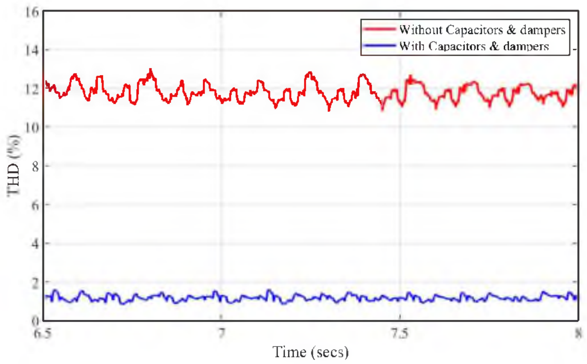

Figure 10. THD on high-voltage side (500 kV) of PV plant

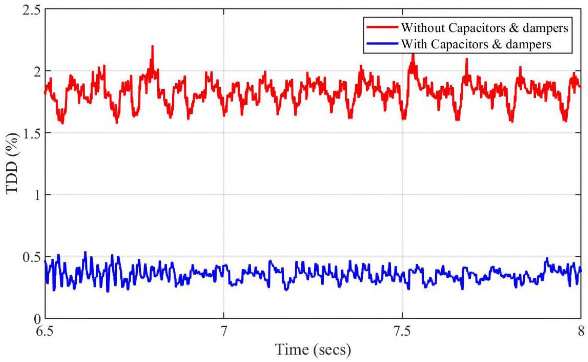

Figure 11. TDD of grid currents on high-voltage of PV plant

the installation of shunt capacitors and dampers. The THD of the grid voltages and TDD of grid currents on the low-voltage side for the PV plants are below the recommended limits with and without shunt capacitors and damper upgrades.

3.4.2. Hybrid PV Plant. The THD of the high-voltage side (500 kV) grid voltage of the hybrid PV plant is shown in Figure 12 with and without shunt capacitors. It is observed from Figure 12 that with the installation of 40 μF shunt capacitor banks on the low-voltage side (33 kV) of each of the power transformer in the PV and ESS plants and upgrading dampers on the low-voltage side of the PV inverter transformer and ESS inverter transformer, the THD reduces to the recommended limits of 1.0% (average value). Without

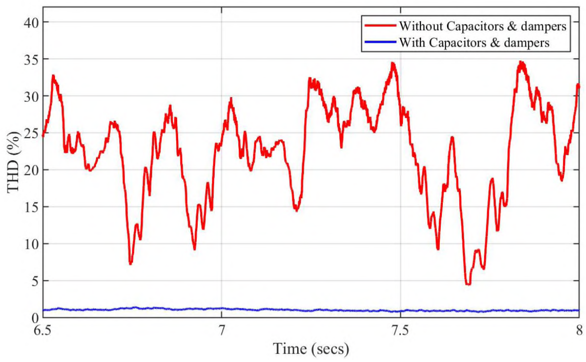

Figure 12. THD on high-voltage side (500 kV) of hybrid PV plant

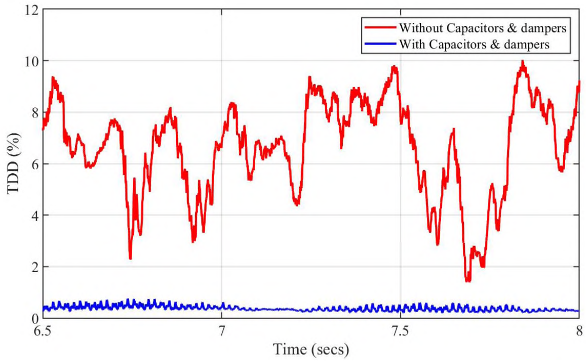

Figure 13. TDD of grid currents on the high-voltage side of hybrid PV plant

installation of shunt capacitors and dampers, the THD is well above the recommended limits (>> 1.5%). The total demand distortion (TDD) of the grid current of the PV plant at the high voltage side is shown in Figure 13. It is observed from Figure 13 that the TDD is well above the recommended limits (>> 1.5%) without the installation of shunt capacitors and dampers. It is observed from Figure 13 that the TDD is reduced to 0.4% (i.e. within the recommended limits) with the installation of shunt capacitors and dampers. The THD of the grid voltages and TDD of the grid currents on the low-voltage side for hybrid PV plants are below the recommended limits with and without shunt capacitors and damper upgrades.

4. PSCAD SIMULATION RESULTS

One of the objectives of this study is to compare the PV and hybrid PV plants with additional upgrades with MARS. The performance criteria is based on provision of continuity of operation that include a provision of continuity of operations and Q_{poc} support under transmission line balanced and unbalanced faults. The PV and ESS power available to provide support during disturbances are kept the same in all of the proposed options in comparison to the MARS system. In all of the plants, the following two use cases are considered: (a) a balanced three-phase fault at t = 5.0 s with a duration of 0.2 s; and (b) a line-to-line fault at t = 6.0 s with a duration of 0.2 s.

4.1. PV PLANT + UPGRADES

4.1.1. Use Case 1: Three-Phase Fault. The PV plant is operating at a PV power dispatch (P_{ac}) of 390 MW. A three-phase fault is simulated on the transmission line between the ac grid and the PV plant at t = 5.0 s with a fault duration of 0.2 s. After 0.2 s, the fault is self-cleared. During the three-phase fault, the PV plant alone failed to provide continuity of service (if operated without any additional upgrades). With the installation of synchronous condenser, shunt capacitors, and dampers, the PV plant was able to provide continuity of service as well as Q_{poc} support during three-phase fault as shown in Figure 14

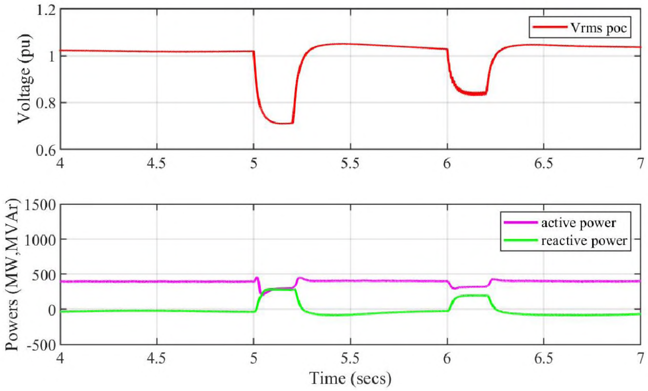

Figure 14. POC RMS grid voltage, P_{poc} and Q_{poc} of the PV plant with SCR 2 and inertia 11

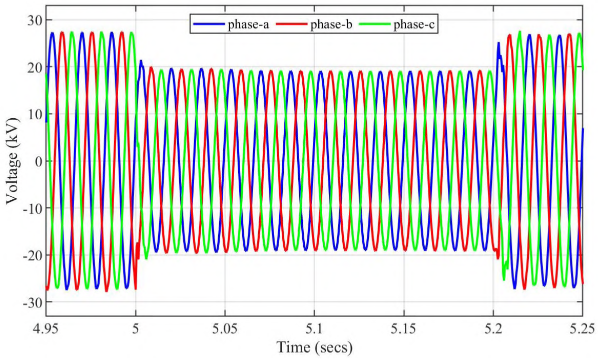

Figure 15. POC instantaneous grid voltage during a three-phase fault for PV plant with SCR 2 and inertia 11

and Figure 15. From Figure 14b, it is observed that: a) the PV plant provides continuity of operation through pre-fault, during the fault, and post fault conditions; b) during the three-phase fault, the Q_{poc} provided by the PV plant is similar to the Q_{poc} provided by the MARS system as shown in Figure 20b; and c) during the three-phase fault, the P_{poc} provided by PV plant is 300 MW approximately, whereas the P_{poc} provided by MARS is 350 MW approximately as shown in Figure 20b. From Figure 15, the instantaneous three-phase grid voltages at the POC are observed to be free of oscillations indicating voltage stability at the POC.

4.1.2. Use Case 2: Line-to-Line Fault. A line-to-line fault is simulated on the transmission line between the ac grid and the PV plant at t = 6.0 s with the fault duration of 0.2 s. During the line-to-line fault, the PV plant alone failed to provide continuity of service (if operated without any additional upgrades). With the installation of synchronous condensers, shunt capacitors and upgrading dampers, the PV plant was able to provide continuity of service during the line-to-line fault as shown in Figure 14 and Figure 16. In this use case, it is observed from Figure 14b that the Q_{poc} provided by the PV plant is approximately 4.25x the amount of Q_{poc} provided by the MARS system as shown in Figure 20b. Additionally, it is observed from the figure that the P_{poc} provided by PV plant

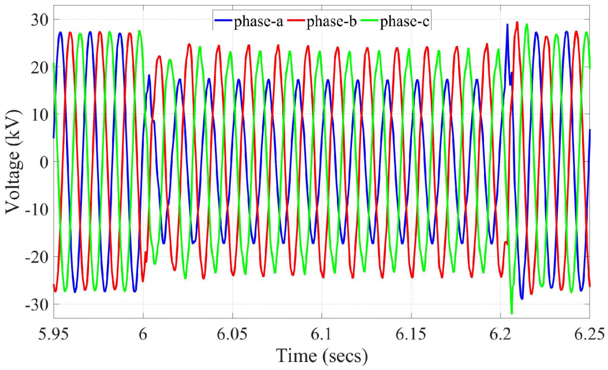

Figure 16. POC instantaneous grid voltage during a line-to-line fault for PV plant with SCR 2 and inertia 11

is similar to the P_{poc} provided by the MARS system. From Figure 16, the instantaneous three-phase grid voltages at the POC are free of oscillations indicating voltage stability at the POC.

4.2. HYBRID PV PLANT + UPGRADES

4.2.1. Use Case 1: Three-Phase Fault. The hybrid PV plant is operating at a PV power dispatch P_{ac} of 390 MW. This scenario indicates that the net P_{poc} generated by PV plant is used to charge the ESS plants similar to the operating case in the MARS system. A three-phase fault is simulated on the transmission line between the ac grid and the PV plant at t = 4.0 s with a fault duration of 0.2 s. After 0.2 s, the fault is self-cleared. During the three-phase fault, the hybrid PV plant alone failed to provide continuity of service (if operated without any additional upgrades).

With the installation of synchronous condenser, shunt capacitors, and upgrading dampers at PV and ESS plants, the hybrid PV plant was able to provide continuity of service as well as Q_{poc} support during the three-phase fault as shown in Figure 17 and

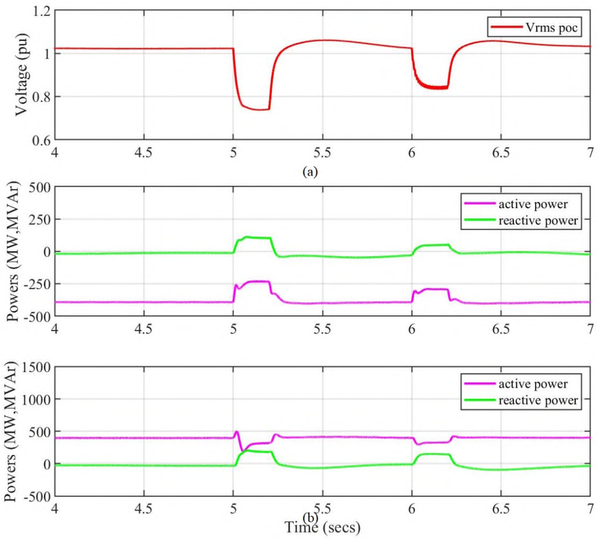

Figure 17. POC RMS grid voltage, P_{poc} and Q_{poc} of the hybrid PV plant with SCR 2 and inertia 11

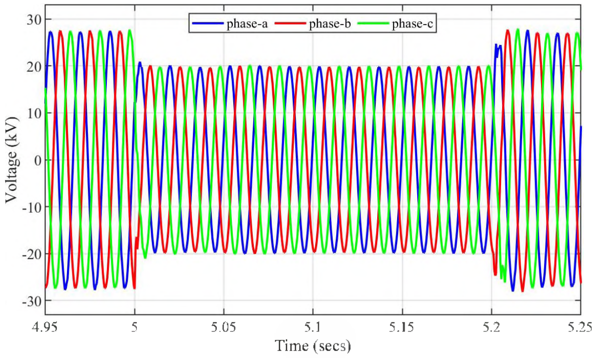

Figure 18. POC instantaneous grid voltage during a three-phase fault for hybrid PV plant with SCR 2 and inertia 11

Figure 18. From Figure 17, it is observed that the hybrid PV plant provides continuity of operation during the fault and post fault. It is observed from Figure 17b and Figure 17c that the P_{poc} generated from the PV plant is used to charge the ESS plant. During the three-phase fault, the P_{poc} is reduced to 315 MW and in the MARS system the P_{poc} is reduced to 357 MW. From this observation, it can be inferred that both the discrete hybrid PV plant and the MARS system provide continuity of operation during the three-phase fault. In hybrid PV plants, the Q_{poc} is provided by the PV and ESS plants. During the three-phase fault, it is observed from Figure 17b and Figure 17c that the total Q_{poc} provided by the ESS plant and PV plant is similar to the Q_{poc} provided by the MARS system as shown in Figure 20b. From Figure 18, the instantaneous three-phase grid voltages at the POC are free of oscillations indicating voltage stability at the POC.

4.2.2. Use Case 2: Line-to-Line Fault. A line-to-line fault is simulated on the transmission line between the ac grid and the hybrid PV plant at t = 5.0 s with a fault duration of 0.2 s. During the line-to-line fault, the hybrid PV plant alone failed to provide continuity of service (if operated without any additional upgrades). With the installation of synchronous condensers, shunt capacitors, and dampers, the hybrid PV plant was able to provide continuity of service during the line-to-line fault as shown in Figure 17 and

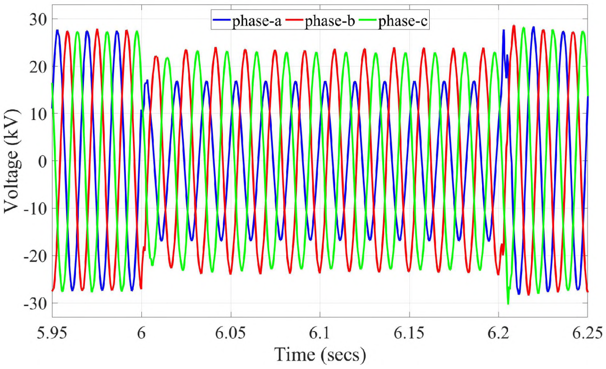

Figure 19. POC instantaneous grid voltage during a line-to-line fault for hybrid PV plant with SCR 2 and inertia 11

Figure 19. In this use case, it is observed from Figure 17b and Figure 17c that the total Q_{poc} provided by the hybrid PV plant (from the PV plant and the ESS plant) is 4.25x the amount of Q_{poc} provided by the MARS system as shown in Figure 20b. Also from these figures it is observed that the P_{poc} is reduced to 325 MW during line-to-line fault and in the MARS system the P_{poc} is reduced to 325 MW. As in the case of three-phase fault, it is also inferred that both the discrete hybrid PV plant and the MARS plant provide continuity of operation during the line-to-line fault too. From Figure 19, the instantaneous three-phase grid voltages at the POC are free of oscillations indicating voltage stability at the POC.

4.3. MARS

4.3.1. Use Case 1: Three-Phase Fault.

The MARS plant is operating at an ac power dispatch $P_{\text{ac}} = P_{\text{dc}}$ of 650 MW. In this operating condition, the total active power provided by the PV SMs is utilized to charge the ESS systems. A three-phase fault is simulated on the transmission line between the ac grid and the MARS plant at t = 4.0 s with the fault duration of 0.2 s. After 0.2 s, the fault is self-cleared. During the three-phase fault, the MARS plant is able to provide continuity of service without any additional upgrades as shown in Figure 20a and Figure 20b. It is observed from Figure 20b, the P_{poc} provided by

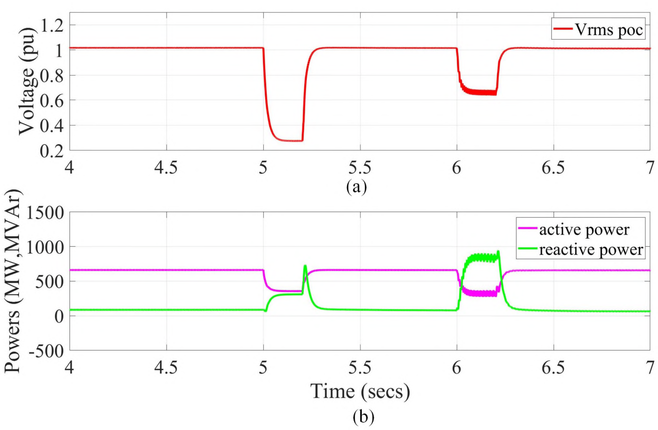

Figure 20. POC RMS grid voltage, P_{poc} and Q_{poc} of the MARS system during a three-phase fault for SCR = 2 and inertia = 11

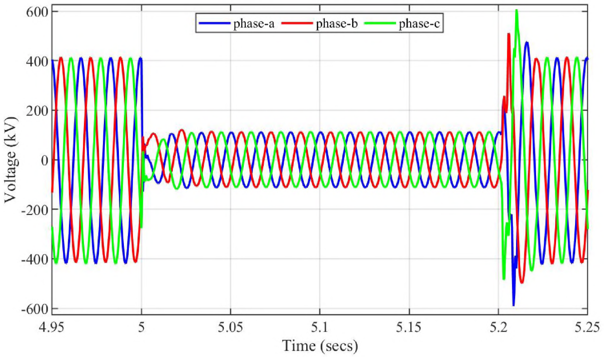

Figure 21. Instantaneous ac grid voltage for SCR = 2 and inertia = 11 during a three-phase fault

the MARS system at POC is reduced to 357 MW during the three-phase fault and the total active power generated from PV SMs is used for charging the ESS SMs. From Figure 20b it is observed that the Q_{poc} support of 310 MVAr is provided by the MARS system during the three-phase fault. The instantaneous three-phase grid voltages at the POC are shown in Figure 21. From the figure, it is observed that there are no undesired oscillations causing instabilities during the three-phase fault and post fault periods.

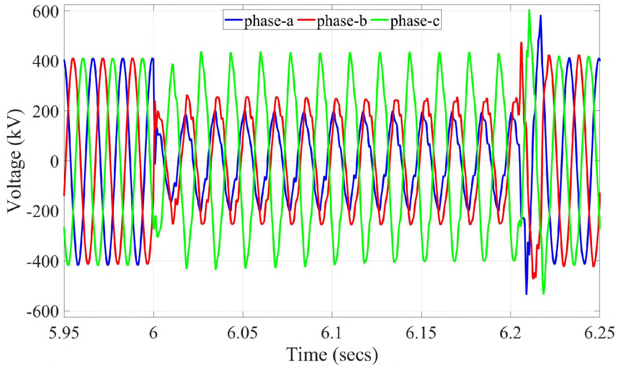

Figure 22. Instantaneous ac grid voltage for SCR = 2 and inertia = 11 during a line-to-line fault

4.3.2. Use Case 2: Line-to-Line Fault. A line-to-line fault is simulated on the transmission line between the ac grid and the MARS plant at t = 5.0 s with the fault duration of 0.2 s for the same operating condition described in Section 4.3.1. During the line-to-line fault, the MARS plant is able to provide continuity of service without any additional upgrades as shown in Figure 20b. It is observed from Figure 20b, the P_{poc} provided by the MARS system at POC is reduced to 325 MW during the line-to-line fault and the Q_{poc} support of 850 MVAr is provided by the MARS system during the line-to-line fault. The instantaneous three-phase grid voltages at the POC are shown in Figure 22. From the figure, it is observed that there are no undesired oscillations causing instabilities during the fault, pre-fault, and post fault periods.

5. DISCUSSIONS

In this section, the technical merits of the MARS plant in comparison to the discrete hybrid PV plant are presented. Additionally, the upgrade requirements for providing continuity of operation during transmission line balanced and unbalanced faults in discrete PV plant and discrete hybrid PV plant are presented. The technical merits of the MARS plant include: (a) provision of continuity of operation with and without additional control algorithms used for voltage support during transmission line balanced and unbalanced faults; (b) THD and TDD requirements are always below the recommendation limits of IEEE 519-2014 [22]; and (c) stable Q_{poc} is always provided during balanced and unbalanced faults at different locations and different fault magnitudes. The MARS plant provides continuity of operation even when connected to low SCR and low inertia ac grids because of these technical merits.

The discrete PV plant and the discrete hybrid PV plant without upgrades could not provide continuity of operation during balanced and unbalanced transmission line faults for the same operating conditions and ac grid conditions as in the MARS system when connecting to a low SCR and low inertia grid. The main reason for such behavior is insufficient short circuit strength in the ac grid that led to unstable operation of the discrete PV and discrete hybrid PV plant. To ensure continuity of operation and enhanced stability, additional reinforcements such as synchronous condensers, shunt capacitors, and dampers were installed in the system. The synchronous condensers improved the short circuit strength of the system and enhanced the stability of the connected plant. Shunt capacitors and dampers were also installed in the system to reduce the harmonics produced by the PV and ESS plant inverters. A detailed comparison of the performance of discrete hybrid PV

Table 3. Performance comparison between MARS and hybrid PV plant

Fault magnitude	Fault distance	MARS	Discrete hybrid PV plant
1.435 Ω	long	STABLE	STABLE
1.435 Ω	medium	STABLE	further analysis required
1.435 Ω	short	STABLE	further analysis required
5.435 Ω	long	STABLE	STABLE
5.435 Ω	medium	STABLE	further analysis required
5.435 Ω	short	STABLE	further analysis required
25.435 Ω	long	STABLE	STABLE
25.435 Ω	medium	STABLE	STABLE
25.435 Ω	short	STABLE	STABLE

plants with the MARS plant at different locations with different fault magnitudes during balanced and unbalanced transmission line faults were analyzed and tabulated in Table 3. From this fault analysis, it is observed that the MARS power plants could provide stable Q_{poc} in all of the scenarios irrespective of the fault location and fault magnitude. For the balanced faults, the hybrid PV plant could only provide stable Q_{poc} support in the scenarios where the fault location was at a long distance (600 km). Further analysis is required for the scenarios where the fault location is closer to the plant (60 km) and fault location is at a medium distance (300 km), as initial studies have indicated unstable operation without control and/or further hardware reinforcements. For the unbalanced faults, the hybrid PV plant could provide stable Q_{poc} in all of the scenarios.

6. CONCLUSION

This paper presents a set of solutions that enable PE-interfaced resources that connect to low SCR and low inertia grids to operate without momentary cessation. The solutions include: (a) addition of traditional upgrades such as synchronous condensers, shunt capacitors, and dampers to state-of-the-art PV plants and hybrid PV plants so that they can provide voltage support (ensuring continuity of operation during balanced and unbalanced transmission line faults); and, (b) integrated PV-ESS plants that connect to HVdc and high-voltage ac transmission grids (MARS). The proposed solutions were evaluated under different operating conditions and fault types using EMT models developed in PSCAD/EMTDC enviroment. In addition to evaluating different solutions, a technical comparison is provided between the MARS system and the discrete hybrid PV plants. The MARS system provides continuity of operation without any additional ac upgrades. This may potentially reduce the redundancy of PE-based resources and additional upgrade requirements, improving reliability and reducing the overall cost.

ACKNOWLEDGEMENT

This paper is based upon work supported by the U.S. Department of Energy's Office of Energy Efficiency and Renewable Energy (EERE) under Solar Energy Technologies Office (SETO) Agreement Number 34019. Authors would like to thank Dr. John Seuss for overseeing the project developments and providing guidance. The views expressed herein do not necessarily represent the views of the U.S. Department of Energy or the United States Government.

REFERENCES

[1] M. Lewis, "Energy Storage Procurement Tracker," 2020. [Online]. Available: https://www.morganlewis.com/-/media/files/document/2020/energy_storage_tracker_2020.pdf

[2] North American Electric Reliability Corporation, "BPS-Connected Inverter-Based Resource Performance," 2018. [Online]. Available: https://www.nerc.com/comm/PC_Reliability_Guidelines_DL/Inverter-Based_Resource_Performance_Guideline.pdf

[3] "IEEE Standard for Interconnection and Interoperability of Distributed Energy Resources with Associated Electric Power Systems Interfaces - redline," *IEEE Std 1547-2018 (Revision of IEEE Std 1547-2003) - Redline*, pp. 1–227, 2018.

[4] B. J. Pierre, M. E. Elkhatib, and A. Hoke, "Photovoltaic Inverter Momentary Cessation: Recovery Process is Key," in *Proc. 2019 IEEE 46th Photovoltaic Specialists Conference (PVSC)*.

[5] North American Electric Reliability Corporation, "1,200 MW Fault Induced Solar Photovoltaic Resource Interruption Disturbance Report," 2017. [Online]. Available: https://www.nerc.com/pa/rrm/ea/1200_MW_Fault_Induced_Solar_Photovoltaic_Resource_/1200_MW_Fault_Induced_Solar_Photovoltaic_Resource_Interruption_Final.pdf

[6] North American Electric Reliability Corporation, "900 MW Fault Induced Solar Photovoltaic Resource Interruption Disturbance Report," 2018. [Online]. Available: https://www.nerc.com/pa/rrm/ea/October%209%202017%20Canyon%202%20Fire%20Disturbance%20Report/900%20MW%20Solar%20Photovoltaic%20Resource%20Interruption%20Disturbance%20Report.pdf

[7] North American Electric Reliability Corporation, "April and May 2018 Fault Induced Solar Photovoltaic Resource Interruption Disturbances Report," 2019. [Online]. Available: https://www.nerc.com/pa/rrm/ea/April_May_2018_Fault_Induced_Solar_PV_Resource_Int/April_May_2018_Solar_PV_Disturbance_Report.pdf

[8] North American Electric Reliability Corporation, "San Fernando Disturbance," 2020. [Online]. Available: https://www.nerc.com/pa/rrm/ea/Documents/San_Fernando_Disturbance_Report.pdf

[9] North American Electric Reliability Corporation, "Generator Frequency and Voltage Protective Relay Settings," 2015. [Online]. Available: https://www.nerc.com/pa/Stand/Reliability%20Standards/PRC-024-2.pdf

[10] North American Electric Reliability Corporation, "Integrating Inverter-Based Resources into Low Short Circuit Strength Systems," 2017. [Online]. Available: https://www.nerc.com/comm/PC_Reliability_Guidelines_DL/Item_4a._Integrating%20_Inverter-Based_Resources_into_Low_Short_Circuit_Strength_Systems_-_2017-11-08-FINAL.pdf

[11] H. Shin, J. Jung, S. Oh, K. Hur, K. Iba, and B. Lee, "Evaluating the Influence of Momentary Cessation Mode in Inverter-based Distributed Generators on Power System Transient Stability," *IEEE Transactions on Power Systems*, vol. 35, no. 2, pp. 1618–1626, 2020.

[12] H. Shin, J. Jung, and B. Lee, "Determining the Capacity Limit of Inverter-based Distributed Generators in High-Generation Areas Considering Transient and Frequency Stability," *IEEE Access*, vol. 8, pp. 34 071–34 079, 2020.

[13] C. Li and R. Reinmuller, "Fault Responses of Inverter-based Renewable Generation: On Fault Ride-Through and Momentary Cessation," in *Proc. 2018 IEEE Power Energy Society General Meeting (PESGM)*.

[14] Y. Wu, D. Zhang *et al.*, "Modeling and Mechanism Investigation of Inertia and Damping Issues for Grid-Tied PV Generation Systems with Droop Control," *Energies*, vol. 12, p. 1985, 2019.

[15] C. Loutan, P. Klauer *et al.*, "Demonstration of Essential Reliability Services by a 300-MW Solar Photovoltaic Power Plant," 2017. [Online]. Available: https://www.nrel.gov/docs/fy17osti/67799.pdf

[16] N. Mohan, W. Hess, and J.Bakke, "Renewable Integration Impact Assessment: Finding integration inflection points of increasing renewable energy."

[17] S. Debnath, P. Marthi, Q. Xia, J. Pan, M. Saeedifard, V. N. Vipin, S. Chakraborty, and M. Arifujjaman, "Renewable Integration in Hybrid ac-dc Systems using Multiport Autonomous Reconfigurable Solar power plant (MARS)," *IEEE Transactions on Power Systems*, pp. 1–1, 2020.

[18] P. R. V. Marthi, S. Debnath, and M. L. Crow, "Synchronverter-based Control of Multi-Port Autonomous Reconfigurable Solar Plants (MARS)," in *Proc. ECCE2020 - Twelfth Annual IEEE Energy Conversion Congress and Exposition*, Oct.

[19] PSCAD, "Simple Solar Farm Model," 2019. [Online]. Available: https://www.pscad.com/knowledge-base/article/521

[20] P. R. V. Marthi, S. debnath, Q. Xia, and M. Saeedifard, "Advanced and Fast Simulation Suite of Models for Multi-Port Autonomous Reconfigurable Solar Plants," in *Proc. 2020 IEEE PES T&D Conference & Exposition.*

[21] S. Debnath and J. Sun, "Fidelity Requirements with Fast Transients from VSC-HVdc," in *Proc. IECON 2018 - 44th Annual Conference of the IEEE Industrial Electronics Society*, pp. 6007–6014.

[22] "IEEE Recommended Practice and Requirements for Harmonic Control in Electric Power Systems," *IEEE Std 519-2014 (Revision of IEEE Std 519-1992)*, pp. 1–29, 2014.

SECTION

2. CONCLUSION

The dissertation is mainly focused on three aspects, they are: modeling, control, and application of MARS. The first research goal of this dissertation is to develop and implement advanced *grid forming* predictive control method in real-time for MARS to provide frequency support and voltage support during grid side disturbances. To achieve this goal, the need of developing ultra fast high fidelity simulation models was of paramount importance. Therefore, an ultra fast CPU simulation algorithm to simulate the MARS system based on statespace models, hybrid discretization algorithm with a relaxation technique that reduces the imposed computational burden is developed. Also, SG-based control methods based on classical control methods were developed. The proposed control methods were implemented, tested and evaluated for MARS Pittsburg in PSCAD/EMTDC and also compared with *grid following* control method. The second main research objective is to propose MARS as one of the suite of solutions to momentary cessation problems. Solutions based on PV plant with upgrades and hybrid PV plants with upgrades were also proposed. These solutions were tested and evaluated for large utility-scale PV and hybrid plants in PSCAD/EMTDC environment. A detailed comparison between discrete development of PV and ESS connecting to transmission ac grid and HVdc links and MARS has been performed to establish the benefits of integrated development of PV, ESS and HVdc systems. Future avenues of research might include developing MARS-based multi-terminal direct current (MTdc) systems connecting multiple asynchronous grids and developing control algorithms for those systems.

REFERENCES

[1] North American Electric Reliability Corporation, "BPS-Connected Inverter-Based Resource Performance," 2018. [Online]. Available: https://www.nerc.com/comm/PC_Reliability_Guidelines_DL/Inverter-Based_Resource_Performance_Guideline.pdf

[2] L. Yashen, J. H. Eto, B. B. Johnson, J. D. Flicker, R. H. Lasseter, H. N. V. Pico, G.-S. Seo, B. J. Pierre, and A. Ellis, "Research Roadmap on Grid-Forming Inverters," 2020. [Online]. Available: https://www.nrel.gov/docs/fy21osti/73476.pdf.

[3] M. M. Merlin, T. C. Green, P. D. Mitcheson, D. R. Trainer, R. Critchley, W. Crookes, and F. Hassan, "The alternate arm converter: A new hybrid multilevel converter with dc-fault blocking capability," *IEEE transactions on power delivery*, vol. 29, no. 1, pp. 310–317, 2013.

[4] B. Jacobsson, P. Karlsson, G. Asplund, L. Harnefors, and T. Jonsson, "VSC-HVdc transmission with cascaded two-level converters," in *CIGRE Session*, 2010, pp. B4–B110.

[5] S. Du, A. Dekka, B. Wu, and N. Zargari, *Modular Multilevel Converters: Analysis, Control, and Applications*. IEEE, 2018.

[6] S. Debnath, J. Qin, B. Bahrani, M. Saeedifard, and P. Barbosa, "Operation, control, and applications of the modular multilevel converter: A review," *IEEE Transactions on Power Electronics*, vol. 30, no. 1, pp. 37–53, Jan 2015.

[7] M. Vasiladiotis and A. Rufer, "Analysis and control of modular multilevel converters with integrated battery energy storage," *IEEE Transactions on Power Electronics*, vol. 30, no. 1, pp. 163–175, Jan 2015.

[8] M. A. Perez, D. Arancibia, S. Kouro, and J. Rodriguez, "Modular multilevel converter with integrated storage for solar photovoltaic applications," in *Proc. IECON 2013 - 39th Annual Conference of the IEEE Industrial Electronics Society*, pp. 6993–6998.

[9] H. Bayat and A. Yazdani, "A hybrid MMC-based photovoltaic and battery energy storage system," *IEEE Power and Energy Technology Systems Journal*, vol. 6, no. 1, pp. 32–40, March 2019.

[10] J. Khazaei, G. Pavlak, B. Lee, and M. Elsenbaty, "A novel application of modular multi-level converters for partially shaded PV systems," in *Proc. 2019 IEEE Texas Power and Energy Conference (TPEC)*, pp. 1–6.

[11] S. Debnath and M. Chinthavali, "Numerical-stiffness-based simulation of mixed transmission systems," *IEEE Transactions on Industrial Electronics*, vol. 65, no. 12, pp. 9215–9224, Dec 2018.

[12] S. Debnath and M. Chinthavali, “MMC-HVdc: Simulation and control system,” in *Proc. 2016 IEEE Energy Conversion Congress and Exposition (ECCE)*, pp. 1–8.

[13] D. Rekioua and E. Matagne, *Optimization of Photovoltaic Power Systems*. Springer, 2012.

[14] H. Knaak, “Modular multilevel converters and HVdc/FACTS: A success story,” in *Proc. 2011 14th European Conference on Power Electronics and Applications*, pp. 1–6.

VITA

Phani Ratna Vanamali Marthi completed his Bachelor of Technology in Electrical and Electronics Engineering in May 2010 from Jawaharlal Nehru Technological University, Hyderabad, India. In 2013, Phani Marthi joined the graduate program at Missouri University of Science & Technology. From January 2018-December 2018, he interned at Oak Ridge National Laboratory (ORNL) and also worked as a sub-contract student at ORNL from December 2018-December 2020. He received his Doctor of Philosophy (PhD) in Electrical Engineering in May 2021 from Missouri University of Science & Technology. His main research interests included integration of renewable energy resources to HVdc systems, modeling, simulation, control, and application of HVdc converters.